2011

Integration Of High-q Filters With Highly Efficient Antennas

Yazid Yusuf
University of Central Florida

INTEGRATION OF HIGH-Q FILTERS WITH HIGHLY EFFICIENT ANTENNAS

by

YAZID YUSUF

M.S. University of Central Florida

A dissertation submitted in partial fulfillment of the requirements
for the degree of Doctor of Philosophy
in the Department of Electrical Engineering and Computer Science
in the College of Engineering & Computer Science
at the University of Central Florida
Orlando, Florida

Fall Term
2011

Major Professor: Xun Gong

ABSTRACT

The integration of high-quality (Q)-factor 3-D filters with highly efficient antennas is addressed in this dissertation. Integration of filters and antennas into inseparable units eliminates the transitions between the otherwise separate structures resulting in more compact and efficient systems. The compact, highly efficient integrated 3-D filter/antenna systems, enabled by the techniques developed herein, allow for the realization of integrated RF front ends with significantly- reduced form factors.

Integration of cavity filters with slot antennas in a single planar substrate is first demonstrated. Due to the high Q factor of cavity resonators, the efficiency of the integrated filter/antenna system is found to be the same as that of a reference filter with the same filtering characteristics. This means a near 100% efficient slot antenna is achieved within this integrated filter/antenna system. To further reduce the footprint of the integrated systems, vertically integrated filter/antenna systems are developed. We then demonstrate the integration of cavity filters with aperture antenna structures which enable larger bandwidths compared with slot antennas. The enhanced bandwidths are made possible through the excitation and radiation of surface waves. To obtain omnidirectional radiation patterns , we integrate cavity filters with monopole antennas. Finally, the integration of filters with patch antennas is addressed. Unlike the other filter/antenna integration examples presented, in which the antenna is utilized as an equivalent load, the patch antenna provides an additional pole in the filtering function.

The presented techniques in this dissertation can be applied for filter/antenna integration in all microwave, and millimeter-wave frequency regions.

This dissertation is dedicated to my mother and father.

ACKNOWLEDGMENTS

I would like to express my gratitude to my adviser, Prof. Xun Gong for his abundant help and invaluable assistance, support., and encouragement throughout my graduate studies. I thank the members of my dissertation committee, Prof. Parveen Wahid, Linwood Jones, Thomas Wu and Jing Wang for taking the time to review this work and providing valuable comments that helped improve this dissertation. I would also like to thank Dr. Siamak Ebadi for his friendship and advice.

It was a great experience working with my graduate colleagues, Rajesh Paryani, Ajay Subramanian, Ya Shen, Xinhua Ren, Mudar Al-Joumayly, Justin Luther, Paul Nelson, Kalyan Karnati, and Haitao Cheng. I would like to thank you for providing a stimulating and fun environment to learn, and most importantly, for being great friends.

Lastly, I wish to thank my father, Nihad Yusuf, my mother, Khawla Abu Nemer, my brothers Waleed, Marwan, and Laith, and my sister, Dima. Without your continued support and unconditional love, it would have been impossible for me to finish this work.

TABLE OF CONTENTS

LIST OF FIGURES viii
1 INTRODUCTION 1
1.1 Motivation 1
1.2 Literature Review 8
1.3 Dissertation Overview 9
2 APPLICATION OF COUPLED-MODE THEORY TO FILTER ANALYSIS 11
2.1 Introduction 11
2.2 Coupled-Mode Theory Review 13
2.3 Coupled-Mode Theory Applied to Filters 16
2.3.1 Physical Determination of Q_{ext} and k_{ij} 18
2.3.2 Comparison to Coupling Matrix Formulation 23
2.3.3 Application to Filter Insertion Loss 26
2.4 Conclusion 30
3 INTEGRATION OF FILTERS WITH SLOT ANTENNAS 31
3.1 Introduction 31
3.2 Filter Synthesis 31
3.3 Filter/Antenna Synthesis 34
3.3.1 Summary of the Filter/Antenna Synthesis Procedure 35
3.3.2 Select the Slot Antenna Initial Length 36
3.3.3 Generate Q_{ext} Design Curves and Determine the Antenna Length and Position 36
3.3.4 Compensate for the End Resonator Length 40
3.3.5 Time-Domain (TD) Synthesis of Filter/Antenna 42
3.3.6 Equivalent Circuit Model of the Filter/Antenna 44
3.3.7 Filter and Filter/Antenna Using CPW Feeding 46
3.4 Measurement Results and Discussions 49
3.4.1 Filter and Filter/Antenna Using Coaxial Feeding 49
3.4.2 Filter and Filter/Antenna Using CPW Feeding 51
3.5 Effect of Different Physical Parameters on Q_{ext} 57
3.6 Conclusion 63
4 VERTICAL INTEGRATION OF FILTERS WITH SLOT ANTENNAS 64

4.1 Introduction 64
4.2 Filter Synthesis 66
4.3 Filter/Antenna Synthesis 68
4.3.1 Frequency-Domain Slot Antenna Synthesis 69
4.3.2 Time-Domain (TD) Filter/Antenna Synthesis 74
4.4 Q Breakdown and Loss Analysis 76
4.5 Results and Discussion 79
4.6 Conclusion 82
5 INTEGRATION OF FILTERS WITH APERTURE ANTENNAS 84
5.1 Introduction 84
5.2 Filter/Antenna Synthesis 86
5.2.1 Resonator/Antenna Q_{ext}. 86
5.2.2 Resonator/Antenna Radiation Characteristics 93
5.2.3 Filter/Antenna Design. 96
5.3 Results and Discussion 99
5.4 Conclusion 102
6 INTEGRATION OF FILTERS WITH MONOPOLE ANTENNAS 103
6.1 Introduction 103
6.2 Filter/Antenna Synthesis 103
6.2.1 Modeling the Cavity and Monopole Antenna 105
6.2.2 Filter/Antenna Design 110
6.3 Results and Discussion 113
6.4 Conclusion 113
7 INTEGRATION OF FILTERS WITH PATCH ANTENNAS 116
7.1 Introduction 116
7.2 Filter/Antenna Synthesis 118
7.2.1 Modeling the Coupling Via Inside a Waveguide 121
7.2.2 Modeling the Coupling Via and the Patch Antenna 122
7.2.3 Filter/Antenna Modeling 123
7.2.4 Coupling between Patch and Middle Cavity (k_{23}) 126
7.2.5 Filter/Antenna Design 130
7.2.6 Filter/Antenna Efficiency 136
7.3 Fabrication and Measurement Results 138
7.4 Filter/Antenna Array 141

7.5 Conclusion 143
8 CONCLUSION AND FUTURE WORK 144
8.1 Contributions 144
8.2 Future Work 145
8.2.1 Integration of Antennas with other High-Q Filters. 145
8.2.2 Implementation of Vertically Integrated Filter/antennas in Antenna Arrays 145
8.2.3 Integrated Filter/antenna Systems with General Filtering Functions 145
8.2.4 Tunable Integrated Filter/Antenna Systems 146
9 REFERENCES 147

LIST OF FIGURES

Figure 1.1: Block diagram of (a) transmitter, and (b) receiver of a communications system. 2

Figure 1.2: Schematics of (a) a SIW cavity filter connected with a cavity-backed slot antenna using coaxial connectors; (b) an integrated filter/antenna system. 4

Figure 1.3: (a) responses of discrete filter and antenna; and (b) S_{11} response of the cascaded system compared with the discrete filter. 6

Figure 1.4: Comparison of the responses of the discrete filter, cascaded filter with antenna, and the integrated filter/antenna. 7

Figure 2.1: Extraction of Q_{ext} from the phase of S_{11}. 20

Figure 2.2: Simulation setup of weakly excited coupled resonators to extract k_{ij}. 22

Figure 2.3: Simulated S_{21} of the setup in Figure 2.2 used to extract k_{ij}. 22

Figure 2.4: Equivalent circuit of a two-pole filter. 23

Figure 2.5: Fractional difference between the two frequency variables p_1 and p_2. 26

Figure 2.6: S-parameters of a two-pole filter calculated using p_1, and p_2. 27

Figure 2.7: S-parameters of a four-pole filter. 29

Figure 3.1: Schematics of (a) a coaxial-fed filter connected with a cavity-backed slot antenna using coaxial connectors; (b) a coaxial-fed integrated filter/antenna; (c) a CPW-fed filter connected with a cavity-backed slot antenna using CPW lines; (d) a CPW-fed integrated filter/antenna. 32

Figure 3.2: (a) Schematic of a filter using coaxial feeding. Picture of the (b) top and (c) back side. (L_1 = 20.4 mm; L_2 = 14.4 mm; W = 13 mm; W_1 = 5.4 mm; W_2 = 4.5 mm; P_p = 5.6 mm) ... 33

Figure 3.3: (a) Schematic of a filter/antenna using coaxial feeding. Picture of the (b) antenna and (c) coaxial feeding side. (L_1 = 20.4 mm; L_2 = 14.4 mm; L_3 = 14.5 mm; L_4 = 9.6 mm; W = 13 mm; W_1 = 5.4 mm; W_2 = 4.5 mm; W_3 = 5.2 mm; W_a = 1 mm; L_a = 12.2 mm; P_a = 2.3 mm; P_p = 5.6 mm) 34

Figure 3.4: Synthesis procedure of filter/antenna. 35

Figure 3.5: (a) Schematic of a transverse slot in a waveguide and (b) its equivalent circuit. (c) Normalized slot impedance for L_a = 12.1 mm and W_a = 1 mm. 37

Figure 3.6: (a) Schematic of a slot antenna in a resonator and (b) its equivalent circuit. (c) Simulated reflection coefficients for a slot antenna inside an end resonator (L_a = 12.1 mm, W_a = 1 mm, P_a = 2.3 mm, L_4 = 10.7 mm)..... 38

Figure 3.7: The input impedance of the structure in Fig. 3.6(a). 40

Figure 3.8: Extracted Q_{ext} versus slot antenna position P_a for slot antenna length L_a =10, 10.5, 11, 11.5, 12, and 12.5 mm..... 41

Figure 3.9: The equivalent circuit of an impedance inverter that utilizes an iris and transmission lines. 41

Figure 3.10: Simulated S_{11} and S_{21} of the filter shown in Fig. 3.2. Simulated S_{11} and gain (at boresight) of the filter/antenna shown in Fig. 3.3. 43

Figure 3.11: Simulated time-domain responses of the filter and filter/antenna. 43

Figure 3.12: Equivalent circuit models of (a) the filter in Fig. 3.2 and (b) filter/antenna in Fig. 3.3. (Z_0 = 50 Ω; K_{01} = K_{45} = 21.9 Ω; K_{12} = K_{34} = 8.75 Ω; K_{23} = 7.05 Ω; L_1 = 3.11 nH; C_1 = 0.0838 pF; R_1 = 0.226 Ω; L_1' = 2.66 nH; C_1' = 0.0978 pF; R_1' = 0.194 Ω; R_{ext} = 8.25 Ω. 45

Figure 3.13: S Parameters of the filter and filter/antenna using equivalent circuit. 45

Figure 3.14: (a) Schematic of the filter using CPW feeding. Picture of the (b) top and (c) back side. (L_1 = 14.0 mm; L_2 = 14.4 mm; W = 13 mm; W_1 = 5.4 mm; W_2 = 4.5 mm; L_{cpw} = 7.4 mm; L_{coup} = 3.4 mm; W_{cpw} = 1.5 mm; g = 0.5 mm) 46

Figure 3.15: (a) Schematic of the filter/antenna using CPW feeding. Picture of the (b) antenna and (c) back side. (L_1 = 14.0 mm; L_2 = 14.4 mm; L_3 = 14.5 mm; L_4 = 9.8 mm; W = 13 mm; W_1 = 5.4 mm; W_2 = 4.5 mm; W_3 = 5.3 mm; L_{cpw} = 7.4 mm; L_{coup} = 3.4 mm; W_{cpw} = 1.5 mm; g = 0.5 mm; W_a = 1 mm; L_a = 12.1 mm; P_a = 2.3 mm) 47

Figure 3.16: Simulated S_{11} and S_{21} of the filter shown in Fig. 3.14. Simulated S_{11} and gain (at boresight) of the filter/antenna shown in Fig. 3.15. 48

Figure 3.17: Simulated S_{11} and S_{21} of the filter shown in Fig. 3.14 with a shielding cap. Simulated S_{11} and gain (at the boresight) of the filter/antenna shown in Fig. 3.15 with shielding caps. 48

Figure 3.18: Simulated and measured responses of the (a) filter and (b) filter/antenna using coaxial feeding. The gain is at the boresight..... 50

Figure 3.19: Simulated and measured radiation patterns of the filter/antenna using coaxial feeding at f_0. 52

Figure 3.20: Simulated and measured wide-band response of the filter/antenna using coax feeding..... 52

Figure 3.21: Simulated and measured (a) filter responses, and (b) filter/antenna S_{11} and gain at boresight (CPW feeding without shielding cap) 53

Figure 3.22: Simulated and measured (a) filter responses, and (b) filter/antenna S_{11} and gain at boresight. (CPW feeding with shielding cap) 54

Figure 3.23: CPW fed filter/antenna radiation patterns at f_0. (a) without, and (b) with a shielding cap. 55

Figure 3.24: Schematic of the resonator/antenna with slot antenna on (a) top and (b) side. 58

Figure 3.25: Cavity Model schematic of the resonator/antenna. 58

Figure 3.26: Extracted Q_{ext} of the resonator/antennas in Fig. 3.24 versus cavity width W for different h with (a) $\varepsilon_r = 1$, (b) $\varepsilon_r = 2.2$, and (c) $\varepsilon_r = 4$. 63

Figure 4.1: Schematic of a phased array with integrated filter/antenna. 65

Figure 4.2: Exploded view of a vertical two-pole cavity filter with CPW feeding. SMA connectors are soldered to the CPW lines for measurement purposes. 66

Figure 4.3: (a) Stack and (b) top view of the vertical filter. (Dimensions are in millimeters. h_1 = 1.524; h_2 = 0.762; h_3 = 0.508; h_4 = 0.254; prepreg thickness = 0.1; L_{CPW} = 5.6; L_{Coup} = 1.2; g = 0.4; L_c = 9; W_c = 12.5; D = 1; S = 1.3; L_s = 3.9; W_s = 0.5; Y_s = 0.5) 67

Figure 4.4: Exploded view of a vertical two-pole cavity filter seamlessly integrated with a slot antenna. 69

Figure 4.5: Magnetic field distribution at the top of (a) an unperturbed resonator and (b) the upper resonator of the filter antenna. (Dimensions are in millimeters. L_c = 9; W_c = 12.5; L_s = 4; W_s = 0.5; Y_s = 0.5; L_a = 9.5; W_a = 0.5; X_a = 3.3; X_{via} = 2.2; Y_{via} = 0.7) 70

Figure 4.6: Schematics of a cavity resonator terminated with (a) a slot antenna or (b) a 50-ohm port excited by a waveguide port. 71

Figure 4.7: Reflection coefficients of the waveguide port for the upper cavity terminated with either a slot antenna (Fig. 4.6(a)) or a filter port (Fig. 4.6(b)). 72

Figure 4.8: Simulated filter and filter/antenna responses in (a) frequency domain and (b) time domain 75

Figure 4.9: Equivalent circuits of the structures (a) in Fig. 4.6 and (b) in Figs. 2&4. (Filter: L_1 = L_2 = 3 nH, C_1 = 0.0815 pF, C_2 = 0.0816 pF, R_1 = R_2 = 0.979 Ω, K_{01} = K_{23} = 13.3 Ω, K_{12} = 4.02 Ω, Z_0 = 50 Ω) (Filter/Antenna: L_1 = L_2 = 3 nH, C_1 = C_2 = 0.0815 pF, R_1 = 0.979 Ω, R_2 = 1.03 Ω, K_{01} = 13.3 Ω, K_{12} = 3.9 Ω, K_{23} = 12.7 Ω, Z_0 = 50 Ω) 77

Figure 4.10: (a) Filter S_{11} and S_{21} using HFSS simulation and equivalent circuit. (b) Filter/antenna S_{11} and gain using HFSS simulation as well as filter/antenna S_{11} and S_{21} using equivalent circuit. 78

Figure 4.11: (a) Photo of fabricated filter/antenna, and (b) Simulated and measured S_{11} and gain 81

Figure 4.12: Measured and simulated radiation patterns of the filter/antenna at f_0. 82

Figure 5.1: Schematic of a three-pole cavity filter integrated with an aperture antenna over a ground plane 85

Figure 5.2: Top view of an integrated cavity filter with an aperture antenna. 34% FBW on 3.17-mm thick substrate 85

Figure 5.3: Schematic of the resonator/antenna with aperture on (a) side and (b) top. 87

Figure 5.4: Normalized impedance of the resonator/antenna compared with a series *RLC* circuit. 87

Figure 5.5: Equivalent circuit of the filter/antenna system. 88

Figure 5.6: Extracted Q_{ext} of the resonator/antennas in Figure 5.3 versus aperture width W for different h with (a) $\varepsilon_r = 1$, (b) $\varepsilon_r = 2.2$, and (c) $\varepsilon_r = 4$. 90

Figure 5.7: Electric field away from the aperture for $\varepsilon_r = 1$ and 2.2. 92

Figure 5.8: Variation of Q_{ext} of the resonator/antenna in Fig. 5.3(a) versus L_D for $\varepsilon_r = 1$, 2.2, and 4. The substrate thickness $h = 3.17$ mm. 92

Figure 5.9: Simulated E-plane radiation patterns of an air-filled resonator/antenna over an infinite ground plane for two different substrate thicknesses. 94

Figure 5.10: Simulated E-plane radiation patterns of an air-filled resonator/antenna over finite ground planes of different lengths L_D. ($W = 18$ mm, $h = 3.17$ mm) 94

Figure 5.11: Simulated E-plane radiation patterns of a dielectrically-filled resonator/antenna for different L_D. ($\varepsilon_r = 2.2$, $W = 15$ mm, $h = 3.17$ mm) 95

Figure 5.12: Simulated responses of a 34% three-pole integrated filter with an aperture antenna on 3.17-mm-thick Rogers RT/Duroid 5880. 97

Figure 5.13: Simulated radiation patterns of the 34% integrated filter/antenna at f = (a) 9 GHz, (b) 10 GHz, and (c) 11 GHz. 98

Figure 5.14: Photos of the fabricated filter/antenna. (a) With and (b) without the shielding cap. 100

Figure 5.15: Simulated and measured responses of the three-pole integrated filter with an aperture antenna at 8-12 GHz. 100

Figure 5.16: Simulated and measured responses of the three-pole integrated filter with an aperture antenna at 8-18 GHz. 101

Figure 5.17: Simulated and measured radiation patterns of the 8% integrated filter with an aperture antenna in (a) H-plane and (b) E-plane at the center frequency. 101

Figure 6.1: (a) Skew and (b) top view of a three-pole cavity filter integrated with a monopole antenna. (W = 13; P_p = 2.3; W_1 = 5.5; W_2 = 5.6; L_{r1} =15.5; L_{r2} = 13.6; L_{r3} = 16.5; P_a = 3.2, c = 6.5; L_a = 7; h = 1.57) Dimensions are in mm. 104

Figure 6.2: (a) Schematic of a waveguide excited by a coaxial probe and (b) its equivalent circuit. (W = 13, c = 6.5, h = 1.57) Dimensions are in mm. 106

Figure 6.3: (a) Resonator/antenna structure. (b) Equivalent circuit of the resonator/antenna. (c) Simplified equivalent circuit. (c) Equivalent series *RLC* circuit. 106

Figure 6.4: Z_{shunt} for a monopole antenna of length L_a = 7 mm. 108

Figure 6.5: Input impedance of the cavity resonator with a monopole antenna. 108

Figure 6.6: Extracted Q_{ext} versus monopole antenna position P_a for antenna lengths L_a = 6, 7, and 8 mm. 110

Figure 6.7: Equivalent circuit of the three-pole integrated filter/antenna system (K_{01} = 2.87 Ω, K_{12} = 0.182 Ω, K_{23} = 0.19 Ω, L_{r1}' = L_{r2}' = 16.1, P_a = 3.2, L_{r3}' = 17.8). Dimensions are in mm. 111

Figure 6.8: Lumped element equivalent circuit of the filter/antenna. (K_{01} = 2.87 Ω; K_{12} = 0.182 Ω; K_{23} = 0.19 Ω; L_1 = L_2 = 63.2 pH; C_1 = C_2 = 4 pF; R_{o1} = R_{o2} = 5.67 mΩ; L_3 = 69 pH; C_3 = 3.67 pF; R_{o3} = 6.2 mΩ; R_{ext} = 0.178 Ω. 111

Figure 6.9: Simulated and measured responses of the three-pole integrated filter with a monopole antenna. 114

Figure 6.10: Simulated and measured wideband responses of the three-pole integrated filter with a monopole antenna. 114

Figure 6.11: Simulated and measured radiation patterns of the integrated filter with a monopole antenna in (a) H plane and (b) E plane at the center frequency. 115

Figure 7.1: Exploded view of a vertically-integrated three-pole filter/antenna with two cavity resonators and one patch antenna. 117

Figure 7.2: Schematics of (a) SMA coaxial feeding and coupling slot; (b) coupling slot and via; (c) coupling via and patch antenna; and (d) vertical stack. (W = 12.9; P_c = 2.7; L_s = 5.7; W_s = 0.5;

X_s = 0.9; L_{r1} = 15.7; L_{r2} =16; P_p = 3.1; c = 6.5; d = 2.3; L_p = 9.1; W_p = 14; h_1 = 1.6; h_2 = 0.8) Dimensions are in mm. 120

Figure 7.3: (a) Schematic of a waveguide excited by a coaxial probe and (b) its equivalent circuit. 122

Figure 7.4: The equivalent circuit of a probe-fed patch antenna. 123

Figure 7.5: Equivalent circuit of the filter/antenna system. 125

Figure 7.6: Simplified equivalent circuits of the filter/antenna system (K_{01} = 0.469 Ω, K_{12} =0.208 Ω, L_{r1}' = 15.4 mm, L_{r2}' = 16.8 mm, P_p = 2.9 mm). 125

Figure 7.7: Equivalent circuit of the patch antenna coupled to the middle cavity resonator. 127

Figure 7.8: Lumped element impedance inverters. 127

Figure 7.9: Transformation of the equivalent circuit in Fig. 7.7 to the conventional form of two series resonators coupled by an impedance inverter. 128

Figure 7.10: Simulated impedance of a probe-fed patch antenna and its equivalent *RLC* model (C_p = 1.882 pF, L_p = 0.135 nH, R_r = 147.1 Ω, R_l = 4961.7 Ω, n_2 = 0.695, X_2 = 29 Ω) 132

Figure 7.11: (a) Schematic of a patch antenna coupled to a waveguide through a coupling via and (b) its equivalent circuit. 132

Figure 7.12: Simulated impedance of the patch antenna in Fig. 7.11(a) as seen from the waveguide and its equivalent *RLC* model (C_p' = 0.318 nF, L_p' = 0.802 pH, R_p' = 0.840 Ω, X_s = 0.576 Ω) 133

Figure 7.13: The reactances X_s and X_p compared with ($\omega L_2 - 1/\omega C_2$) showing a slower variation with frequency. 133

Figure 7.14: Simulated S_{11} and S_{21} of the reference filter compared to simulated S_{11} and gain of the filter/antenna shown in Fig. 7.1. 134

Figure 7.15: Time domain S_{11} responses of the reference filter and the filter/antenna shown in Fig. 7.1. 135

Figure 7.16: Photos of the fabricated filter/antenna system. 139

Figure 7.17: Simulated and measured responses of the three-pole vertically integrated filter with a patch antenna. 140

Figure 7.18: Simulated and measured radiation patterns in (a) H-plane and (b) E-plane at the center frequency. 140

Figure 7.19: Simulated input reflection coefficients of individual filter/antenna elements in a 1 × 4 array. 142

Figure 7.20: Simulated radiation patterns of the 1 × 4 filter/antenna array in both H- and E-planes at the center frequency. 142

1 INTRODUCTION

1.1 Motivation

Microwave systems have a wide range of usage, ranging from everyday applications such as satellite television and mobile phones to military radar systems. In recent years, there has been a rapid growth in existing wireless communication systems, in addition to the emergence of new technologies. In order to continue to make efficient use of the available electromagnetic spectrum, high performance transceivers with more stringent electrical specifications are increasingly needed. Moreover, transceivers are required to be more compact, lighter in weight and lower in cost.

Filters and antennas are indispensable components in any communications and radar system, which typically take up considerable volume in the system transceivers. In the past, a lot of research has been conducted to improve the electrical performance, and compactness of filters and antennas. New materials and fabrication techniques such as high-temperature superconductors, low-temperature cofired ceramics (LTCC)[1, 2], stereolithography [3, 4], and micromachining [5] have been used to improve the performance of filters. In addition, due to the growing demand for compact, yet efficient antennas, there has been a renewed interest in the field of electrically small antennas in recent years as evident by the large number of publications in the literature .

Fig. 1.1 shows the block diagrams of the transmitter and receiver of a typical wireless communications system. A bandpass filter immediately following the antenna in the receiver circuit is utilized to reject out-of-band noise and interference while allowing the transmission of

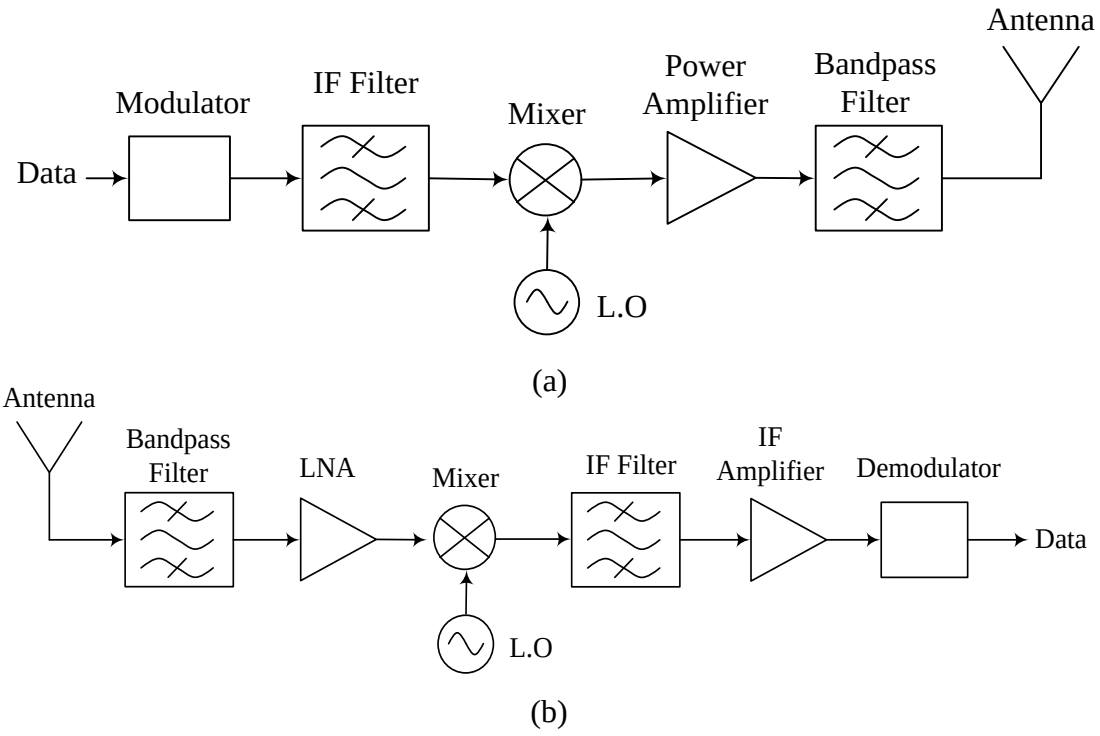

Figure 1.1: Block diagram of (a) transmitter, and (b) receiver of a communications system.

in-band signals. Similarly on the transmitter side, a bandpass filter following the power amplifier is used to filter out any spectral components outside the desired frequency band in order to satisfy regulatory requirements on out-of-band radiation. Undesired spectral components include intermodulation products and harmonics generated by nonlinearities of the transmitter circuitry.

An important characteristic of a filter is its out-of-band rejection, which describes the degree by which noise and unwanted signals outside the passband of a filter are attenuated. Generally, the out-of-band rejection is improved by using a larger number of resonators within the filter structure. Equally important is the filter insertion loss, which is proportional to the number of resonators, and inversely proportional to the resonator quality factors and the overall bandwidth of the filter. For a given bandwidth, a highly selective filter requires the usage of a large number of resonators, which can lead to increased insertion loss unless high-Q resonators are utilized.

High-Q resonator filters are therefore necessary in high-performance transceivers in which both high selectivity and low insertion loss are needed.

Waveguide and dielectric resonator filters are commonly used high-Q filters. In spite of their high Q factors (> 2000), waveguide filters have the disadvantage of being bulky, heavy, and not easy to fabricate and integrate with other circuitry. Dielectric resonator filters, utilizing dielectric materials with typical dielectric constants between 20 and 80, are smaller in size. Although temperature-stable dielectrics are more available nowadays, the sensitivity of dielectric resonator filters to temperature and other factors such as humidity remains to be their main disadvantage. Due to their sensitivity, precisely controlled fabrication techniques and unavoidable tuning procedures are needed in the realization of dielectric resonator filters , which render them rather costly and not readily available to many applications.

On the other hand, filters composed of resonators realized using planar transmission lines such as microstrip and coplanar waveguide (CPW) lines are low profile, and easily fabricated using lithography techniques. However, Q factors realized using planar resonators are generally limited (<300) due to high radiation loss, and increased metal loss particularly for CPW line resonators.

In order to attain many of the advantageous features of both waveguide and planar filters, waveguiding structures with reduced height substrates such as substrate integrated waveguides (SIW) have become more popular recently [6],[7]. A SIW is a waveguide realized on a dielectric substrate, in which two rows of closely-spaced metalized vias form the waveguide sidewalls. With the use of such vias, cavity resonators can also be formed in SIW technology. SIW cavities generally exhibit lower Q factors compared with conventional air-filled cavity resonators, due to

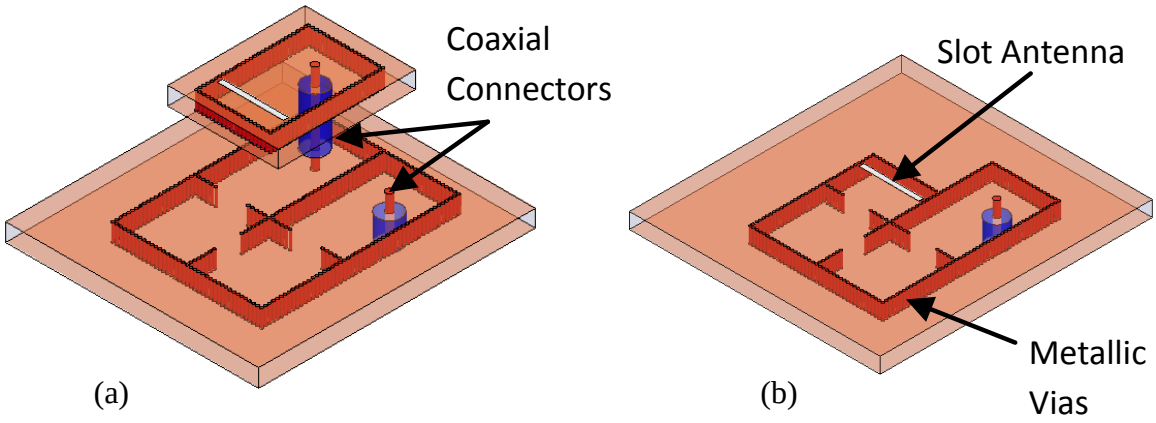

Figure 1.2: Schematics of (a) a SIW cavity filter connected with a cavity-backed slot antenna using coaxial connectors; (b) an integrated filter/antenna system.

the increased metallic losses in the thinner cavities, and additional dielectric losses otherwise absent in air-filled cavities. Nevertheless, the obtained Q factors are usually much higher than those of planar resonators and can be as high as 1000. Unlike conventional waveguides, however, SIW structures are more easily integrated with other systems, and can be fabricated using common printed circuit board (PCB) processes. Due to the aforementioned advantages of SIW, extensive use of this technology is made in this dissertation. The underlying principles, however, are general and can be readily extended to other technologies.

Traditionally, filters and antennas are individually designed and subsequently cascaded using standard 50-ohm connectors. Even when the filter and antenna are individually considered to have acceptable performances, a simple cascade of the two using a 50-ohm transmission line does not present an optimum solution. Fig. 1.2 (a) shows a SIW cavity filter connected with a cavity-backed slot antenna using a coaxial connector. It is rather evident that the cascade approach yields bulky structures, particularly for 3-D filters and antennas. Furthermore, the losses of the 50-ohm transition degrade the overall efficiency and noise factor of the system. Another drawback of the simple cascade approach is the deterioration of the return loss at the

filter input due to the antenna presenting an impedance different from 50 ohms at the filter output. This happens if the antenna bandwidth is smaller than the filter bandwidth. In such cases, the antenna input impedance is close to 50 ohms at the center frequency f_o of the antenna but differs from 50 ohms as we move away from f_o. More importantly, a similar situation occurs in relatively wideband antennas. Due to the difficulties in maintaining an impedance match over a large frequency span, antenna designers are usually satisfied with input voltage standing wave ratios (VSWR) of 2 or 3 corresponding to input reflection coefficients (S_{11}) of -10 dB and -6 dB, respectively. In order to demonstrate the effect of antenna mismatch on the return loss of the filter, an SIW filter and a cavity backed slot antenna are designed at f_o = 9.85 GHz and then cascaded as shown in Fig. 1.2 (a). The designed filter has a 6% 3-dB bandwidth, and a midband insertion loss of 0.58 dB corresponding to an efficiency of 87 %. The antenna bandwidth is 3.1% (VSWR<2), or 5.5% (VSWR<2), and an efficiency of 96% (-0.16 dB) at the center frequency f_o. The responses of the filter and antenna are plotted in Fig. 1.3 (a). Fig. 1.3 (b) shows S_{11} at the filter input of the cascaded system. The deterioration of the input S_{11} of the cascaded system is apparent. It is important to note that an antenna S_{11} of -10 dB, which is usually considered to be a good matching criterion, is insufficient to preserve the matching at the filter input. In addition to degrading the overall system efficiency, the higher reflections result in higher VSWRs at the input line which are highly undesirable especially in high power applications. Furthermore, due to the filter presenting a source/load impedance different from 50 ohms to the LNA/power amplifier, their optimum performance is disrupted.

Integration of filters and antennas into single inseparable units can eliminate the transition between the otherwise separate structures, resulting in more compact and efficient systems. Being co-designed, integrated filter/antenna systems can be more easily designed so as to

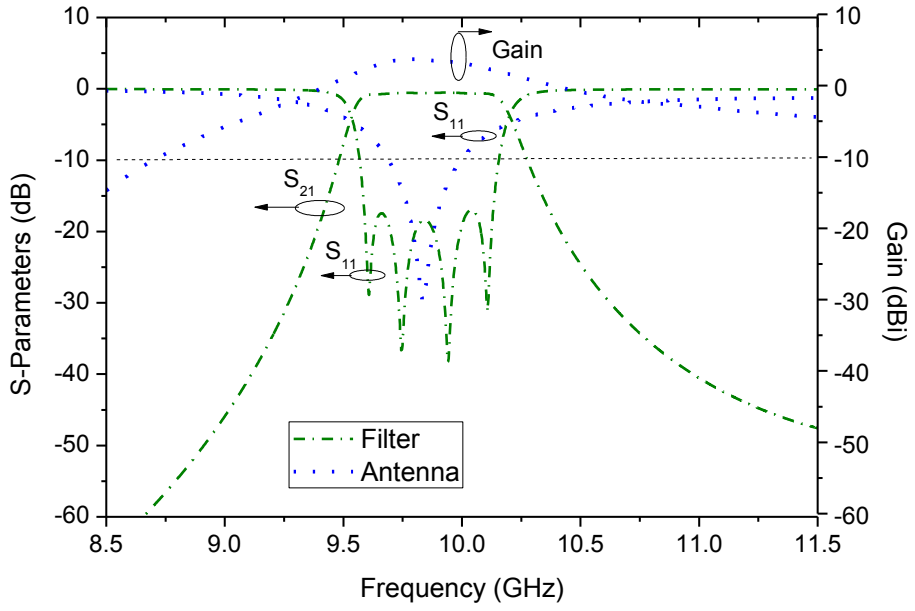

(a)

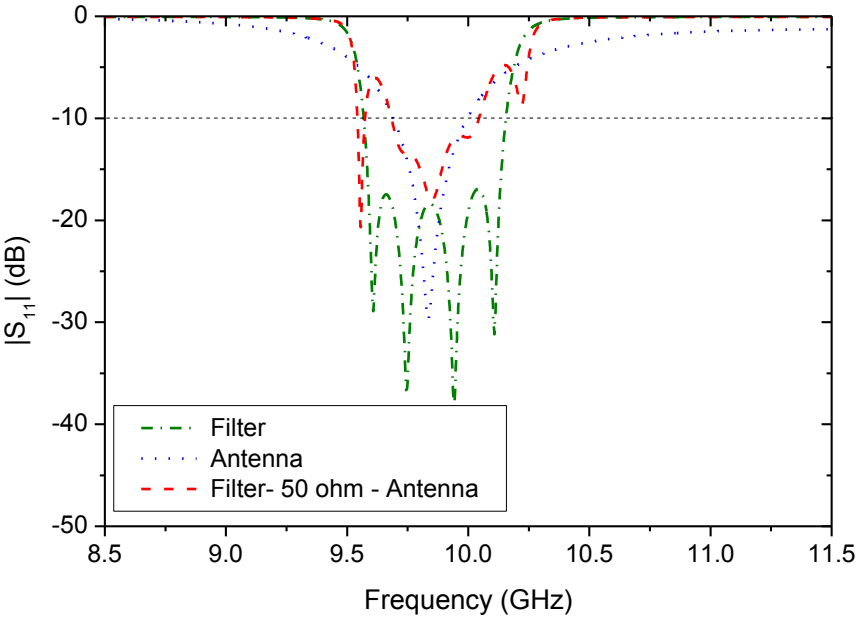

(b)

Figure 1.3: (a) responses of discrete filter and antenna; and (b) S_{11} response of the cascaded system compared with the discrete filter.

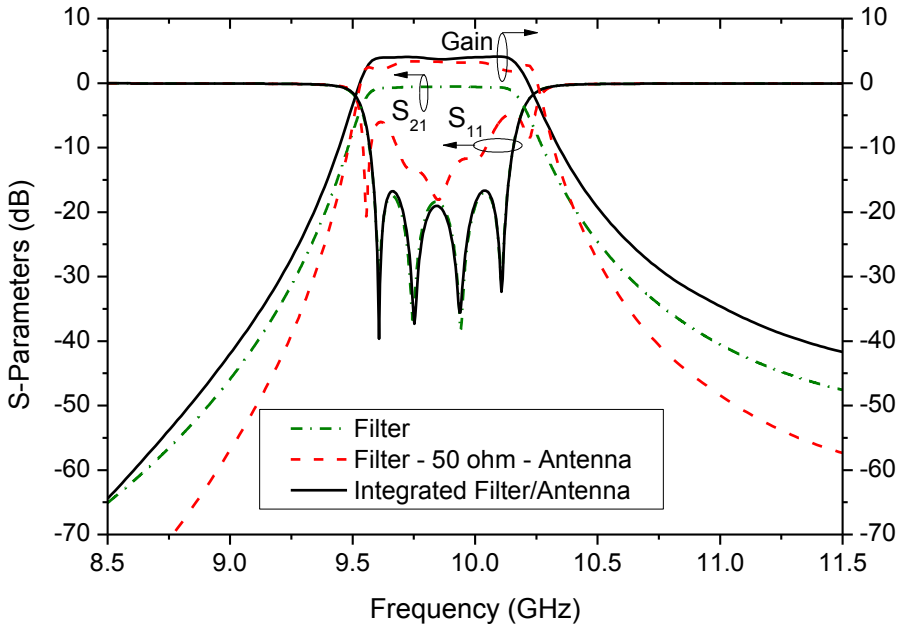

Figure 1.4: Comparison of the responses of the discrete filter, cascaded filter with antenna, and the integrated filter/antenna.

maintain a good impedance match within the passband. Fig. 1.2 (b) shows the integrated filter/antenna alternative of the cascaded system in Fig. 1.2 (a), in which the slot antenna does not occupy any additional volume. In such integrated structures, it is possible to preserve the quality of filtering and radiation characteristics. Fig. 1.4 shows S_{11} and the gain of the integrated filter/antenna and compares them with the responses of the filter and the cascaded system. It is seen that the integrated/filter antenna can be designed to have the same filtering characteristics of the filter, as evidenced by the closely matching S_{11} responses, and the same filtering shape exhibited by the gain and S_{21} of the filter/antenna and filter, respectively. In this particular filter/antenna structure, the overall system efficiency is found to be 87% which matches exactly the insertion loss of the filter. This means that the integration of the filter and antenna did not introduce any additional losses, and in this sense, we were able to achieve a 100% efficient radiator. Although this is not always possible, the efficiency of the integrated system is always

found higher than the efficiency of the corresponding cascaded system.. At the center frequency f_o, where the reflection from the antenna is minimum, the efficiency of the cascaded system is (-0.58 dB - 0.2 dB - 0.16 dB = -1.38 dB), where -0.16 dB is the efficiency of the antenna, and 0.2 dB is the assumed insertion loss of for the coaxial connector. This corresponds to an overall system efficiency of 73% compared with 88% (-0.58 dB) for the integrated filter/antenna.

The demonstrative example provided above demonstrates the advantages of high efficiency and reduced form factors gained by integrating high-Q filters with antennas, and will therefore be our main focus in this dissertation.

1.2 Literature Review

In an effort to realize structures that combine the filtering and radiation functions of the filter and antenna, respectively, different approaches have been followed by researchers. In [8], Lee *et al.* demonstrated a vertical three-pole cavity filter integrated with a patch antenna inside low-temperature cofired ceramic (LTCC) substrates. The filter and antenna were designed separately using 50-ohm ports and then connected together through a slot-to-microstrip transition avoiding coaxial connectors. The transition caused significant connection losses and strongly detuned the filter response due to the antenna loading effect.

In another approach, the aperture of a horn antenna was covered with a substrate integrated waveguide (SIW) cavity frequency selective surface (FSS) [9]. In [10], a filtering function was incorporated into a horn antenna using metallic posts that formed resonant cavities within the horn. Being bulky, however, the use of horn antennas is limited to certain applications.

The integration of patch antennas with coplanar waveguide (CPW) and microstrip resonator filters was reported in [11-13].The antennas acted as radiators and additional resonators

simultaneously, and therefore higher-order filtering functions were achieved with a reduced number of resonators inside the filter. In [11], a third-order filtering function is incorporated into a CPW-fed patch antenna by the addition of open-circuited half-wavelength microstrip resonators on a different dielectric layer. The microstrip resonators were electrically connected to the CPW line using metalized vias. The need for multilayers was removed in [12] by using CPW resonators patterned on the ground plane of the patch, and therefore a single dielectric substrate was used.

More recently, the integration of a coupled line microstrip filter with an inverted L antenna was demonstrated [14]. The inverted L antenna is utilized as an additional series resonator in a microstrip coupled line filter. The main disadvantage of the integrated filter/antenna systems in [11-14] is the very limited Q factor performance, associated with the planar resonator structures used. Furthermore, radiation from the transmission line resonators can significantly degrade the out-of-band performance. Better performance is obtained using high-Q 3D integrated filter/antenna structures as will be shown in this dissertation. Despite the advantages of high-Q filters compared with their planar counterparts, very few designs utilizing such structures have been reported in the literature. Xun Gong et al presented the integration of a high-Q EBG filter and slot antenna in a seamless manner [15]. However in that work, no systematic design procedure was described and only simulation data was shown.

1.3 Dissertation Overview

This dissertation presents the integration of high-Q 3D filters with efficient antennas. Chapter 2 presents some of the theoretical background needed in designing filters and integrated filter/antennas. Microwave filters are studied with the aid of coupled mode theory, a theory usually used to study optical nonlinearities and acoustic/optical wave interactions. The

unconventional treatment stresses the underlying physical principles and provides a deeper understanding of phenomena involved in coupled resonator structures. Chapter 3 presents the integration of cavity filters with slot antennas. In this chapter, the cavity resonators are realized on a single dielectric substrate in a planar form. To further reduce the footprint of the integrated filter/antenna systems, slot antennas are integrated with vertical cavity filters in Chapter 4. In Chapter 5, a new antenna structure is used that enables the design of filter/antenna systems with larger bandwidths compared with those presented in Chapters 3 and 4. The antenna consists of an open-ended aperture mounted on a ground plane. The enhanced bandwidth is made possible through the excitation and radiation of surface waves. In Chapter 6, we integrate cavity filters with monopole antennas to obtain omnidirectional radiation patterns. Finally, in Chapter 7, the integration of filters with patch antennas is presented.

2 APPLICATION OF COUPLED-MODE THEORY TO FILTER ANALYSIS

2.1 Introduction

Integrated filter/antenna systems can be synthesized utilizing similar design approaches used for coupled resonator bandpass filters. The response of a filter, as we shall see, is determined by the resonant frequencies of the resonators, the inter-coupling coefficients k_{ij} between the resonators, and the external Q factors Q_{ext} of the first and last resonators. Different from a filter structure, the last resonator of the filter/antenna couples to a radiating antenna instead of a second port. In this chapter, we will briefly review some of the basic principles of microwave filters that are equally applicable to integrated filter/antenna structures. For a more detailed treatment, the reader is referred to the available textbooks on the subject [16-18].

Typically, at microwave frequencies, filters are realized using inter-coupled resonators such as cavity [19] and dielectric resonators [20].The most commonly used approach to design such structures is based on low-pass prototypes [16]. Low-pass prototypes are ladder networks made of lumped capacitors and inductors which are synthesized to achieve desired filtering functions. The element values of the low-pass prototypes of specific pass band characteristics such as maximally flat and Chebyshev responses with different ripple are tabulated [16]. The element values are normalized with respect to low-pass filter parameters such as the cut-off frequency and the source impedance. Low-pass prototypes can be transformed into bandpass, high-pass, and bandstop filters by using appropriate frequency transformations [16]. Based on this approach, resonators of bandpass filters are coupled in a cascade configuration, from which all-pole filtering characteristics are obtained.

More general filtering functions can be realized provided couplings between non-adjacent resonators are used. Analysis and synthesis of cross-coupled resonator filters are commonly performed with the aid of coupling matrix techniques [21, 22].

In this chapter, we utilize a coupling of modes formulation to analyze and synthesize microwave filters. This formalism, introduced by Haus [23], is a general method by which coupled resonant modes or propagating modes can be analyzed. The formalism has the advantage of being simple, utilizing very few basic physical concepts, in addition to using a minimum of algebra. It has been used in the treatment of optical nonlinearities and the interaction of optical waves with acoustic waves [23].

The main features of this formalism are highlighted and its use as applied to microwave filter design is then discussed. For demonstration purposes, a two-pole filter is analyzed using the coupling of modes formalism. The results are then compared with the results of the commonly used coupling matrix method. The two approaches are found to yield identical results apart from different frequency variables. Unlike the coupling matrix approach, however, the presented coupling of modes approach does not require an equivalent circuit model in its formulation. Instead, the approach uses the concepts of conservation of energy and the time-reversibility of Maxwell's equation, which in our opinion, not only makes it more general, but also stresses the physical principles and provides a deeper understanding of phenomena involved in coupled resonator systems.

In section 2.3.3, closed-form expressions for the insertion loss of filters up to fifth order are derived using the coupled-mode approach. The developed expressions provide an accurate means

to evaluate the insertion loss of filters in terms of the external Q factors Q_{ext}, the inter-resonator coupling coefficients k_{ij}, and the unloaded Q factors Q_{oi}.

2.2 Coupled-Mode Theory Review

In this section, the coupled-mode theory developed by Haus is briefly reviewed. For a detailed discussion of the theory, the reader is referred to the original work [23].

By initially considering an isolated lossless resonator, Haus introduces the positive-frequency component of a mode amplitude a, which is related to the energy W stored in the resonator through:

$$W = |a|^2 \tag{2.1}$$

The time evolution of the mode amplitude a is described by the differential equation:

$$\frac{da}{dt} = j\omega_o a \tag{2.2}$$

In order to account for effects such as internal energy dissipation inside the resonator, coupling of the resonator to an external port, and/or coupling to another resonator, equation (2.2) is modified in a perturbative manner. To account for internal energy dissipation in the resonator, (2.2) is modified according to:

$$\frac{da}{dt} = j\omega_o a - \frac{a}{\tau_o} \tag{2.3}$$

where $1/\tau_o$ is the rate of decay due to loss. When the resonator is coupled to an external port, (2.3) is modified to account for two effects, namely, the escape of power back into the port, and

the buildup of energy in the resonator due to a possible incident wave. Equation (2.3) now becomes:

$$\frac{da}{dt} = j\omega_o a - \left(\frac{1}{\tau_o} + \frac{1}{\tau_e}\right)a + \kappa \cdot s^+ \tag{2.4}$$

where $1/\tau_e$ is the decay rate due to power escaping to the port written in terms lifetime τ_e, κ is a coupling coefficient that represents the degree of coupling of the incident wave to the resonator mode, and $|s^+|^2$ represents the power carried by the incident wave. Using the property of time-reversibility of Maxwell's equations, Haus shows that κ and τ_e are related up to a relative phase factor as:

$$\kappa = \sqrt{\frac{2}{\tau_e}} \tag{2.5}$$

If two resonators resonant at ω_o are coupled, each being also connected to an external port, the differential equations describing the mode amplitudes of the two resonators labeled 1 and 2 respectively, are given by:

$$\frac{da_1}{dt} = j\omega_o a_1 - \left(\frac{1}{\tau_{o1}} + \frac{1}{\tau_{e1}}\right)a_1 + \kappa_{12}a_2 + \sqrt{\frac{2}{\tau_{e1}}} \cdot s_1^+ \tag{2.6}$$

$$\frac{da_2}{dt} = j\omega_o a_2 - \left(\frac{1}{\tau_{o2}} + \frac{1}{\tau_{e2}}\right)a_2 + \kappa_{21}a_1 + \sqrt{\frac{2}{\tau_{e2}}} \cdot s_2^+ \tag{2.7}$$

By considering two coupled lossless resonators, which are isolated from any external ports, and noting that the total energy $|a_1|^2 + |a_2|^2$ under such circumstances must be conserved, Haus shows that κ_{12} and κ_{21} are related according to:

$$\kappa_{12} + \kappa_{21}^{*} = 0 \tag{2.8}$$

Finally, the reflected wave s_1^- at the port coupled to resonator 1 can be evaluated using:

$$s_1^- = -s_1^+ + \sqrt{\frac{2}{\tau_{e1}}} a_1 \tag{2.9}$$

and similarly for s_2^-. The derivation of equation (2.9) makes use of the linearity of the system, by which s_1^- is written as a linear combination of s_1^+ and a_1. The coefficient of a_1, namely $\sqrt{2/\tau_{e1}}$, is obtained by noting that the power that escapes from a lossless resonator into a coupling port in the absence of an incident wave is:

$$\left|s_1^-\right|^2 = -\frac{d\left|a_1\right|^2}{dt} = \frac{2}{\tau_{e1}}\left|a_1\right|^2 \tag{2.10}$$

where the second equality is obtained using (2.6) in its special form:

$$\frac{da_1}{dt} = j\omega_o a_1 - \frac{1}{\tau_{e1}} a_1 \tag{2.11}$$

By noting that the power delivered to the lossless resonator in the presence of an incident wave must equal the time rate of change of the energy stored, a statement mathematically expressed as:

$$\left|s_1^+\right|^2 - \left|s_1^-\right|^2 = \frac{d\left|a_1\right|^2}{dt} \tag{2.12}$$

the negative unity coefficient of s_1^+ is earned.

Equations (2.6),(2.7), and (2.9) are the workhorse equations of coupled-mode theory. Equations (2.6), (2.7) can be solved for the mode amplitudes a_1 and a_2 for arbitrary excitation functions s_1^+,

and s_2^+ . The reflected waves s_1^-, and s_2^- can then be obtained using equation (2.9) once a_1 and a_2 are found.

2.3 Coupled-Mode Theory Applied to Filters

In this section, we apply the coupled-mode theory described in section 2.2 to the analysis of microwave filters. Before we do so, however, we first give the relation between the lifetimes τ*'s*, and the κ_{ij} used by Haus and the corresponding Q factors and coupling coefficients k_{ij} more commonly used in filter work. The lifetime τ is related to the corresponding Q factor using:

$$\tau = \frac{2Q}{\omega_o} \tag{2.13}$$

The coupling coefficient κ_{ij} is given in terms of k_{ij} by:

$$\kappa_{ij} = j\frac{\omega_o}{2}k_{ij} \tag{2.14}$$

Using (2.14), the condition (2.8) translates to $k_{ij} = k_{ji}$.

To demonstrate the use of coupled-mode theory, a two-pole filter composed of two coupled resonators resonant at ω_o, and having generally different unloaded Q factors, Q_{o1} and Q_{o2}, is analyzed. Assuming a time-harmonic incident wave $s_1^+ = S_1^+ e^{j\omega t}$ at port 1 and matched conditions at port 2 ($s_2^+ = 0$), a system of equations in terms of the two unknown complex amplitudes A_1 and A_2 , where $a_1 = A_1 e^{j\omega t}$, and $a_2 = A_2 e^{j\omega t}$, can be obtained using (2.6) and (2.7) as:

$$\left(j2\frac{\omega-\omega_o}{\omega_o} + \frac{1}{Q_{ext,1}} + \frac{1}{Q_{o1}}\right)A_1 - jk_{12}A_2 = \frac{2}{\sqrt{\omega_o Q_{ext,1}}}S_1^+ \tag{2.15}$$

$$-jk_{21}A_1+\left(j2\frac{\omega-\omega_o}{\omega_o}+\frac{1}{Q_{ext,2}}+\frac{1}{Q_{o2}}\right)A_2=0 \tag{2.16}$$

where (2.13) and (2.14) have been used. By inverting (2.15) and (2.16), A_1 and A_2 are obtained as:

$$A_1=\frac{\frac{2}{\sqrt{\omega_o Q_{ext,1}}}\left[j2\frac{\omega-\omega_o}{\omega_o}+\frac{1}{Q_{ext,2}}+\frac{1}{Q_{o2}}\right]\cdot S_1^+}{\left[j2\frac{\omega-\omega_o}{\omega_o}+\frac{1}{Q_{ext,1}}+\frac{1}{Q_{o1}}\right]\left[j2\frac{\omega-\omega_o}{\omega_o}+\frac{1}{Q_{ext,2}}+\frac{1}{Q_{o2}}\right]+{k_{21}}^2} \tag{2.17}$$

$$A_2=\frac{\frac{2jk_{21}}{\sqrt{\omega_o Q_{ext,1}}}S_1^+}{\left[j2\frac{\omega-\omega_o}{\omega_o}+\frac{1}{Q_{ext,1}}+\frac{1}{Q_{o1}}\right]\left[j2\frac{\omega-\omega_o}{\omega_o}+\frac{1}{Q_{ext,2}}+\frac{1}{Q_{o2}}\right]+{k_{21}}^2} \tag{2.18}$$

In terms of $Q_{ext,1}$ and $Q_{ext,2}$, S_1^- and S_2^- are:

$$S_1^-=-S_1^++\sqrt{\frac{\omega_o}{Q_{ext,1}}}A_1 \quad ; \quad S_2^-=\sqrt{\frac{\omega_o}{Q_{ext,2}}}A_2 \tag{2.19}$$

The S-parameters of the two-port filter are given by:

$$S_{11}=-1+\frac{\frac{2}{Q_{ext,1}}\left[j2\frac{\omega-\omega_o}{\omega_o}+\frac{1}{Q_{ext,2}}+\frac{1}{Q_{o2}}\right]}{\left[j2\frac{\omega-\omega_o}{\omega_o}+\frac{1}{Q_{ext,1}}+\frac{1}{Q_{o1}}\right]\left[j2\frac{\omega-\omega_o}{\omega_o}+\frac{1}{Q_{ext,2}}+\frac{1}{Q_{o2}}\right]+{k_{21}}^2} \tag{2.20}$$

$$S_{21}=\frac{j2k_{21}\Big/\sqrt{Q_{ext,1}\cdot Q_{ext,2}}}{\left[j2\frac{\omega-\omega_o}{\omega_o}+\frac{1}{Q_{ext,1}}+\frac{1}{Q_{o1}}\right]\left[j2\frac{\omega-\omega_o}{\omega_o}+\frac{1}{Q_{ext,2}}+\frac{1}{Q_{o2}}\right]+{k_{21}}^2} \tag{2.21}$$

The results of equations (2.20) and (2.21) show that the response of a filter is completely determined when the resonant frequencies and the unloaded Q factors of the resonators, the inter-coupling coefficients k_{ij}, and the external Q-factors of the first and last resonators are specified.

If a filter of order N having a standard filtering function such as maximally flat, or Chebyshev is to be designed, the external Q-factors and the coupling coefficient k_{ij} are calculated using [16]:

$$Q_{ext,1} = \frac{g_0 g_1}{FBW}; \quad Q_{ext,2} = \frac{g_N g_{N+1}}{FBW} \tag{2.22}$$

$$k_{ij} = \frac{FBW}{\sqrt{g_i g_j}} \tag{2.23}$$

where FBW is the fractional bandwidth of the filter, and g_i are the tabulated low-pass filter prototype element values.

2.3.1 Physical Determination of Q_{ext} and k_{ij}

When a filter structure is to be physically realized, one needs to find the physical parameters required to achieve certain Q_{ext} and k_{ij}. We now describe general methods by which Q_{ext} and k_{ij} can be determined possibly with the aid of full-wave simulations.

Let us first consider a lossless resonator which is coupled to an external port, the differential equation describing this structure is:

$$\frac{da_1}{dt} = j\omega_o a_1 - \frac{1}{\tau_e} a_1 + \sqrt{\frac{2}{\tau_e}} \cdot s_1^+ \tag{2.24}$$

Again, assuming harmonic time dependence $s_1^+ = S_1^+ e^{j\omega t}$, (2.24) can be solved for the amplitude A_1, where $a_1 = A_1 e^{j\omega t}$, and the reflection coefficient S_{11} can then be found using (2.9) as:

$$S_{11} = -1 + \frac{2}{1 + j(\omega - \omega_o)\tau_e} \tag{2.25}$$

Using (2.13), S_{11} in terms of Q_{ext} can be written in the form:

$$S_{11} = \frac{1 - j2\dfrac{\omega - \omega_o}{\omega_o} Q_{ext}}{1 + j2\dfrac{\omega - \omega_o}{\omega_o} Q_{ext}} \tag{2.26}$$

Because the resonator is assumed lossless, the magnitude of S_{11} is equal to 1. The phase of S_{11}, given by:

$$\arg(S_{11}) = -2\tan^{-1}\left(2\frac{\omega - \omega_o}{\omega_o} Q_{ext}\right) \tag{2.27}$$

can be used to extract Q_{ext}. The coupled mode formulation choice of phase results in $\arg(S_{11})$ being zero at $\omega = \omega_o$ similar to a shunt *RLC* circuit. Fig. 2.1 shows a plot of $\arg(S_{11})$ versus frequency for a 10 GHz resonator. The frequencies ω_1 and ω_2 are defined as the frequencies where $\arg(S_{11})$ is $\pi/2$ and $-\pi/2$, respectively. Using (2.27), it is straightforward to show that Q_{ext} is given by:

$$Q_{ext} = \frac{\omega_o}{\omega_2 - \omega_1} \tag{2.28}$$

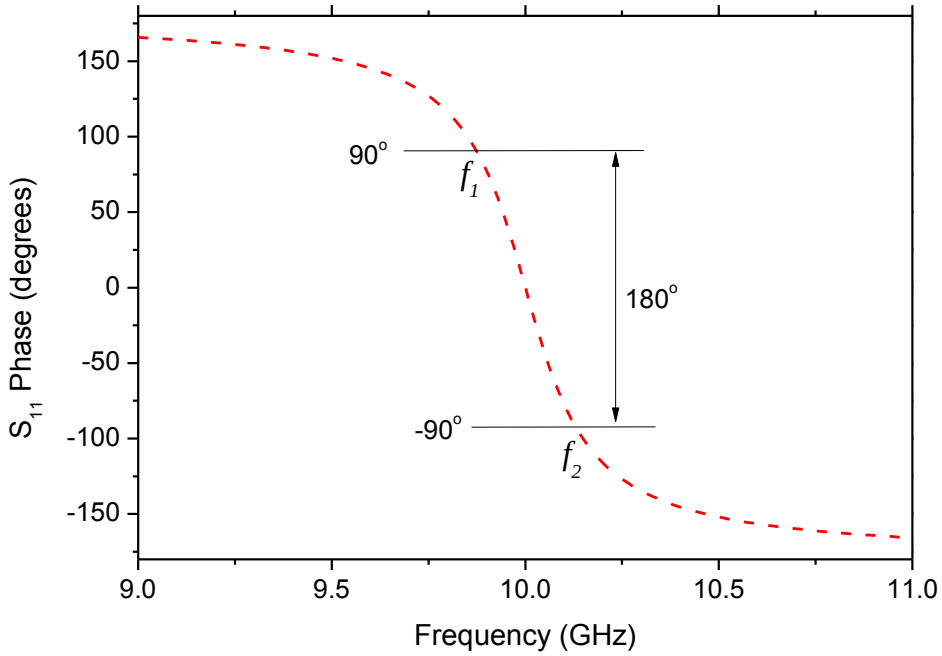

Figure 2.1: Extraction of Q_{ext} from the phase of S_{11}.

In order to determine k_{ij}, we consider two lossless coupled resonators which are disconnected from any external ports and we solve for the natural modes of oscillation of the coupled system. The governing equations can be easily obtained from (2.15) and (2.16), by setting S_1^+ to zero and letting Q_{o1} and Q_{o2} approach infinity, we get:

$$\left(j2\frac{\omega-\omega_o}{\omega_o} \right) A_1 - jk_{12}A_2 = 0 \tag{2.29}$$

$$-jk_{21}A_1 + \left(j2\frac{\omega-\omega_o}{\omega_o} \right) A_2 = 0 \tag{2.30}$$

In order to obtain a nontrivial solution, the determinant of the system of equations is set to zero:

$$\left(2\frac{\omega-\omega_o}{\omega_o} \right)^2 = k_{12}{}^2 \tag{2.31}$$

where k_{12} =k_{21} has been used. This yields two solutions, ω_1 and ω_2 , corresponding to the two natural modes of oscillation. ω_1 and ω_2 satisfy:

$$\left(2\frac{\omega_1-\omega_o}{\omega_o}\right)=-k_{12} \quad ; \quad \left(2\frac{\omega_2-\omega_o}{\omega_o}\right)=k_{12} \tag{2.32}$$

Using (2.32), k_{12} is given by:

$$k_{12}=\frac{\omega_2-\omega_1}{\omega_o} \tag{2.33}$$

This shows that coupling forces the two modes, both originally resonant at ω_o , to split into two new modes at ω_1 and ω_2. The degree of frequency splitting increases with higher coupling.

In order to find the frequencies ω_1 and ω_2, the two coupled resonators can be weakly excited using a two port setup similar to the one shown in Fig. 2.2. Enhanced energy transmission between the two ports is observed at ω_1 and ω_2 as shown in Fig. 2.3. Simulated S_{21} responses of coupled resonators can therefore be used to determine k_{ij} with the aid of equation (2.33).

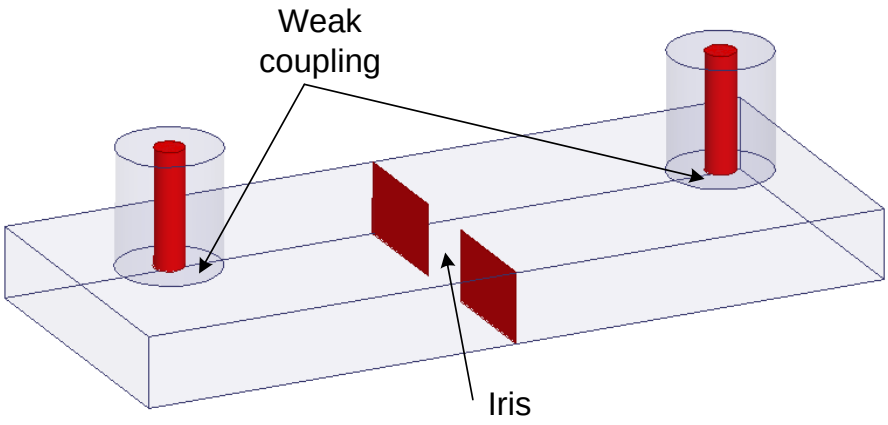

Figure 2.2: Simulation setup of weakly excited coupled resonators to extract k_{ij}.

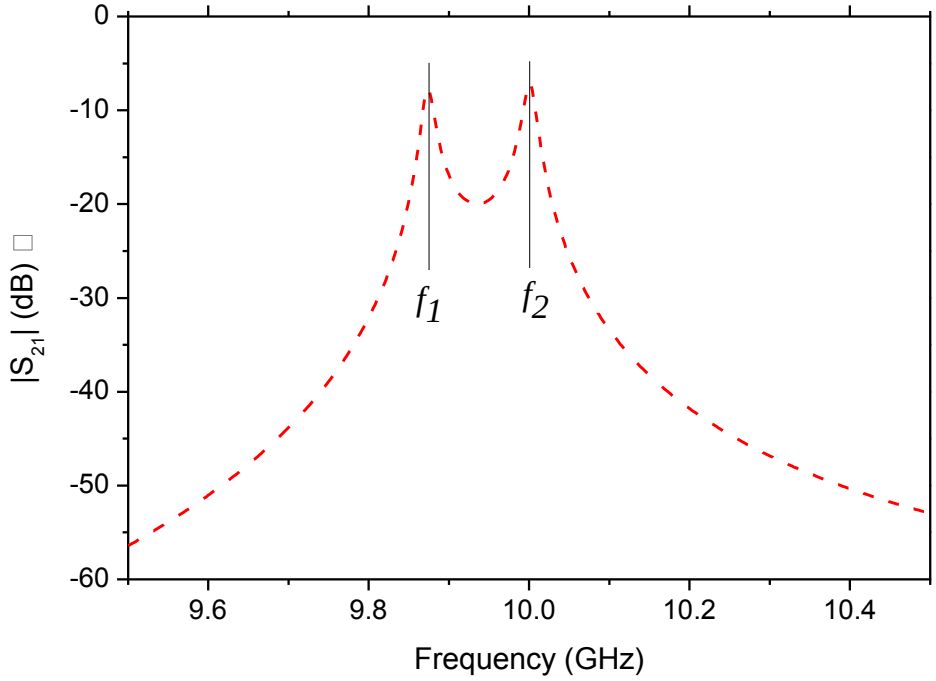

Figure 2.3: Simulated S_{21} of the setup in Figure 2.2 used to extract k_{ij}.

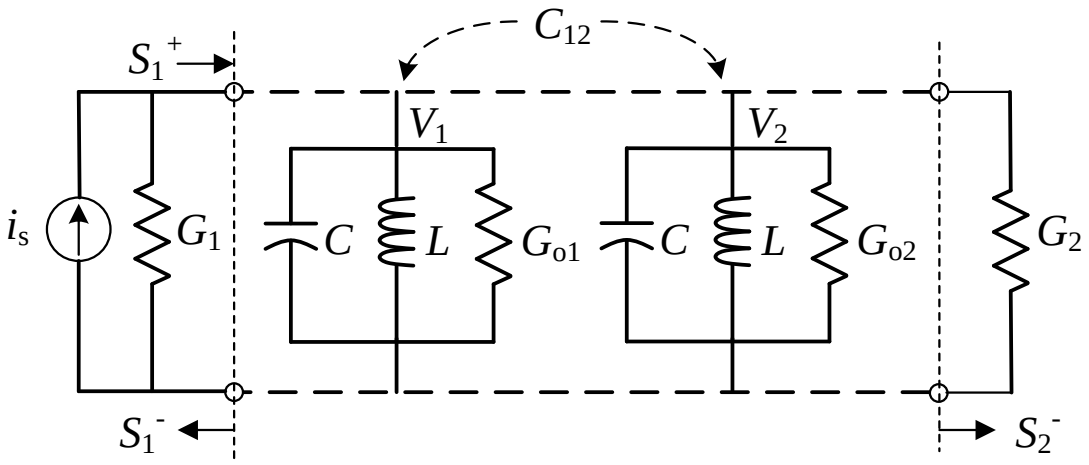

Figure 2.4: Equivalent circuit of a two-pole filter.

2.3.2 Comparison to Coupling Matrix Formulation

It is instructive to compare the coupled-mode formalism to the more commonly used coupling matrix methods. For this purpose, the two-pole filter is analyzed using an approach that closely follows that in [18]. The equivalent circuit of a two-pole filter composed of two shunt *RLC* resonators that are electrically coupled through the mutual capacitance C_{12} is shown in Fig. 2.4. The source excitation is represented by its Norton equivalent circuit consisting of the current source i_s and the source conductance G_1. The conductances G_{o1} and G_{o2} account for the unloaded Q factors of the resonators. The equivalent circuit is analyzed by first writing the nodal equations as:

$$\left(G_1 + G_{o1} + j\omega C + \frac{1}{j\omega L}\right)V_1 - j\omega C_{12}\cdot V_2 = i_s \tag{2.34}$$

$$-j\omega C_{21}\cdot V_1 + \left(G_2 + G_{o2} + j\omega C + \frac{1}{j\omega L}\right)V_2 = 0 \tag{2.35}$$

Equations (2.34) and (2.35), can be written as:

$$\left(j\left(\frac{\omega}{\omega_o} - \frac{\omega_o}{\omega} \right) + \frac{1}{Q_{ext,1}} + \frac{1}{Q_{o1}} \right) V_1 - jk_{12} \cdot V_2 = \frac{i_s}{\omega_o C} \tag{2.36}$$

$$- jk_{21} \cdot V_1 + \left(j\left(\frac{\omega}{\omega_o} - \frac{\omega_o}{\omega} \right) + \frac{1}{Q_{ext,2}} + \frac{1}{Q_{o2}} \right) V_2 = 0 \tag{2.37}$$

where the external and unloaded Q factors are:

$$Q_{ext,i} = \frac{\omega_o C}{G_i} \quad ; \quad Q_{oi} = \frac{\omega_o C}{G_{oi}} \tag{2.38}$$

and the coupling coefficients are defined as:

$$k_{ij} = \frac{\omega}{\omega_o} \frac{C_{ij}}{C} \approx \frac{C_{ij}}{C} \tag{2.39}$$

where the last form of (2.39) follows from the narrowband approximation, $\omega / \omega_o \approx 1$. The source excitation in Fig. 2.4 can be equivalently represented with the incident wave s_1^+, where $|s_1^+|^2$ is the incident power. In terms of i_s, s_1^+ and s_1^- are given by [18]:

$$S_1^+ = \frac{i_s}{2\sqrt{2 \cdot G_1}} \quad ; \quad S_1^- = \frac{2V_1 G_1 - i_s}{2\sqrt{2 \cdot G_1}} \tag{2.40}$$

and for the second port,

$$S_2^+ = 0 \quad ; \quad S_2^- = V_2 \sqrt{G_2 / 2} \tag{2.41}$$

In order to show the similarity between coupled-mode and the coupling matrix approaches, we now find the relation between the mode amplitudes A_i and the corresponding node voltages V_i. For this purpose, we note that the total energy stored in the shunt *LC* resonator *i* at resonance, $|A_i|^2$, is given by:

$$|A_i|^2 = \frac{1}{2} C |V_i|^2 \tag{2.42}$$

Using (2.42), we infer the relation:

$$A_i = \sqrt{\frac{C}{2}} V_i \tag{2.43}$$

Using (2.43) and (2.40) in (2.36), and (2.37), we have:

$$\left(j\left(\frac{\omega}{\omega_o} - \frac{\omega_o}{\omega} \right) + \frac{1}{Q_{ext,1}} + \frac{1}{Q_{o1}} \right) A_1 - jk_{12} A_2 = \frac{2}{\sqrt{\omega_o Q_{ext,1}}} S_1^+ \tag{2.44}$$

$$-jk_{21} A_1 + \left(j\left(\frac{\omega}{\omega_o} - \frac{\omega_o}{\omega} \right) + \frac{1}{Q_{ext,2}} + \frac{1}{Q_{o2}} \right) A_2 = 0 \tag{2.45}$$

By also substituting (2.43) into (2.40) and (2.41) and using (2.38), (2.40) and (2.41) are found to be identical to (2.19). By comparing (2.32) and (2.33) with (2.15), and (2.16), we find that the two forms are identical apart from the frequency variables, p_1 and p_2 given by:

$$p_1 = 2\frac{\omega - \omega_o}{\omega_o} \quad ; \quad p_2 = \frac{\omega}{\omega_o} - \frac{\omega_o}{\omega} \tag{2.46}$$

For $\omega \approx \omega_o$, p_1 and p_2 are approximately equal and are related using a Taylor expansion given by:

$$p_2 = p_1\left(1 - \frac{1}{4} p_1 + \frac{1}{8} p_1^2 - \frac{1}{16} p_1^3 + ... \right) \tag{2.47}$$

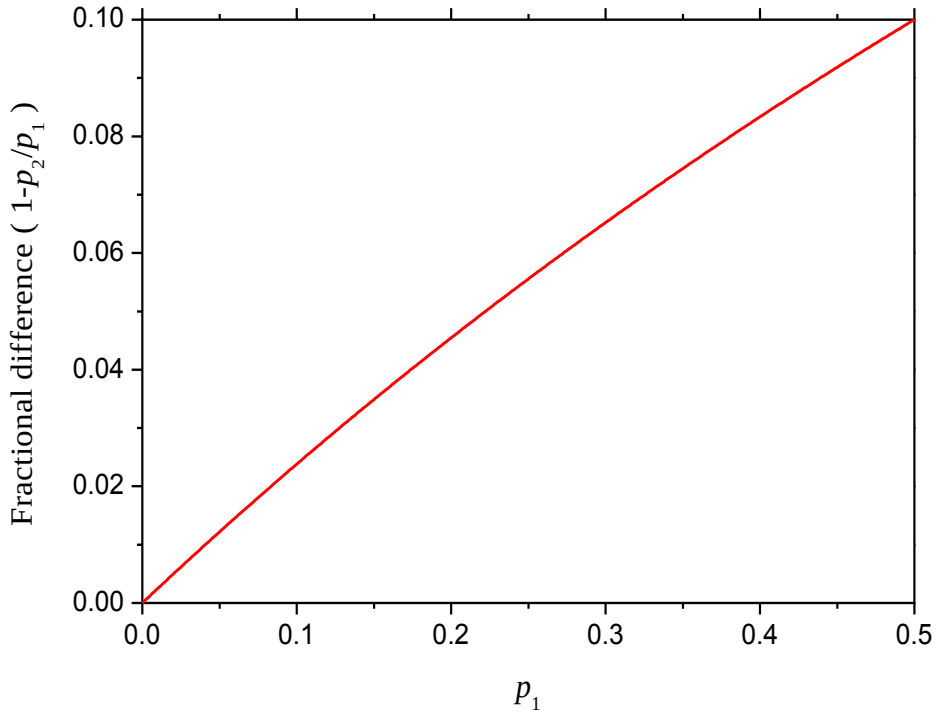

Figure 2.5: Fractional difference between the two frequency variables p_1 and p_2.

Fig. 2.5 shows the fractional difference between the two frequency variables calculated using (2.35). It is seen that the two frequency variables differ by less than 10% for frequency ranges of 50% fractional bandwidths. The S-parameters of a 10% two-pole filter centered at 10 GHz is plotted in Fig. 2.6 using both frequency variables for comparison.

2.3.3 Application to Filter Insertion Loss

The presented coupled-mode analysis can be used to determine the insertion loss of a filter with the knowledge of the external Q factors $Q_{ext,i}$, the coupling coefficients k_{ij}, and the unloaded Q factors Q_{oi} of its constituent resonators. There are methods available in the literature to calculate the insertion loss of filters [16]. In addition to being approximate, the insertion loss formulas in [16] are expressed in terms of the low-pass prototype element values g_i of the filter.

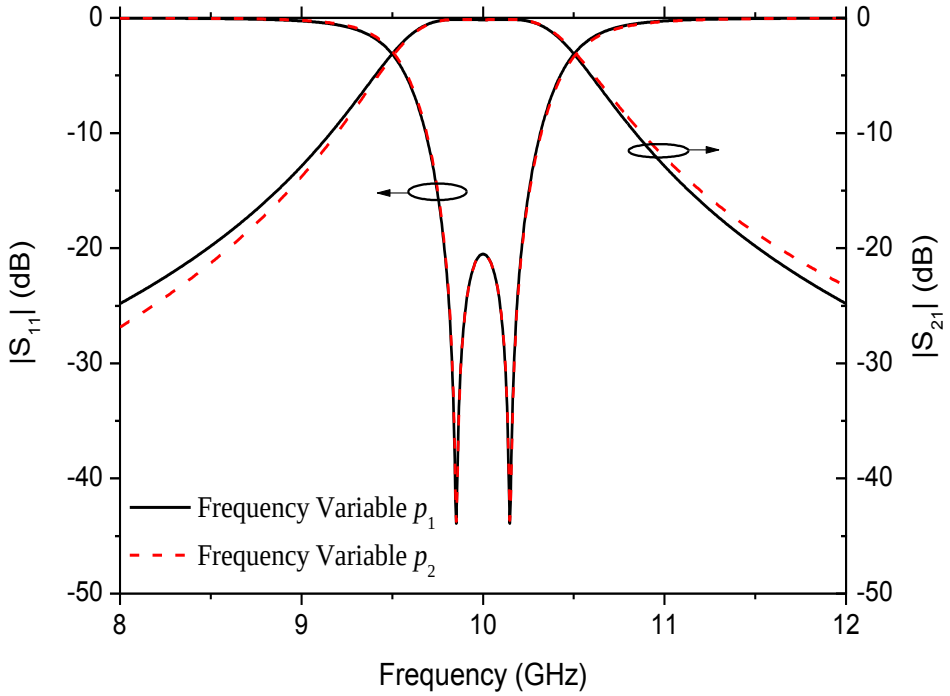

Figure 2.6: S-parameters of a two-pole filter calculated using p_1, and p_2.

Although, $Q_{ext,i}$ and k_{ij} can be used to calculate the prototype element values g_i , insertion loss formulas in terms of the former quantities are more convenient in some cases.

Using (2.21), the insertion loss of a two-pole filter at its center frequency ω_o is given by:

$$IL_{2\,pole} = -10\log\left(\frac{4k_{21}^2/\left(Q_{ext,1}\cdot Q_{ext,2}\right)}{\left(\left[\frac{1}{Q_{ext,1}}+\frac{1}{Q_{o1}}\right]\left[\frac{1}{Q_{ext,2}}+\frac{1}{Q_{o2}}\right]+{k_{21}}^2\right)^2}\right) \tag{2.48}$$

Following the same procedure leading to (2.21), expressions of the insertion loss of three-pole, four-pole, and five-pole filters are obtained and are given by:

$$IL_{3pole} = -10\log\left(\frac{4(k_{12}k_{23})^2/(Q_{ext,1}\cdot Q_{ext,2})}{\left(\left(\frac{1}{Q_{ext,1}}+\frac{1}{Q_{o1}}\right)\left[\frac{1}{Q_{o2}}\left(\frac{1}{Q_{ext,2}}+\frac{1}{Q_{o3}}\right)+k_{23}{}^2\right]+k_{12}{}^2\left(\frac{1}{Q_{ext,2}}+\frac{1}{Q_{o3}}\right)\right)^2}\right) \quad (2.49)$$

$$IL_{4pole} = -10\log\left(\frac{4(k_{12}k_{23}k_{34})^2/(Q_{ext,1}\cdot Q_{ext,2})}{\left(k_{12}^2k_{34}^2+\left(\frac{1}{Q_{ext,2}}+\frac{1}{Q_{o4}}\right)\frac{k_{12}^2}{Q_{o3}}+\left(\frac{1}{Q_{ext,1}}+\frac{1}{Q_{o1}}\right)\frac{k_{34}^2}{Q_{o2}}+\left(\frac{1}{Q_{ext,1}}+\frac{1}{Q_{o1}}\right)\left(\frac{1}{Q_{ext,2}}+\frac{1}{Q_{o4}}\right)\left(\frac{1}{Q_{o2}Q_{o3}}+k_{23}{}^2\right)\right)^2}\right) \quad (2.50)$$

$$IL_{5pole} = -10\log\left(\frac{4(k_{12}k_{23}k_{34}k_{45})^2/(Q_{ext,1}\cdot Q_{ext,2})}{\left(\frac{k_{12}^2k_{45}^2}{Q_{o3}}+k_{12}^2\left(\frac{1}{Q_{ext,2}}+\frac{1}{Q_{o5}}\right)\left(k_{34}^2+\frac{1}{Q_{o3}Q_{o4}}\right)+k_{45}^2\left(\frac{1}{Q_{ext,1}}+\frac{1}{Q_{o1}}\right)\left(k_{23}^2+\frac{1}{Q_{o2}Q_{o3}}\right)+\left(\frac{1}{Q_{ext,1}}+\frac{1}{Q_{o1}}\right)\left(\frac{1}{Q_{ext,2}}+\frac{1}{Q_{o5}}\right)\left(\frac{1}{Q_{o2}Q_{o3}Q_{o4}}+\frac{k_{23}{}^2}{Q_{o4}}+\frac{k_{34}{}^2}{Q_{o2}}\right)\right)^2}\right) \quad (2.51)$$

In order to demonstrate the use of the insertion loss equations (2.36)-(2.39) and compare them with the results of [16], a 10% four-pole 0.2 dB equal ripple Chebyshev filter is designed at 10 GHz starting from a low-pass prototype. The prototype values g_i of filters with different ripple and order are tabulated in [16]. For a four-pole 0.2 dB equal ripple filter, g_i are given by:

$$g_0 = 1;\ g_1 = 1.3028;\ g_2 = 1.2844;\ g_3 = 1.9761;\ g_4 = 0.8468\ ;\ g_5 = 1.5386 \quad (2.52)$$

Using equations (2.22) and (2.23), the design parameters of the filter are found as:

$$Q_{ext,1} = Q_{ext,2} = 13.03;\ \ k_{12} = k_{34} = 0.0773;\ \ k_{23} = 0.0628 \quad (2.53)$$

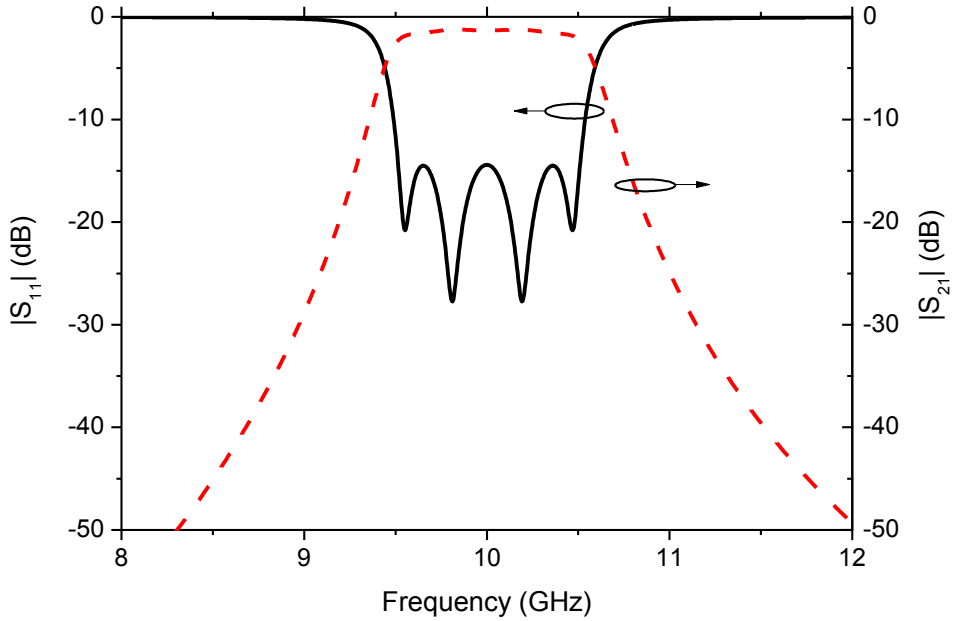

Figure 2.7: S-parameters of a four-pole filter.

Using a circuit simulator the S-parameters of the designed filter are obtained and plotted in Fig. 2.7. The unloaded Q factors Q_{oi} of all four resonators are assumed to have the same value of 200. The insertion loss of a filter of order N in terms of g_i is given by [16]:

$$IL = \frac{4.343}{FBW}\sum_{i=1}^{N}\frac{g_i}{Q_{oi}} \tag{2.54}$$

Using (2.54), the insertion loss of the four-pole filter in Fig. 2.7 is found to be 1.17 dB compared with 1.33 dB as calculated using (2.50). Since the coupled-mode theory results coincide at the center frequency with the coupling matrix results, and because the coupling matrix is derived based on an equivalent circuit model, the coupled-mode approach yields results identical to the circuit simulator.

2.4 Conclusion

In this chapter, we briefly reviewed some of the basic principles needed in designing microwave filters and integrated filter/antenna systems. The review utilized coupled-mode theory, which emphasizes the physics involved in general coupled resonator systems. The theory was compared with the more conventional coupling matrix approach. The two approaches are found to be closely related. Using the coupled-mode theory, the insertion loss of filters was studied and accurate expression for filters up to fifth order were obtained.

3 INTEGRATION OF FILTERS WITH SLOT ANTENNAS

3.1 Introduction

In this chapter, a synthesis technique to integrate high-Q 3-D filters with highly efficient slot antennas is presented. This technique allows for compact integration of 3-D filters and antennas with very high antenna efficiency and significantly reduced form factor of integrated RF front ends. The structure of the proposed filter/antenna system is very compact and easy to fabricate. As shown in Fig. 3.1, the slot antenna does not occupy any additional volume as compared with traditional approaches. The quality of filtering and radiation characteristics is preserved. Moreover, it is found that there is near-zero transition loss between the filter and antenna. Equivalent circuit models are developed for the integrated filter/antenna. This new method can be particularly useful for phased arrays by providing high-Q filtering with small form factors and eliminating either bulky coaxial or lossy transmission line connections between filters and antennas. Therefore, phased arrays with higher sensitivity, less co-site interference, and more robust mechanical structures are possible by using this integration technique.

3.2 Filter Synthesis

First, a four-pole Chebyshev bandpass cavity filter at *X* band as shown in Fig. 3.2 is synthesized. The integrated filter/antenna based on the same filter is shown in Fig. 3.3. A four-pole Chebyshev SIW cavity filter using coaxial feeding is designed at *X* Band. The design parameters of the 6.5% fractional bandwidth four-pole Chebyshev filter are shown as:

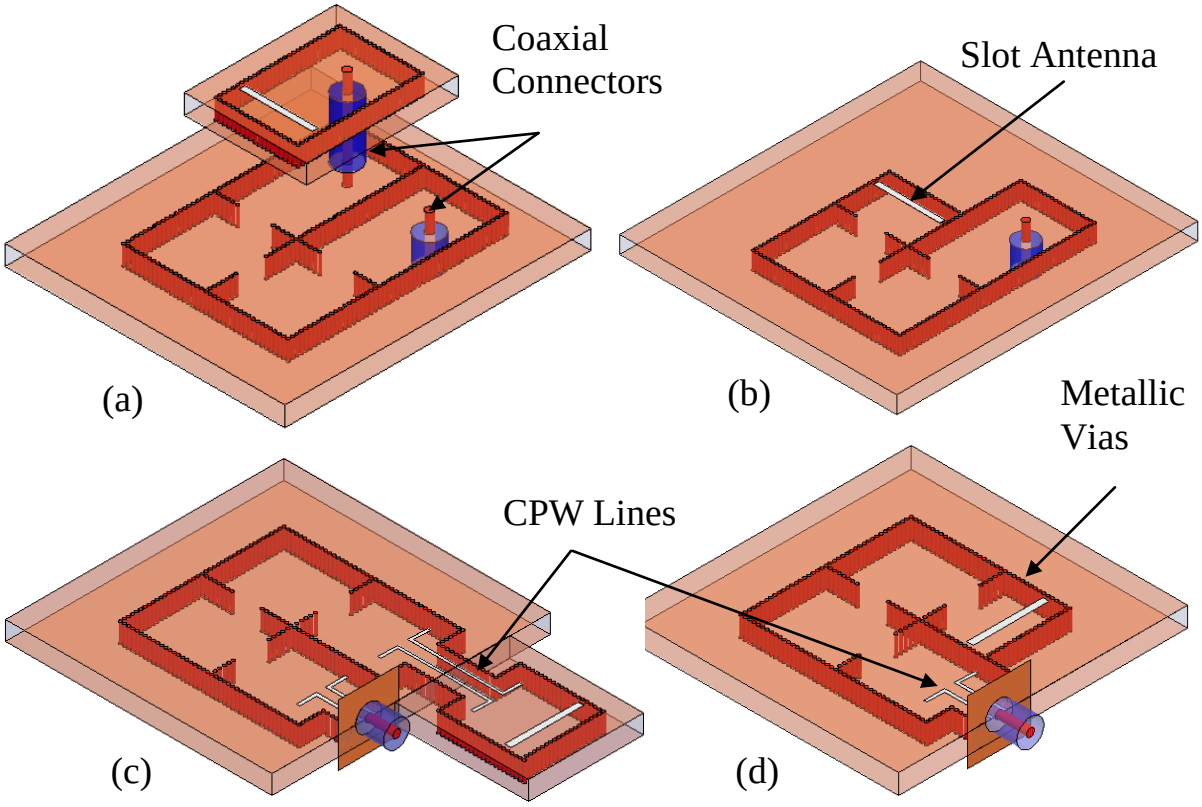

Figure 3.1: Schematics of (a) a coaxial-fed filter connected with a cavity-backed slot antenna using coaxial connectors; (b) a coaxial-fed integrated filter/antenna; (c) a CPW-fed filter connected with a cavity-backed slot antenna using CPW lines; (d) a CPW-fed integrated filter/antenna.

$$k_{12} = k_{34} = 0.046\,;\; k_{23} = 0.037\,;\; Q_{ext} = 20 \tag{3.1}$$

where k_{ij} is the internal coupling coefficient between the ith and jth resonators and Q_{ext} is the external coupling coefficient of the filter.

This filter is built in a 3.17-mm-thick RT/Duroid® 5880 substrate with specified ε_r = 2.2 and $tan\delta$ = 0.0009 from Rogers Corp. The sidewalls of each resonator are formed by closely-spaced metallic vias. The via diameter and spacing are 500 and 700 μm, respectively. The gap between the vias, 200 μm, is much smaller than the wavelength at *X* band. Therefore, the leakage loss through the sidewalls is insignificant compared with the metallic and dielectric losses [6].

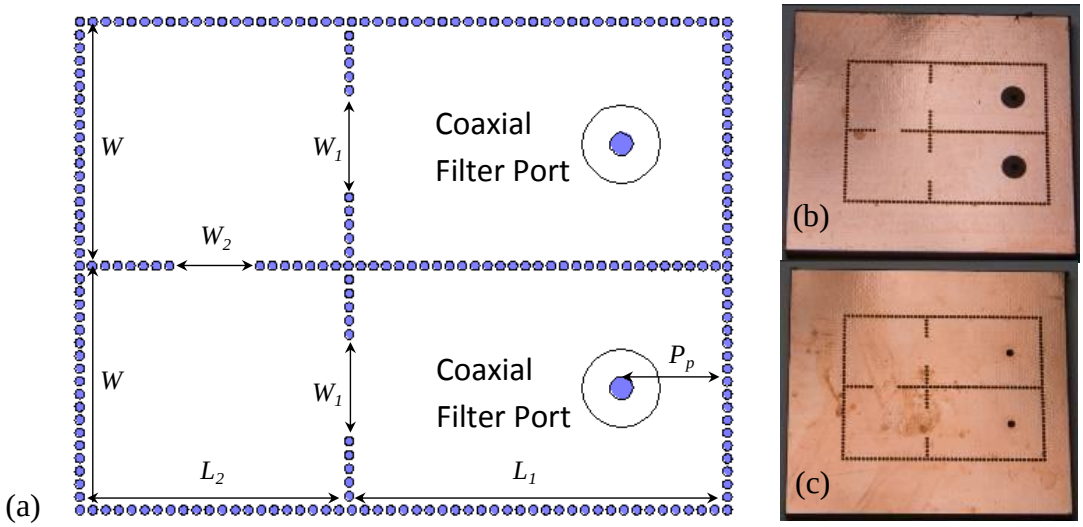

Figure 3.2: (a) Schematic of a filter using coaxial feeding. Picture of the (b) top and (c) back side. (L_1 = 20.4 mm; L_2 = 14.4 mm; W = 13 mm; W_1 = 5.4 mm; W_2 = 4.5 mm; P_p = 5.6 mm)

The inter-resonator coupling is achieved through the irises between the resonators, denoted as W_1 and W_2 in Fig. 3.2(a), representing magnetic coupling. Short-ended coaxial feeding is used here as the external coupling mechanism, which is also magnetic coupling. A via of 1.27 mm in diameter is drilled for the inner conductor of an SMA connector. On the top side of the filter, a circle of 4.32 mm in diameter co-centered with the via is etched to allow the energy coupling between the coaxial connector and cavity. It is noted that the two end resonators, which are located on the right hand side shown in Fig. 3.2(a), have a larger size due to the frequency loading effect from the external coupling. The distance between the center of the coaxial line and end wall of the end resonators, denoted as P_p, is adjusted to achieve the required external coupling. The inner conductor of the SMA connector is soldered on the backside of the filter to form the short-ended connection.

The final dimensions of the filter are listed in Fig. 3.2. The filter responses are simulated using Ansoft High Frequency Structure Simulator (HFSS). The simulated center frequency, bandwidth,

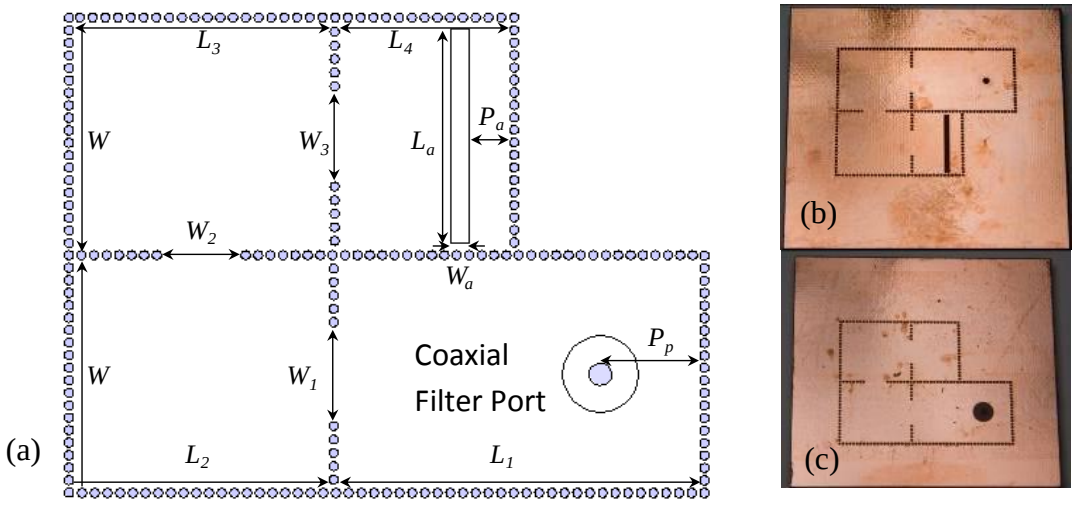

Figure 3.3: (a) Schematic of a filter/antenna using coaxial feeding. Picture of the (b) antenna and (c) coaxial feeding side. (L_1 = 20.4 mm; L_2 = 14.4 mm; L_3 = 14.5 mm; L_4 = 9.6 mm; W = 13 mm; W_1 = 5.4 mm; W_2 = 4.5 mm; W_3 = 5.2 mm; W_a = 1 mm; L_a = 12.2 mm; P_a = 2.3 mm; P_p = 5.6 mm)

and insertion loss are 9.85 GHz, 6.5%, and 0.53 dB, respectively. Return losses higher than 17 dB are achieved within the entire passband. Since this filter is used as a reference of the proposed filter/antenna, the S parameters of the filter will be compared with those of the filter/antenna in Section 3.3.

3.3 Filter/Antenna Synthesis

To realize an integrated filter/antenna, one port of the filter is replaced by a slot antenna. As shown in Fig. 3.3, this slot antenna is etched on the top side of the end resonator. The replacement of one port of the filter by a slot antenna must not change the filtering response. This would require the integrated slot antenna to act as an equivalent port of the filter. Different from a filter, however, energy in the filter/antenna is radiated into space instead of being collected by a second port. To achieve these goals, an antenna with a bandwidth wider than the filter bandwidth has to be chosen. The coupling to the antenna has to be the same as that to the port.

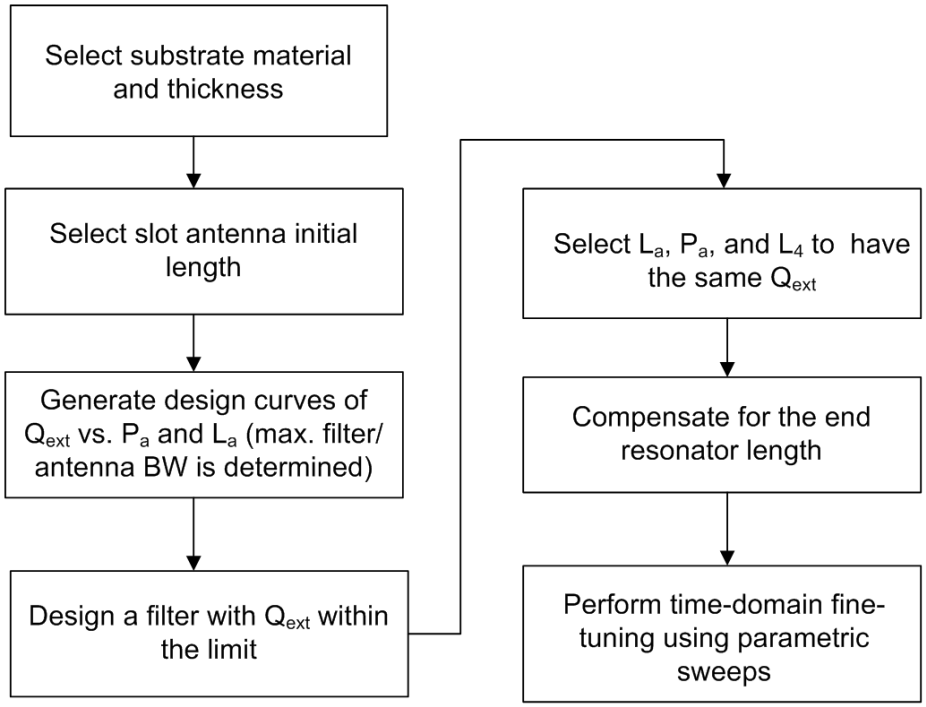

Figure 3.4: Synthesis procedure of filter/antenna.

In other words, the end resonators of both the filter and filter/antenna need to have the same Q_{ext}. In addition, the frequency loading effect from the antenna needs to be taken into account. Provided all these factors are properly considered, the filter/antenna would have the same filtering function as the original filter.

3.3.1 Summary of the Filter/Antenna Synthesis Procedure

A mixed frequency-domain/time-domain synthesis technique is developed herein to achieve near-lossless transition between the filter and antenna and preserve all the desirable functions of the filter and antenna, individually. The filter/antenna synthesis procedure is illustrated in Fig. 3.4. The details of this synthesis technique are presented in Sections 3.3.2-3.3.5. It should be noted that full-wave parametric sweeps are used here to create design curves or fine tune the filter/antenna structure within finite steps. No optimization in full-wave simulators is needed.

3.3.2 Select the Slot Antenna Initial Length

A transverse slot in the broad wall of a waveguide with a width of *W* as shown in Fig. 3.5(a) can be modeled by a series impedance as shown in the equivalent circuit model in Fig. 3.5(b) [24, 25]. Using the approach in [25] but with HFSS simulations, the normalized impedance of the slot is calculated and plotted in Fig. 3.5(c). In this step, the slot length L_a is chosen to achieve an antenna resonant frequency close to the filter center frequency. The slot antenna impedance behavior resembles that of a parallel *RLC* resonator. Therefore, the slot antenna bandwidth in this configuration is found be close to 10% using [26]:

$$\frac{1}{BW} \approx Q = \frac{f(|Z|_{\max})}{\Delta f(|Z|_{\max}/\sqrt{2})} \tag{3.2}$$

3.3.3 Generate Q_{ext} Design Curves and Determine the Antenna Length and Position

The slot antenna inside the end resonator as shown in Fig. 3.6(a) can be modeled by the equivalent circuit shown in Fig. 3.6(b). The reflection coefficients of this structure using HFSS simulations and equivalent circuit models are compared in Fig. 3.6(c) and shown to be very close to each other. It is observed that the phase of S_{11} is 180^o at the center frequency of the filter, 9.85 GHz, when L_4 = 10.7 mm. This structure behaves like a series *RLC* resonator around the center frequency of the filter. To verify this behavior, the input impedance of this structure is simulated and compared with that of a series *RLC* resonator in Fig. 3.7. The element values of the series *RLC* resonator are extracted using:

$$L = \frac{1}{4\pi} \frac{d(\mathrm{Im}(Z_{in}))}{df}\Big|_{f=f_0} \tag{3.3}$$

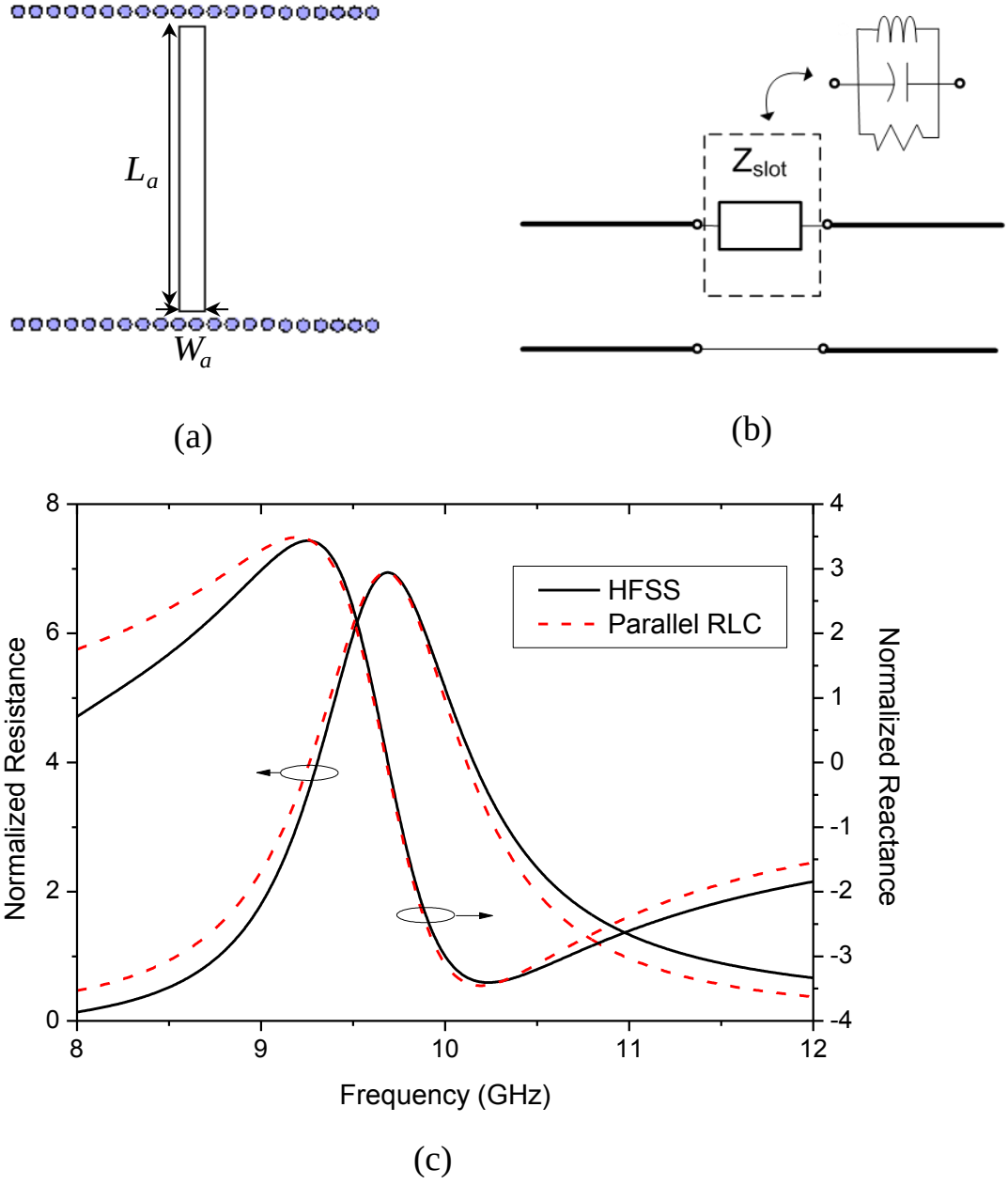

Figure 3.5: (a) Schematic of a transverse slot in a waveguide and (b) its equivalent circuit. (c) Normalized slot impedance for L_a = 12.1 mm and W_a = 1 mm.

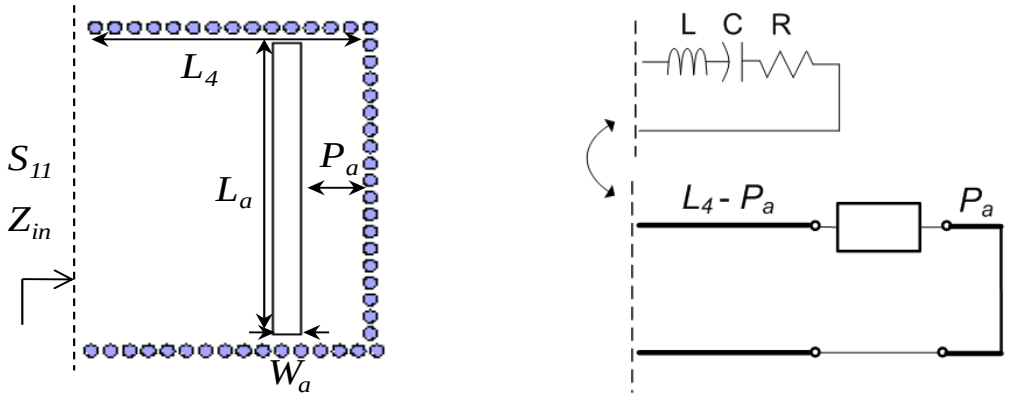

(a) (b)

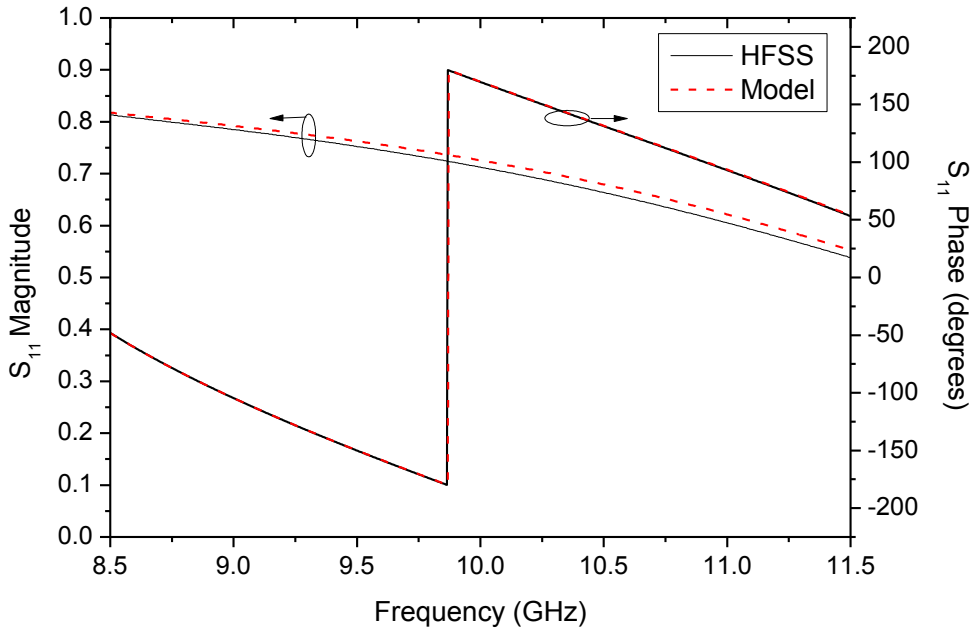

(c)

Figure 3.6: (a) Schematic of a slot antenna in a resonator and (b) its equivalent circuit. (c) Simulated reflection coefficients for a slot antenna inside an end resonator (L_a = 12.1 mm, W_a = 1 mm, P_a = 2.3 mm, L_4 = 10.7 mm).

$$C = \frac{1}{(2\pi f_0)^2 L} \tag{3.4}$$

$$R = Z_{in}(f_0) \tag{3.5}$$

Q_{ext} from the slot antenna can be calculated using:

$$Q_{ext} = \frac{2\pi f_0 L}{R} \tag{3.6}$$

if the resonator is assumed to be lossless in simulations. It is noted from Fig. 3.7 that within the filter bandwidth, which is marked in shaded area, the structure in Fig. 3.6(a) behaves like a series resonator.

The coupling between the slot antenna and filter, Q_{ext}, is controlled by L_a and P_a. Q_{ext} can be found using equation (3.6) by simulating the structure shown in Fig. 3.6(a). It should be noted that the resonator is set to lossless and L_4 is adjusted to achieve S_{11} phase of 180^o at 9.85 GHz for each combination of L_a and P_a. This L_4 adjustment can be done by simply de-embedding the waveguide port in simulations.

The design chart for Q_{ext} is illustrated in Fig. 3.8. It is noted that there are many different combinations of the two parameters to achieve the same Q_{ext}. This is due to the fact that the slot antenna has a wider bandwidth than the filter. Therefore a slightly different L_a can still cover the filter bandwidth. From the design chart, L_a and P_a are selected to be 12.1 and 2.3 mm, respectively, to realize a Q_{ext} of 20. The value of L_4 needed to achieve resonance at 9.85 GHz is found to be 10.7 mm.

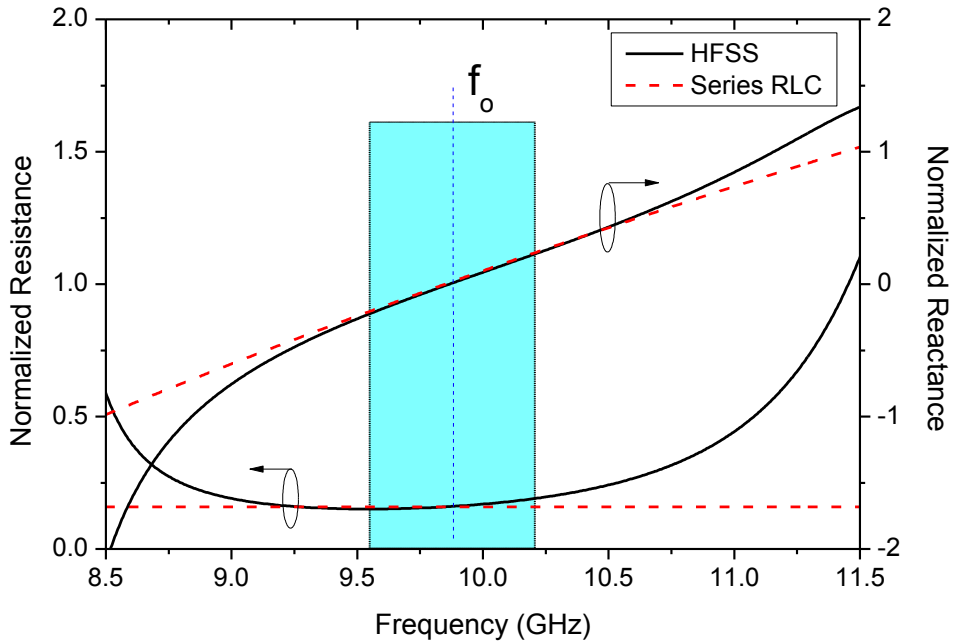

Figure 3.7: The input impedance of the structure in Fig. 3.6(a).

The achievable Q_{ext} range is found to be between 12 and 130, which approximately corresponds to a filter/antenna bandwidth range of 0.8% to 8%.

3.3.4 Compensate for the End Resonator Length

When the designed antenna inside a resonator as shown in Fig. 3.6(a) is incorporated in the filter/antenna structure, the length L_4 needs to be adjusted to account for the frequency loading effect caused by the coupling to the preceding resonator. Fig. 3.9 shows the equivalent circuit of a *K* inverter that uses an iris as well as two transmission lines of electrical length of Φ/2 on both sides of the iris. The length Φ/2 can be calculated using [17]:

$$\Phi = -\tan^{-1}\left(\frac{2X_p}{Z_0} + \frac{X_s}{Z_0}\right) - \tan^{-1}\left(\frac{X_s}{Z_0}\right) \tag{3.7}$$

For our particular design, the required length correction is found to be 1 mm and therefore the length L_4 is adjusted to 9.7 mm accordingly.

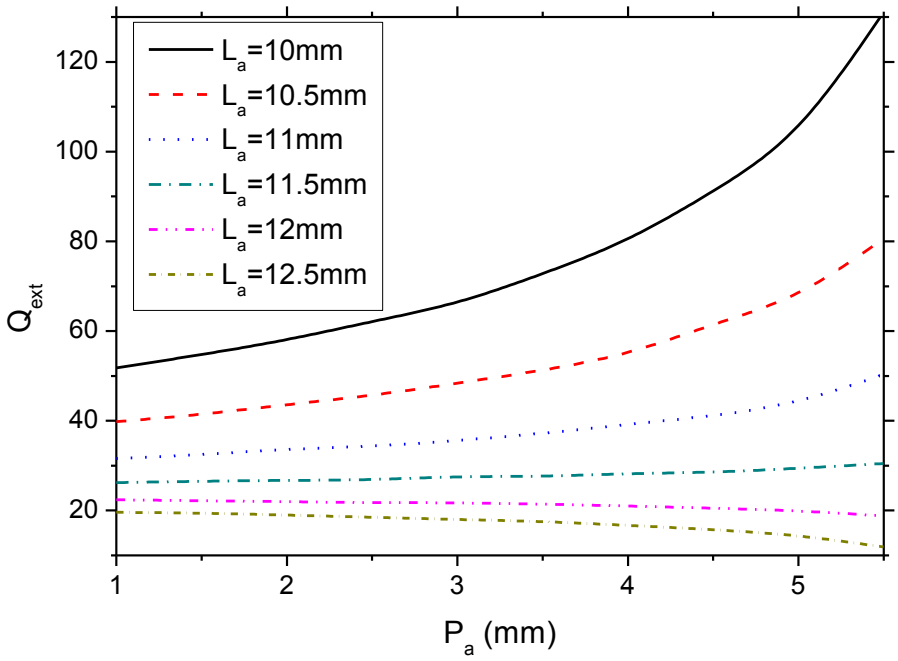

Figure 3.8: Extracted Q_{ext} versus slot antenna position P_a for slot antenna length L_a =10, 10.5, 11, 11.5, 12, and 12.5 mm.

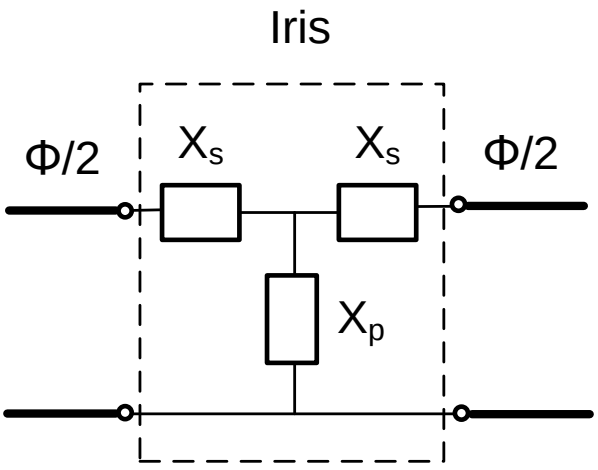

Figure 3.9: The equivalent circuit of an impedance inverter that utilizes an iris and transmission lines.

3.3.5 Time-Domain (TD) Synthesis of Filter/Antenna

Using the filter/antenna structure dimensions from the frequency-domain synthesis, the S_{11} of the filter/antenna is shown in Fig. 3.10 and noticeably different from the filter S_{11}. Optimizing the filter structure in frequency domain is time-consuming.

In order to complete filter/antenna synthesis, a time-domain filter tuning technique [27] is applied here using a software program developed in ARMI lab at UCF. This time-domain technique is able to fine-tune the filter response with just a few parametric sweeps. Using an inverse Chirp-Z transform, the filter S_{11} response is plotted in the time domain as shown in Fig. 3.11. It is observed that the filter responses from different sections of the filter are isolated in the time-domain. The peaks in the time-domain response correspond to the external coupling at Port 1, the internal coupling between resonators 1 and 2 (k_{12}), k_{23}, k_{34}, and the external coupling at Port 2, respectively, from left to right. The dips correspond to the resonators 1 through 4, respectively. A rise (sink) of the level of the peaks means smaller (larger) coupling. While the rise of the dips from their minimum values means off-tuned resonances. The filter/antenna S_{11} time-domain response can be tuned to match that of the equivalent filter, one by one from left to right, with a few parametric sweeps. L_3 is adjusted to 14.5 mm to match the dip of Resonator 3; W_3 is adjusted to 5.2 mm to match k_{34}; L_4 is fine-tuned to 9.6 mm to the match the dip of Resonator 4; and L_a is fine-tuned to 12.2 to match $Q_{ext,\,2}$. The S_{11} responses of the filter/antenna system in time domain are illustrated in Fig. 3.11. Before the time-domain fine tuning, discrepancies between the filter and filter/antenna are observed. After the time-domain fine tuning, excellent agreement between the two cases is apparent. As a result, the frequency-domain responses of the two cases match closely as shown in Fig. 3.10.

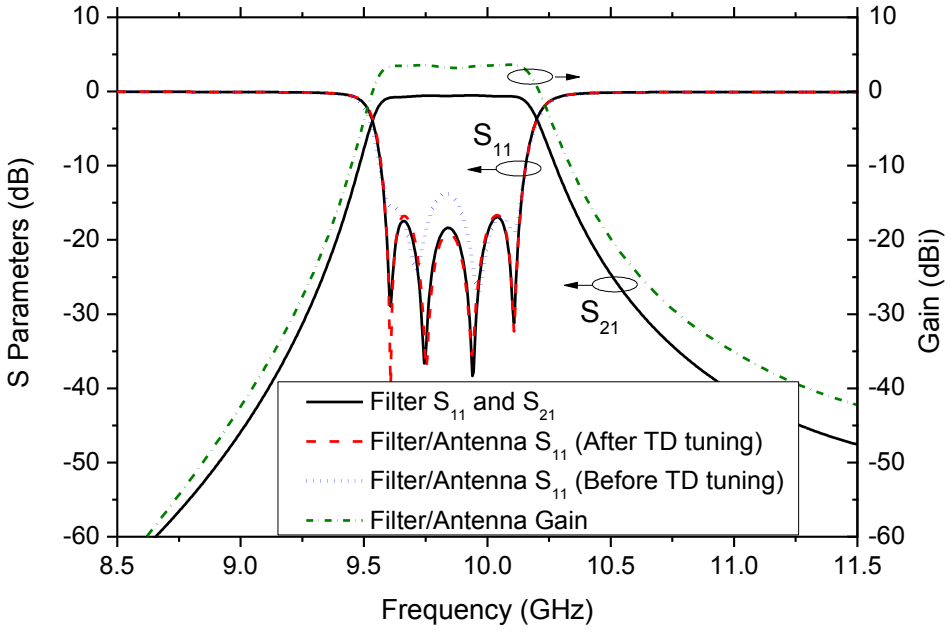

Figure 3.10: Simulated S_{11} and S_{21} of the filter shown in Fig. 3.2. Simulated S_{11} and gain (at boresight) of the filter/antenna shown in Fig. 3.3.

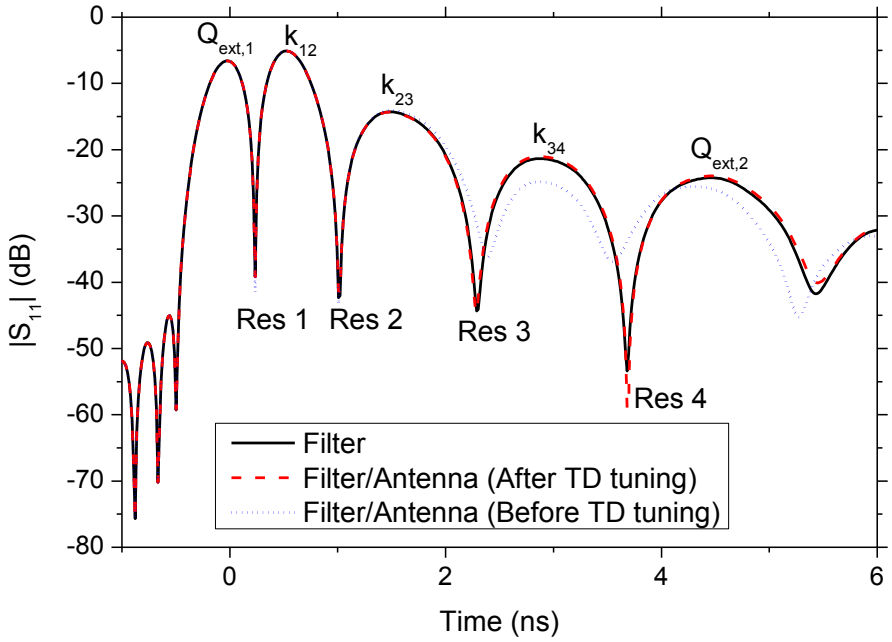

Figure 3.11: Simulated time-domain responses of the filter and filter/antenna.

The gain of the filter/antenna system at the boresight is also shown in Fig. 3.10. It is found that the filter/antenna system exhibits the same filtering function, which is also observed in other radiation directions.

3.3.6 Equivalent Circuit Model of the Filter/Antenna

Equivalent circuit models of the filter as shown in Fig. 3.2 and filter/antenna as shown in Fig. 3.3 are developed and illustrated in Fig. 3.12. The values of the lumped elements are found using equation (3.3)-(3.5). It is noted that though both resonant frequency and Q_{ext} of the last resonator of the filter/antenna are the same as those of the last resonator of the filter, the slope parameter of these two resonators are slightly different. This results in a reflection coefficient difference from the filter S_{11} as shown in Fig. 3.13. This phenomenon is also identified in Fig. 3.10 using full-wave simulations. Using the formula [16]:

$$k_{ij} = \frac{K_{ij}}{2\pi f_0 \sqrt{L_i L_j}} \tag{3.8}$$

it is found that the difference between L_1 and L_1'causes the internal coupling coefficient between the 3rd and 4th resonator to change though K_{34} is still the same. Therefore, K_{34} needs to be adjusted to account for this inductance change. In Fig. 3.13, the filter/antenna with K_{34} = 8.10 Ω restores the filter S_{11} shape. However, this fine tuning of coupling coefficient in full-wave simulators is not as effective since the change of iris dimensions also slightly detunes the resonant frequencies of the 3rd and 4th resonator. Therefore, time-domain tuning as presented in Section 3.3.5 is still necessary.

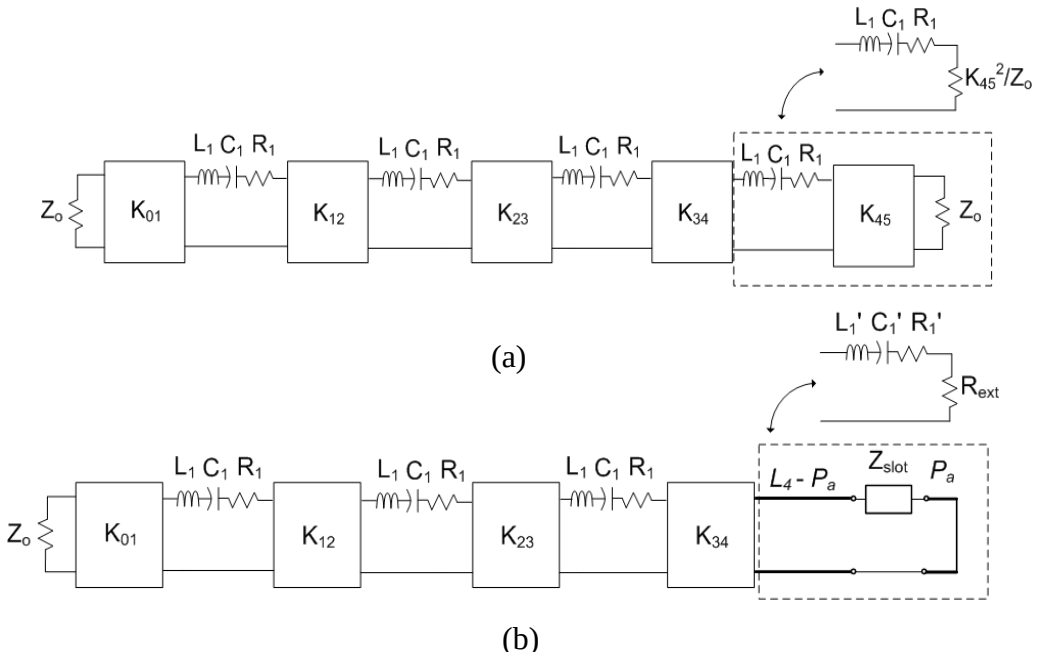

Figure 3.12: Equivalent circuit models of (a) the filter in Fig. 3.2 and (b) filter/antenna in Fig. 3.3. (Z_0 = 50 Ω; K_{01} = K_{45} = 21.9 Ω; K_{12} = K_{34} = 8.75 Ω; K_{23} = 7.05 Ω; L_1 = 3.11 nH; C_1 = 0.0838 pF; R_1 = 0.226 Ω; L_1' = 2.66 nH; C_1' = 0.0978 pF; R_1' = 0.194 Ω; R_{ext} = 8.25 Ω.

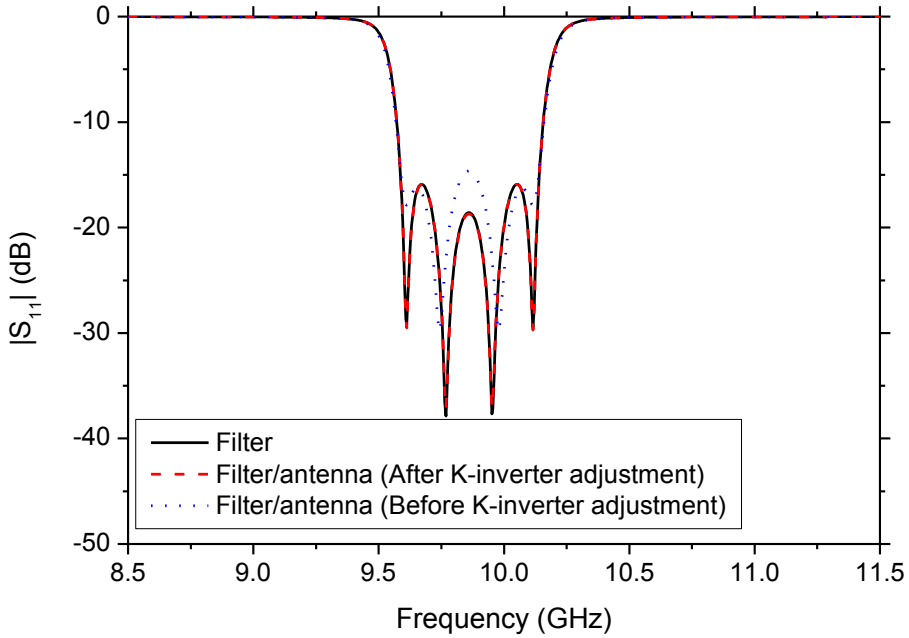

Figure 3.13: S Parameters of the filter and filter/antenna using equivalent circuit.

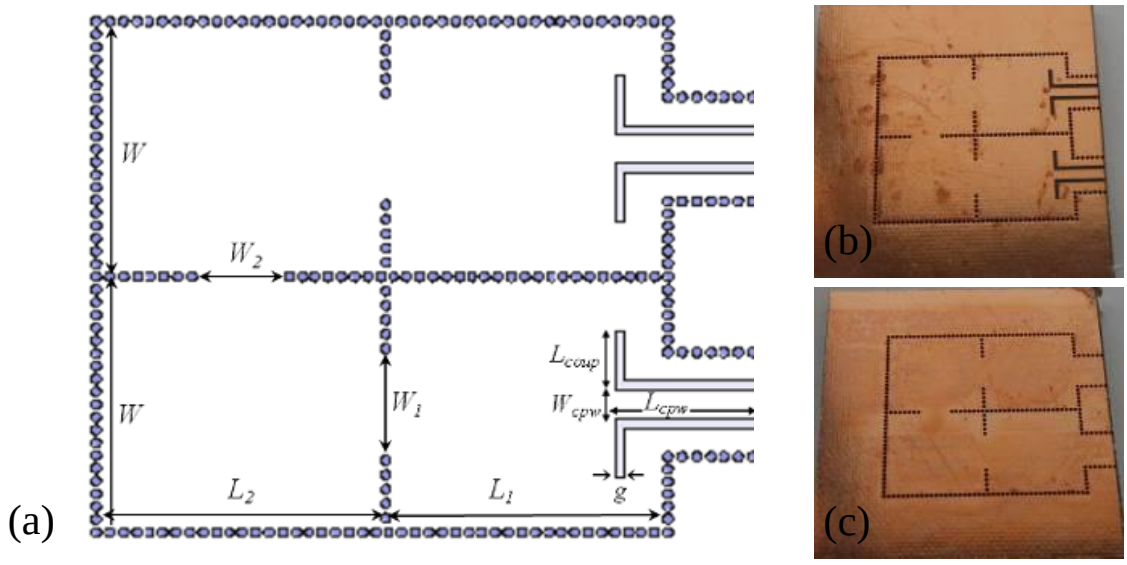

Figure 3.14: (a) Schematic of the filter using CPW feeding. Picture of the (b) top and (c) back side. (L_1 = 14.0 mm; L_2 = 14.4 mm; W = 13 mm; W_1 = 5.4 mm; W_2 = 4.5 mm; L_{cpw} = 7.4 mm; L_{coup} = 3.4 mm; W_{cpw} = 1.5 mm; g = 0.5 mm)

3.3.7 Filter and Filter/Antenna Using CPW Feeding

Although coaxial feeding reduces undesirable losses in the external coupling minimizing the insertion loss of filters, CPW feeding is still preferred when dense packaging is needed. The filter and filter/antenna using CPW feeding are illustrated in Fig. 3.14 and Fig. 3.15, respectively. The dimensions of both devices are designed using the same synthesis approach.

As shown in Fig. 3.16, the simulated center frequency and bandwidth of the filter with CPW feeding are 9.85 GHz and 6.8%, respectively. Return losses higher than 15.5 dB are achieved within the entire passband. The insertion loss of the filter with CPW feeding is 0.87 dB compared with 0.53 dB for the filter with coaxial feeding. This 0.34 dB difference is believed to be from the conductor, dielectric, and radiation losses within the CPW feeding.

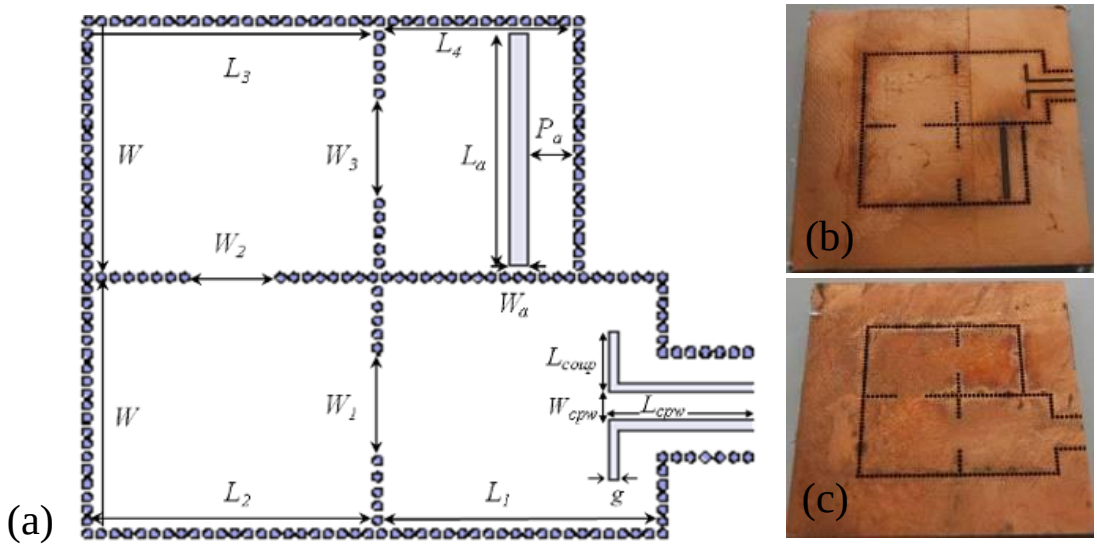

Figure 3.15: (a) Schematic of the filter/antenna using CPW feeding. Picture of the (b) antenna and (c) back side. (L_1 = 14.0 mm; L_2 = 14.4 mm; L_3 = 14.5 mm; L_4 = 9.8 mm; W = 13 mm; W_1 = 5.4 mm; W_2 = 4.5 mm; W_3 = 5.3 mm; L_{cpw} = 7.4 mm; L_{coup} = 3.4 mm; W_{cpw} = 1.5 mm; g = 0.5 mm; W_a = 1 mm; L_a = 12.1 mm; P_a = 2.3 mm)

It is noted that both the S_{21} of the filter and the gain of the filter/antenna do not roll off as sharply as the coaxial feeding cases. For the filter with CPW feeding, it is caused by the cross talk between the CPW lines.

While for the filter/antenna with CPW feeding, it is caused by the radiation from the CPW line. To verify this, metallic shielding caps are placed on top of each CPW line. The roll off of the S_{21} of the filter and the gain of the filter/antenna with shielding caps is as sharp as the coaxial feeding cases. Slight detuning effect in the S_{11} response is observed in Fig. 3.17 due to the shielding cap. However, return losses better than 16.5 dB are still achieved within the filter passband. The insertion loss of the filter with CPW feeding and shielding caps is improved to 0.7 dB, which implies 0.17-dB radiation loss and 0.17-dB metal and dielectric loss within the CPW feeding lines.

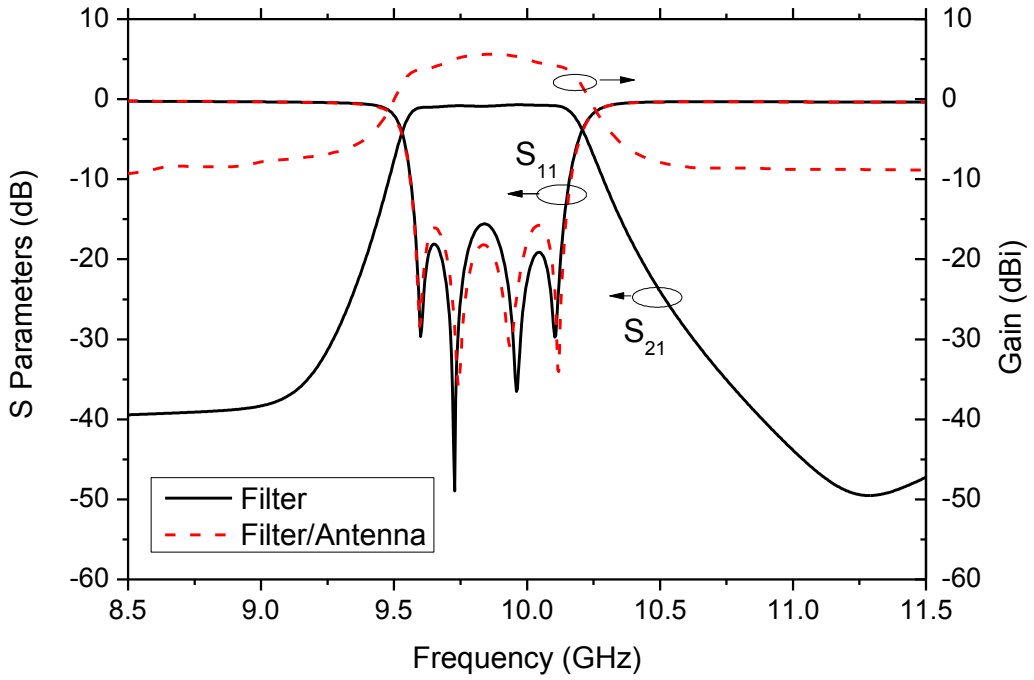

Figure 3.16: Simulated S_{11} and S_{21} of the filter shown in Fig. 3.14. Simulated S_{11} and gain (at boresight) of the filter/antenna shown in Fig. 3.15.

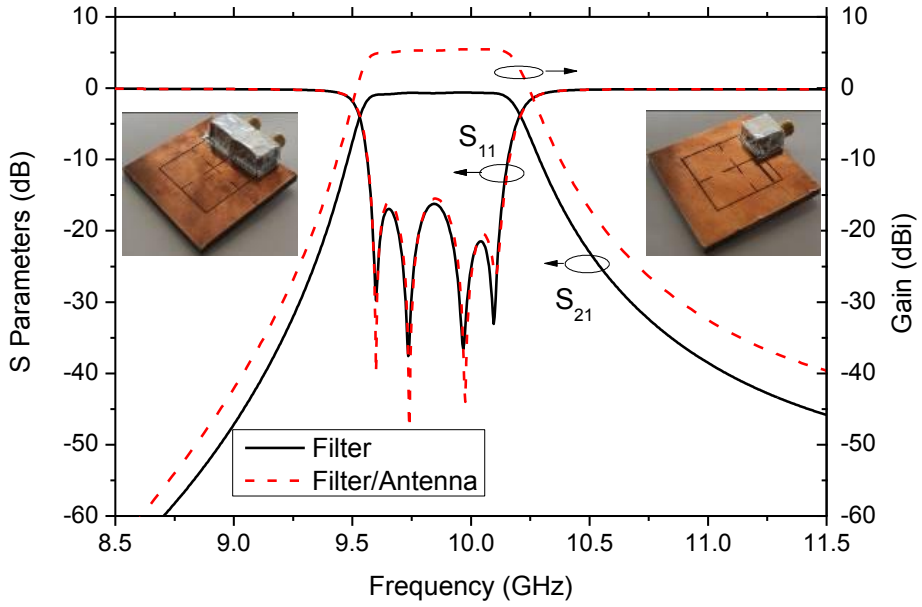

Figure 3.17: Simulated S_{11} and S_{21} of the filter shown in Fig. 3.14 with a shielding cap. Simulated S_{11} and gain (at the boresight) of the filter/antenna shown in Fig. 3.15 with shielding caps.

To summarize, the CPW feeding renders a smaller filter size and is easier for dense packaging. However, there are additional losses within the CPW feeding lines. Proper shielding is also necessary to achieve sharp roll off characteristics.

3.4 Measurement Results and Discussions

Prototype filters and filter/antennas are fabricated and measured. SMA connectors are mounted for both coaxial and CPW feeding cases.

3.4.1 Filter and Filter/Antenna Using Coaxial Feeding

The measured four-pole filter responses are plotted against the simulation results in Fig. 3.18(a). The 1.1% frequency upshift could be due to fabrication tolerances. Nevertheless, this 1.1% frequency upshift is consistently observed in all fabricated devices as shown in Table 1, which means a 1.1% size enlargement can be applied in the 2nd run fabrication to match the design frequency. The measured bandwidth of 6.3% is very close to the simulated bandwidth of 6.5%. Reflection coefficient is less than -13 dB across the entire passband. The measured insertion loss of 0.5 dB is almost identical to the simulated 0.53 dB. This low insertion loss of the filter corresponds to a resonator Q factor around 850 in *X* band.

The measured filter/antenna responses are plotted against the simulation results in Fig. 3.18(b). The measured filter/antenna bandwidth of 6.0% is slightly less than the simulated 6.5%. The matching is better than 15 dB within the passband. The radiation patterns and gain are measured in an anechoic chamber built by TDK Inc. in ARMI Lab. The measured radiation patterns agree very well with the simulation results in both E- and H-planes at the center frequency as shown in Fig. 3.19. Similar radiation patterns are observed across the entire passband.

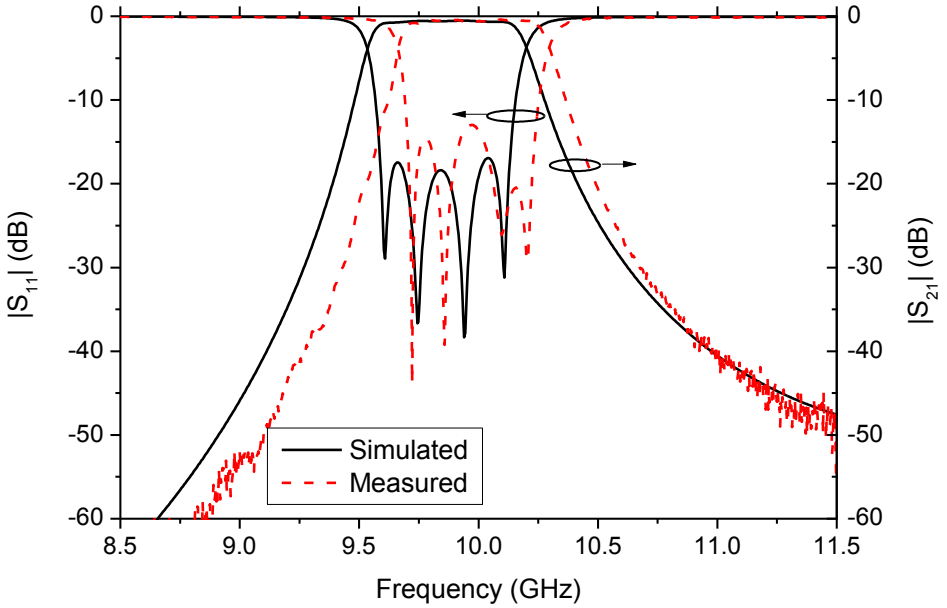

(a)

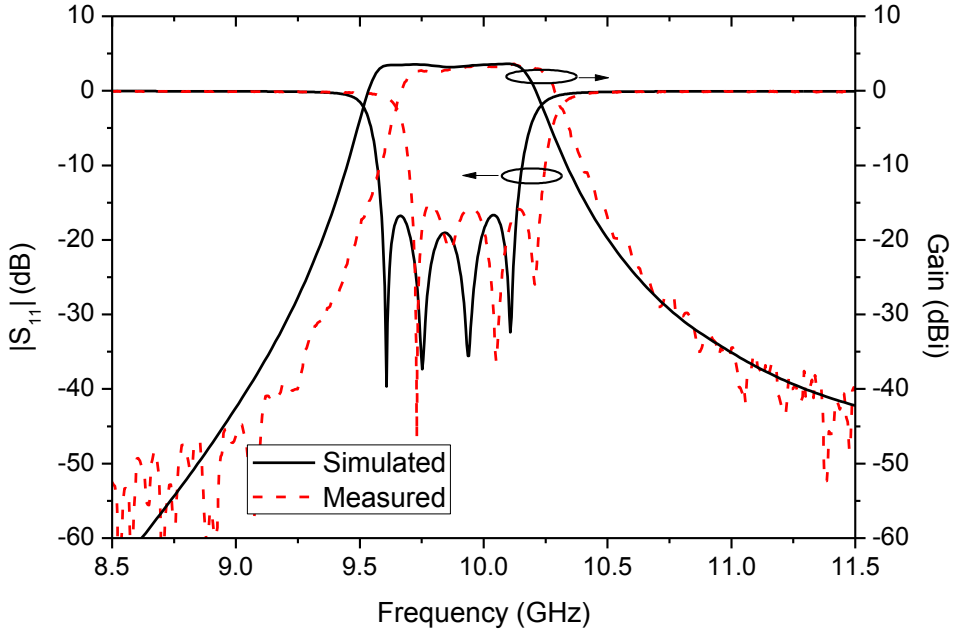

(b)

Figure 3.18: Simulated and measured responses of the (a) filter and (b) filter/antenna using coaxial feeding. The gain is at the boresight.

The measured maximum gain is 6.1 dB. The overall efficiency of the integrated filter/antenna system is calculated by taking the ratio between the gain and simulated directivity and found to be 89%, which is equivalent to a 0.51-dB loss. Compared with the 0.5-dB filter insertion loss, it implies near zero loss from the slot antenna and the transition between the filter and antenna. A near 100% efficient slot antenna is realized using this seamless integration technique. To verify the filtering function of the filter/antenna, gain versus frequency is measured. This measurement is done at the boresight of the slot antenna; therefore a smaller gain is expected due to the dip in the pattern. The wide-band responses of the filter/antenna are shown in Fig. 3.20 between 8.5 and 17 GHz. A spurious mode occurs around 15 GHz, which corresponds to the TE_{102} mode of the cavities.

3.4.2 Filter and Filter/Antenna Using CPW Feeding

The simulation and measurement results for filters and filter/antennas using CPW feeding without and with shielding caps are shown in Fig. 3.21, Fig. 3.22 and Fig. 3.23. The measured bandwidth, impedance matching, filter insertion loss, filter/antenna gain, and radiation pattern closely match simulation results. These results are summarized in Table 1. The measured gain for the filter/antenna without shielding cap is 0.5 dB higher than the simulation. This favorable higher gain is due to the narrower measured radiation pattern as shown in Fig. 3.21(c), which is due to the scattering from the antenna mounting structure, cables, and SMA connectors for an antenna with limited ground plane size.

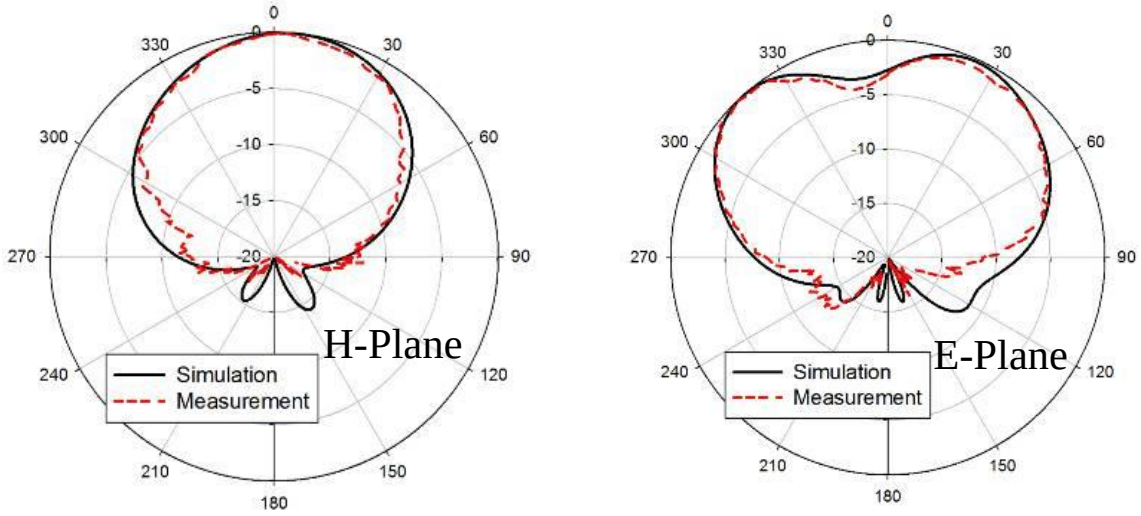

Figure 3.19: Simulated and measured radiation patterns of the filter/antenna using coaxial feeding at f_0.

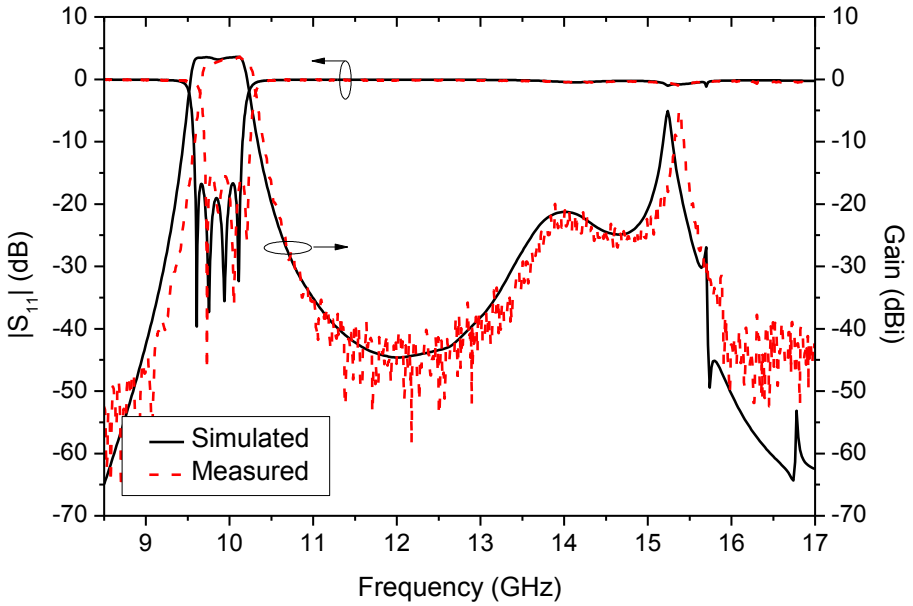

Figure 3.20: Simulated and measured wide-band response of the filter/antenna using coax feeding.

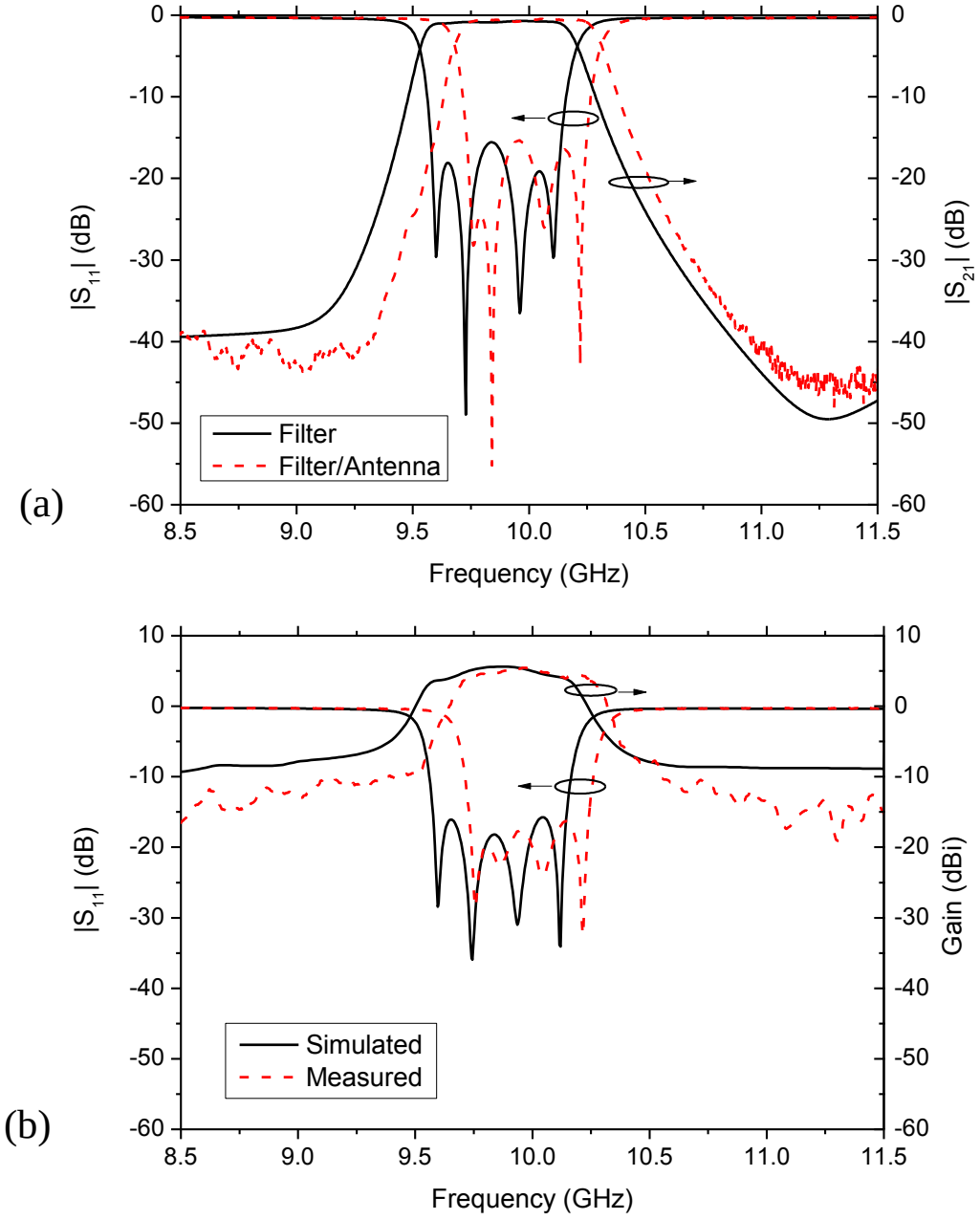

Figure 3.21: Simulated and measured (a) filter responses, and (b) filter/antenna S_{11} and gain at boresight (CPW feeding without shielding cap)

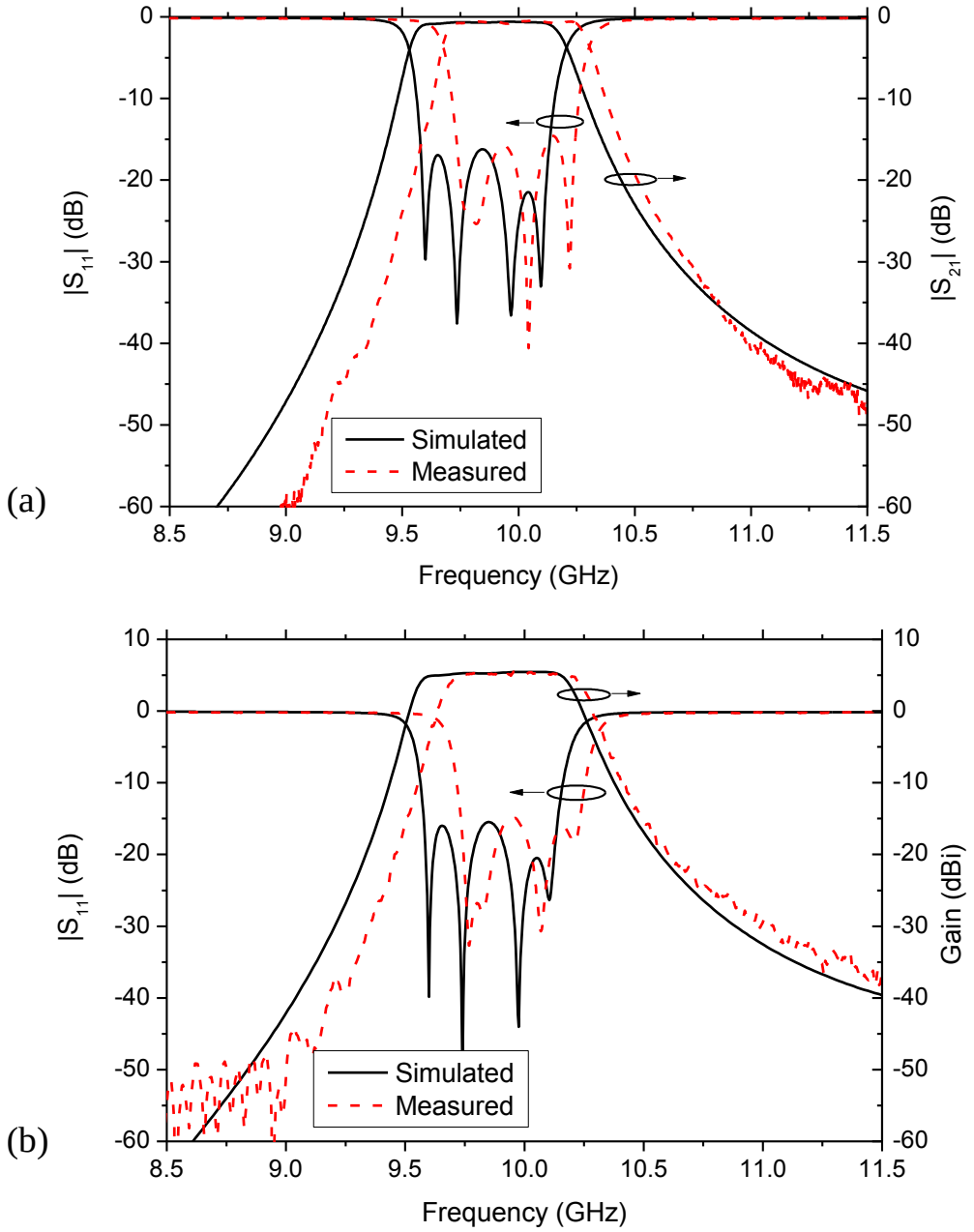

Figure 3.22: Simulated and measured (a) filter responses, and (b) filter/antenna S_{11} and gain at boresight. (CPW feeding with shielding cap)

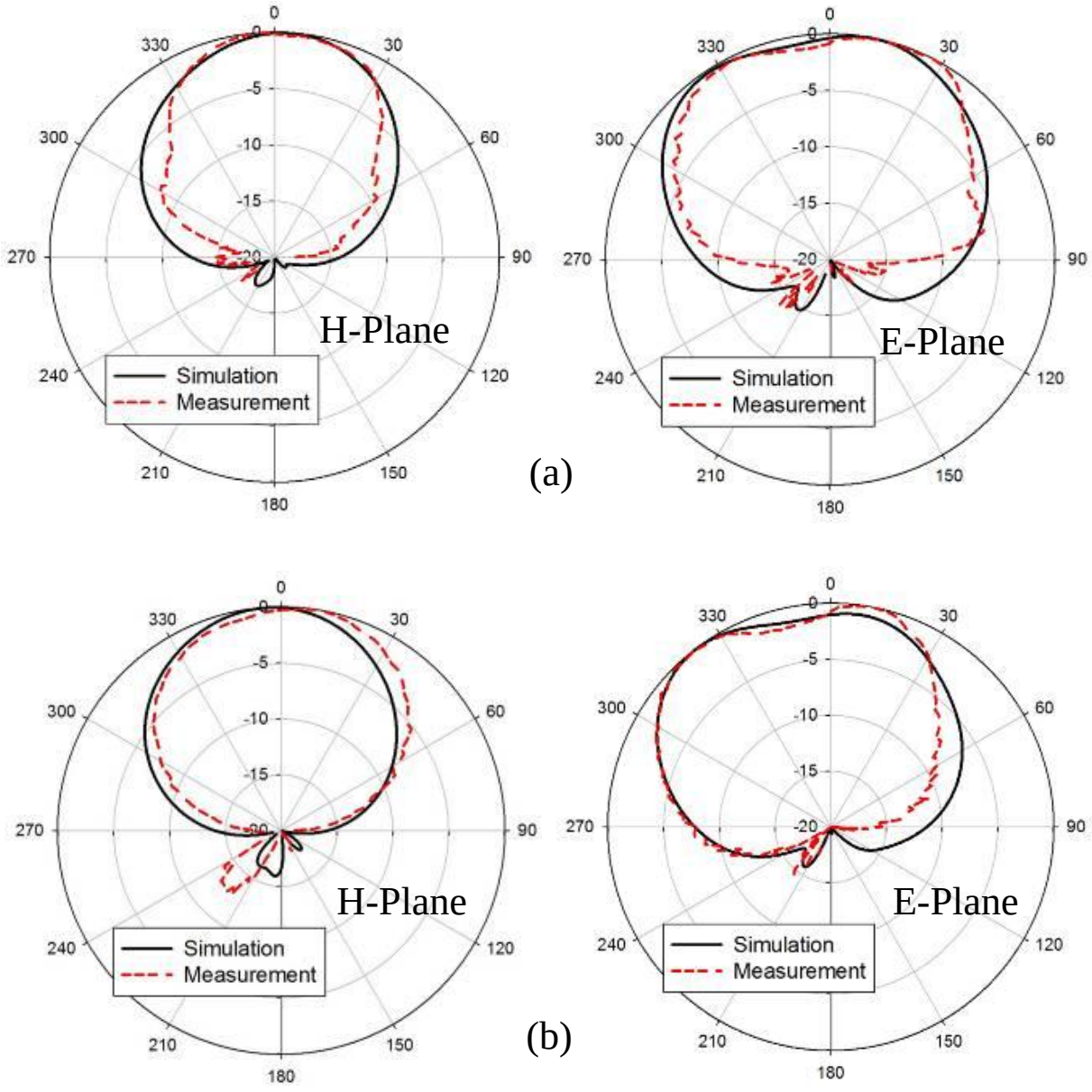

Figure 3.23: CPW fed filter/antenna radiation patterns at f_0. (a) without, and (b) with a shielding cap.

TABLE I

SUMMARY OF RESULTS

Feeding	**Device**	f_0 **(GHz)**		**Bandwidth (%)**		**Max. Gain (dB)**	
		Meas.	Simu.	Meas.	Simu.	Meas.	Simu.
Coaxial	Filter	9.96	9.85	6.3	6.5	-	-
	Filter/Antenna	9.96	9.85	6.0	6.5	6.1	6.1
CPW (No Cap)	Filter	9.96	9.85	6.4	6.8	-	-
	Filter/Antenna	9.96	9.85	6.1	6.8	6.3	5.8
CPW (With Cap)	Filter	9.96	9.85	6.4	6.8	-	-
	Filter/Antenna	9.96	9.85	6.2	6.8	6.3	6.2

3.5 Effect of Different Physical Parameters on Q_{ext}

For the substrate thickness, dielectric constant and cavity width chosen in Section 3, the Q_{ext} of the cavity resonators loaded by the slot antennas was limited to about 10, which corresponds to filter/antenna FBW less than 10%. In this section, the effect of the aforementioned parameters on the achievable Q_{ext} is studied in detail. This study helps designers in selecting the physical parameters in order to achieve the Q_{ext} required by the filter/antenna system to be designed.

Fig. 3.24(a) shows the structure to be analyzed, which may be considered as a limiting case of the resonator/antenna in Fig. 3.6(a), in which the slot is placed at the edge of the cavity and is made long enough to cover the entire cavity width. In addition, we take the slot width to be the same as the substrate height *h*. We now consider the closely related structure in which the slot is moved to the side of the cavity as shown in Fig. 3.24(b), and the dielectric truncated beyond the slot at the edge of the cavity. For the same excitation of the two alternate structures in Fig. 3.24, the waveguide modal voltage drop across the slot antenna, which may be represented as a series impedance in a transmission line, would be the same. For thin substrates, the two structures are also expected to have similar radiation characteristics. Provided that we ignore the effect of higher-order modes associated with the resonator/antenna in Fig. 3.24(b), the two resonator antennas are expected to have very similar Q_{ext}. Being easier to analyze, we therefore study the resonator/antenna structure in Fig. 24(b) using a cavity model often used in the study of microstrip patch antennas [28].

Fig. 3.25 shows a cavity model schematic of the resonator/antenna in which the slot is replaced with a perfect magnetic conductor (PMC) to represent an open circuit. The structure supports the dominant mode illustrated in Fig. 3.25 and is given by:

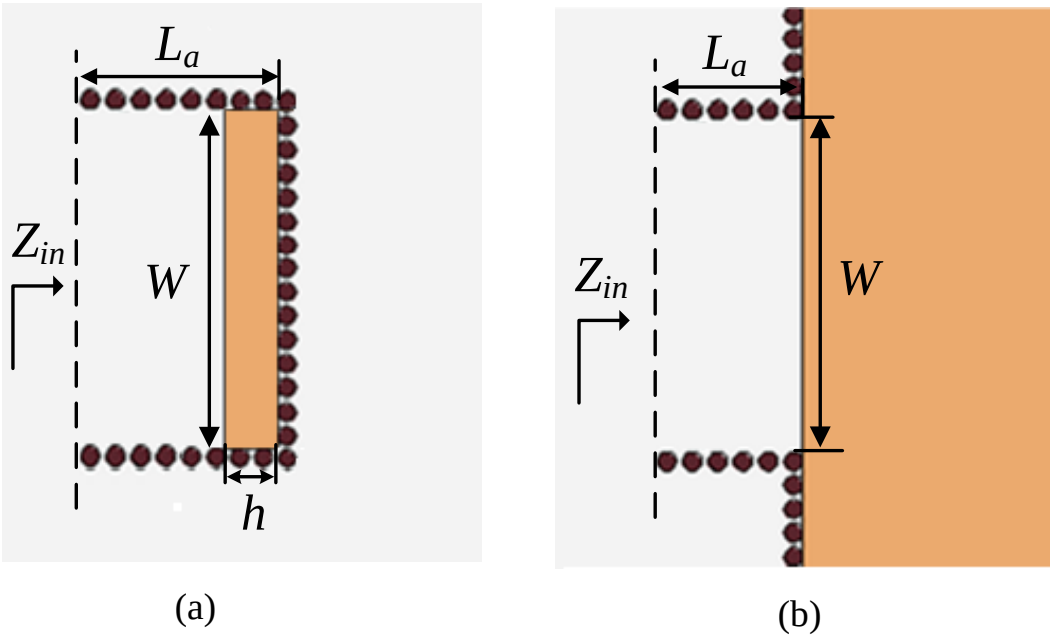

Figure 3.24: Schematic of the resonator/antenna with slot antenna on (a) top and (b) side.

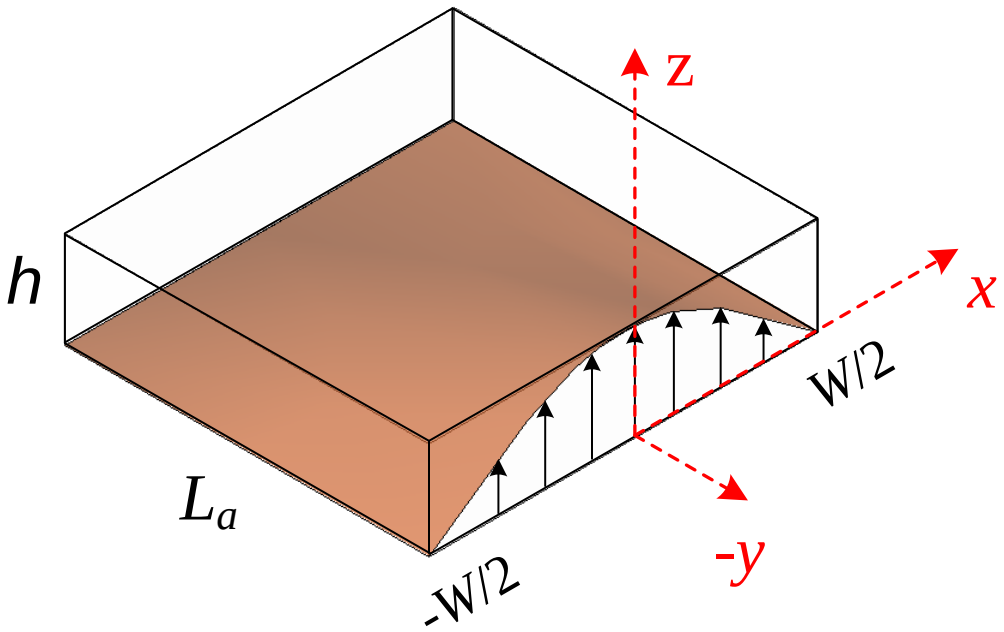

Figure 3.25: Cavity Model schematic of the resonator/antenna.

$$E_z(x,y) = E_o \cos\left(\frac{\pi x}{W}\right)\cos\left(\frac{\pi y}{2L_a}\right) \tag{3.9}$$

This mode exhibits the field distribution of a rectangular metallic cavity of length $2L_a$ operating in its dominant mode in one half of its structure.

By invoking field equivalence principles, the electric field in the slot is replaced with its equivalent surface magnetic current given by:

$$M_x(x) = E_o \cos\left(\frac{\pi x}{W}\right) \tag{3.10}$$

For thin cavities, this surface current can be reduced to a lineal current given by:

$$I_{mx}(x) = E_o h \cos\left(\frac{\pi x}{W}\right) \tag{3.11}$$

By assuming that the cavity is mounted on an infinite ground plane, image theory can be used to double the current of (3.11) which now radiates in unbounded space. Using methods described in [28], the magnetic field in the far field is found as:

$$H_\alpha = \frac{jk}{\eta}\frac{E_o h}{W}\frac{\cos\left(\frac{kW}{2}\cos\alpha\right)\sin\alpha}{(\pi/W)^2 - (k\cos\alpha)^2}\frac{e^{-jkr}}{r} \tag{3.12}$$

where k and η are the wave number and free space intrinsic impedance, respectively, and α is the angle measured with respect to the x axis. The radiated power is then found by integrating the power density over half space:

$$P_{rad} = \frac{k^2 (E_o hW)^2}{2\pi^3 \eta} \int_0^{\pi} \frac{\cos^2\left(\frac{kW}{2}\cos\alpha\right)\sin^3\alpha}{\left[1-\left(\frac{kW}{\pi}\cos\alpha\right)^2\right]^2} d\alpha \tag{3.13}$$

The electric energy stored in the cavity is calculated using:

$$W_e = \varepsilon_o \varepsilon_r \frac{WhL_a}{16} E_o{}^2 \tag{3.14}$$

where ε_o is the permittivity of free space. Under resonant conditions, L_a is given by:

$$L_a = \frac{\pi/2}{\sqrt{\left(\frac{2\pi f_o}{c}\right)^2 \varepsilon_r - \left(\frac{\pi}{W}\right)^2}} \tag{3.15}$$

Combining (3.13)-(3.15) and using the fact that the stored electric and magnetic energies are equal at resonance, Q_{ext} is given by:

$$\begin{aligned} Q_{ext} &= \frac{4\pi f_o W_e}{P_{rad}} \\ &= \frac{\varepsilon_r \pi^3 c}{16 f_o Wh} \frac{1}{\sqrt{\left(\frac{2\pi f_o}{c}\right)^2 \varepsilon_r - \left(\frac{\pi}{W}\right)^2}} F(W,k) \end{aligned} \tag{3.16}$$

where,

$$F(W,k) = \left[\int_0^{\pi} \frac{\cos^2\left(\frac{kW}{2}\cos\alpha\right)\sin^3\alpha}{\left[1-\left(\frac{kW}{\pi}\cos\alpha\right)^2\right]^2} d\alpha \right]^{-1} \tag{3.17}$$

Equation (3.16) shows the dependence of Q_{ext} on the relative dielectric constant ε_r, the width of the cavity *W*, and the substrate thickness *h*. According to (3.16), Q_{ext} is inversely proportional to *h*. Numerical evaluation of (3.16) suggests that Q_{ext} decreases monotonically with increased *W*. Further examination of (3.16) shows that for a given *W*, Q_{ext} attains a minimum when

$$\varepsilon_{r\min} = \frac{1}{2}\left(\frac{c}{f_o W}\right)^2 \tag{3.18}$$

Equation (3.16) is approximate due to the ideality of the cavity model as well as the assumptions of thin cavity and infinite ground plane. Fig. 3.26 shows Q_{ext} extracted from HFSS simulations for the resonator/antenna structures of Fig. 3.24(a) versus cavity width *W* for substrate heights *h* = 1.57 and 3.17 mm and dielectric constants ε_r = 1, 2.2, and 4. In the same figure, Q_{ext} calculated using equation (3.16) is also shown for comparison. The chosen range of *W* ensures that 10 GHz is above the cutoff frequency of the waveguide. As expected, Q_{ext} of the resonator/antenna structure decreases with increasing substrate thickness and cavity width *W*. Despite being approximate, equation (3.16) predicts the correct trend of the behavior for the resonator/antennas.

(a)

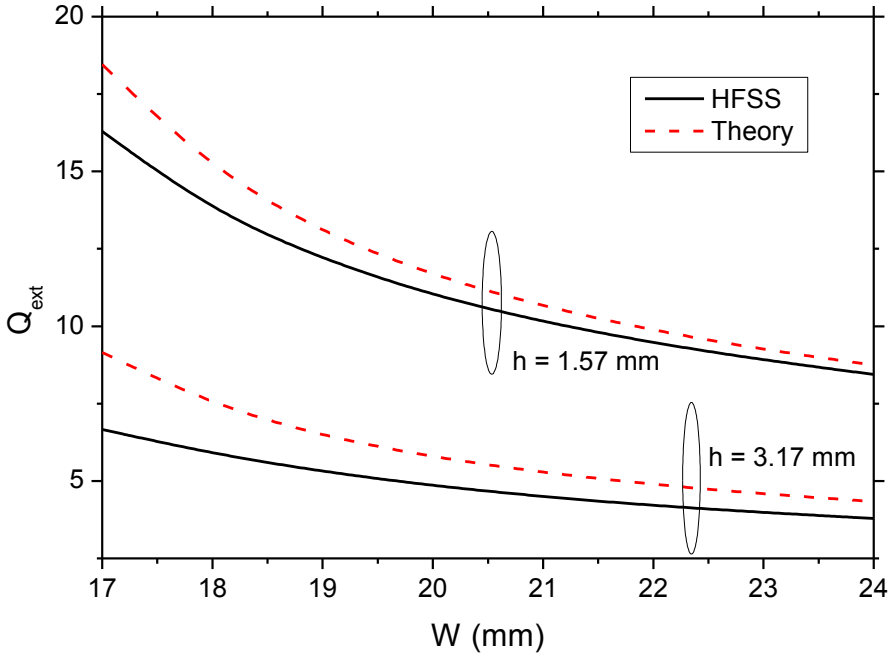
HFSS
Theory
h = 1.57 mm
h = 3.17 mm
Q_{ext}
W (mm)
20
15
10
5
17
18
19
20
21
22
23
24

(b)

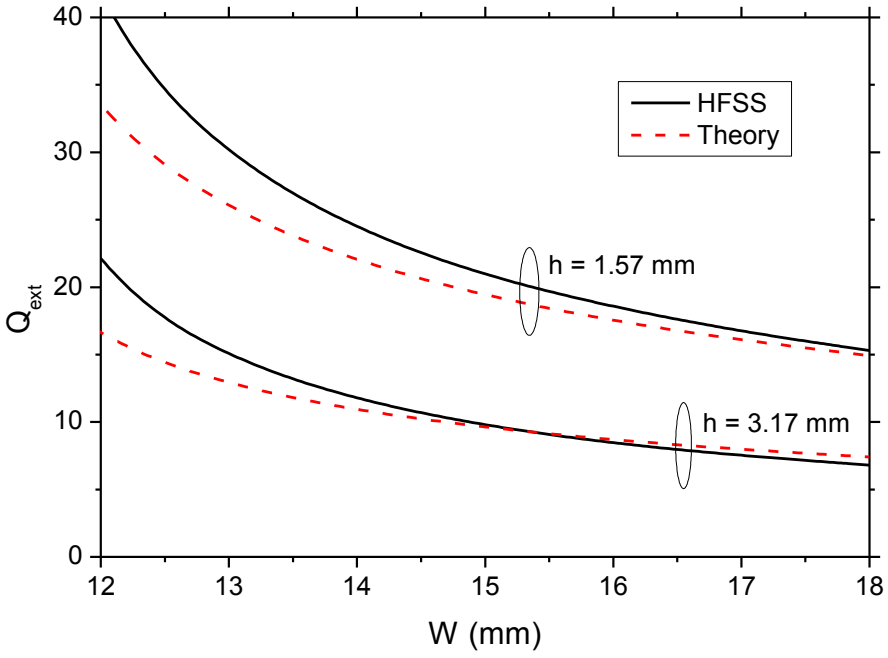
HFSS
Theory
h = 1.57 mm
h = 3.17 mm
Q_{ext}
W (mm)
40
30
20
10
0
12
13
14
15
16
17
18

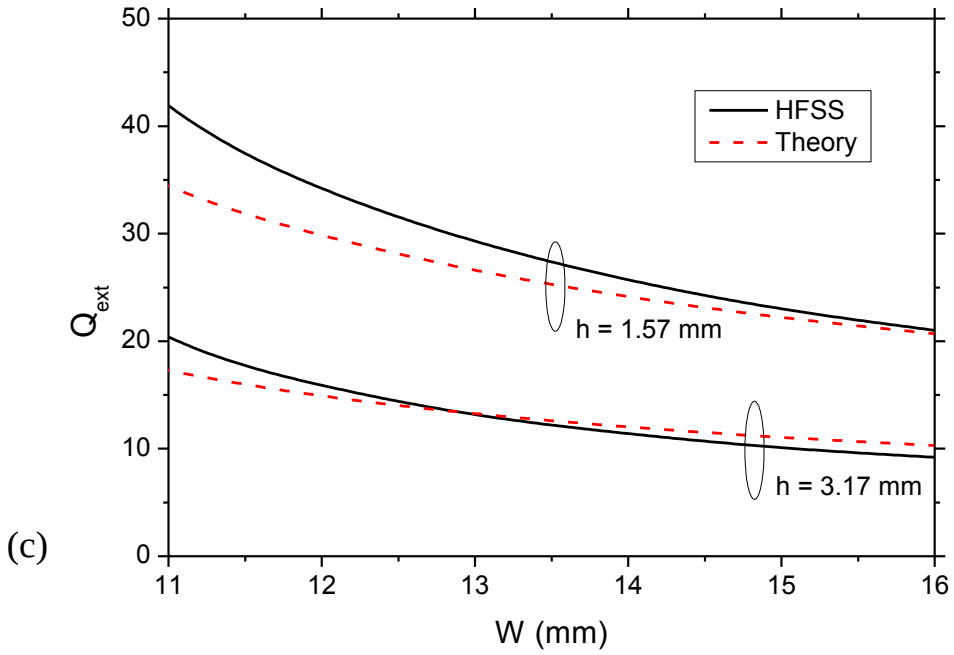

Figure 3.26: Extracted Q_{ext} of the resonator/antennas in Fig. 3.24 versus cavity width W for different h with (a) $\varepsilon_r = 1$, (b) $\varepsilon_r = 2.2$, and (c) $\varepsilon_r = 4$.

3.6 Conclusion

A synthesis approach to seamlessly integrate high-Q filters with highly efficient antennas was presented. This technique can be used for integrated filter/antennas at different frequencies, with different bandwidths, or with different number of orders. It has been shown the integrated slot antenna is a near 100% efficient radiator with expected radiation patterns and gain. In addition, this slot antenna acts as an equivalent load to the filter, without compromising the filtering characteristics. This compact low-loss integration technique enables highly efficient RF front ends with reduced size and higher signal sensitivity.

4 VERTICAL INTEGRATION OF FILTERS WITH SLOT ANTENNAS

4.1 Introduction

The integration of a four-pole 3-D cavity filter with a highly efficient slot antenna was described in Chapter 2, where all four cavity resonators were designed on a single-layer substrate. In applications such as phased arrays, where the spacing between antenna elements is generally limited to less than one wavelength, integrated filter/antenna systems with further reduced footprints are desirable. Under such circumstances, vertically integrated structures present a viable solution.

Vertically integrated high-Q-factor 3-D cavity filters using silicon micromachining [5], low-temperature cofired ceramics (LTCC) [1, 2, 29, 30], and polymer stereolithography [3, 4] have been demonstrated with significantly reduced footprints. In this chapter, we demonstrate the vertical integration of a two-pole cavity filter with a slot antenna, in order to significantly reduce the footprint of the integrated system. The integrated slot antenna is embedded inside the filter and therefore represents zero added volume. Bulky or lossy transitions between the filter and antenna are thus avoided.

Fig. 4.1 shows the schematic of a phased array using the proposed integrated filter/antenna, exhibiting compact size, high-Q filtering characteristics, and reduced co-site interference.

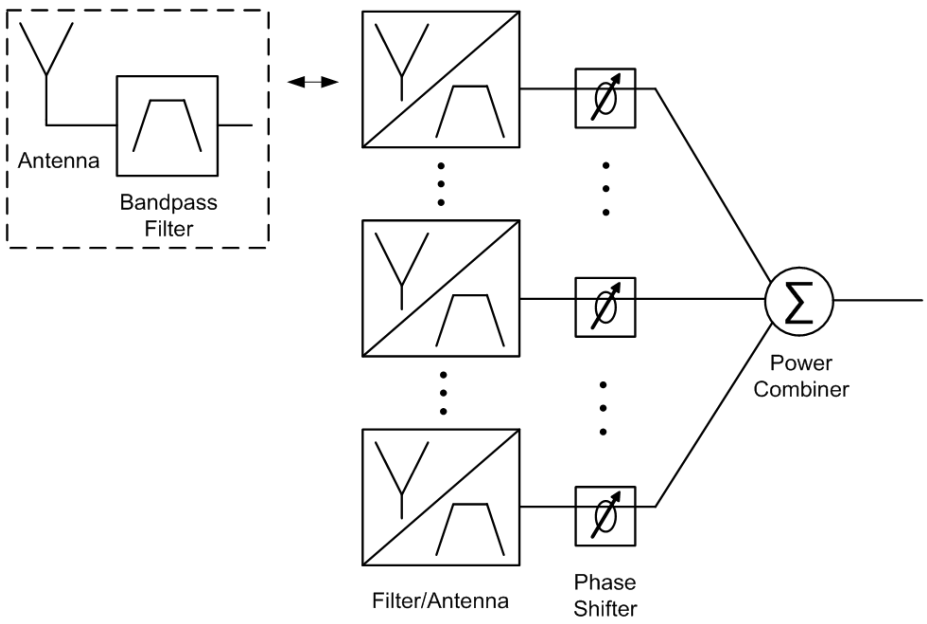

Figure 4.1: Schematic of a phased array with integrated filter/antenna.

It should be noted that vertically integrated filters and filter/antenna systems exhibit increased thickness and therefore extra care should be taken to minimize the potential warpage by selecting metal and dielectric materials with similar coefficients of thermal expansion (CTE) and using appropriate fabrication techniques.

Although the synthesis approach described in the previous chapter can be used to design the vertically integrated structures [31], we opt to use a more generic synthesis approach in this chapter. This approach can be more readily extended for integrated systems with very different filter or antenna structures.

This chapter is organized as follows. Section 4.2 presents the synthesis of a vertical two-pole cavity filter, which is used as a reference for the filter/antenna system. The filter/antenna synthesis procedure is described in Section 4.3.

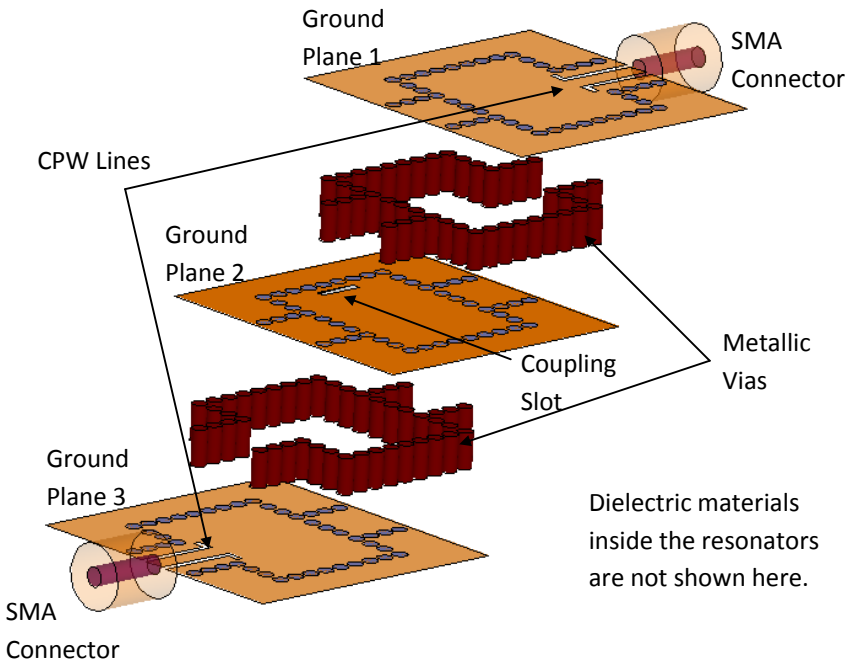

Figure 4.2: Exploded view of a vertical two-pole cavity filter with CPW feeding. SMA connectors are soldered to the CPW lines for measurement purposes.

In Section 4.4, equivalent circuit models are developed to identify the losses in the antenna, which are also verified by full-wave simulations. The measured results are shown and discussed in Section 4.5.

4.2 Filter Synthesis

A vertical two-pole cavity filter is first designed using the approach presented in [7] to serve as a reference for the filter/antenna system. The filter structure is illustrated in Fig. 4.2. The sidewalls of each resonator are formed by closely-spaced metallic vias. The via diameter and spacing are 1 and 1.3 mm, respectively. The internal coupling is achieved through a slot in the ground plane between the two resonators, representing magnetic coupling. The external coupling is realized through the magnetic coupling from the short-ended CPW feeding lines.

(a)

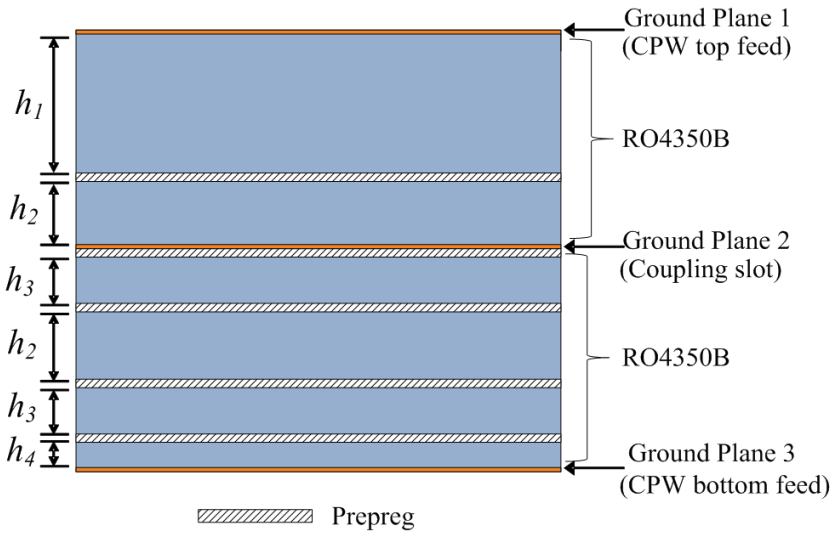

(b)

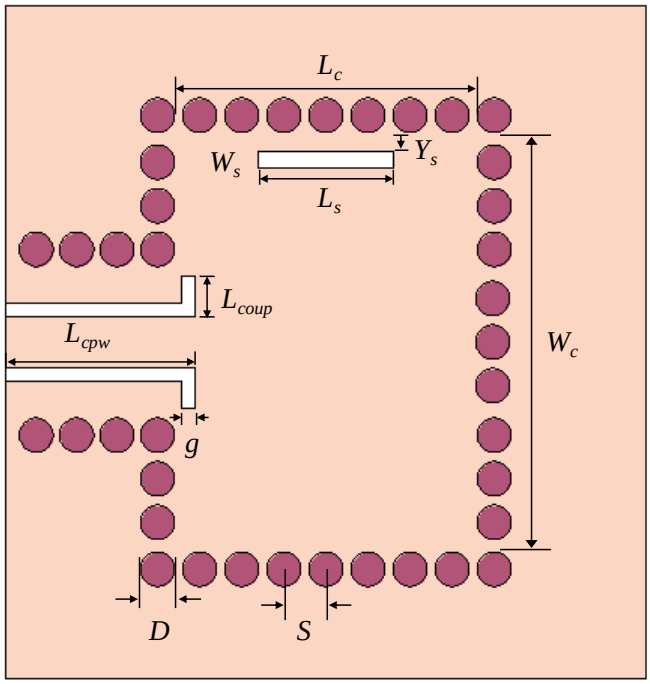

Figure 4.3: (a) Stack and (b) top view of the vertical filter. (Dimensions are in millimeters. h_1 = 1.524; h_2 = 0.762; h_3 = 0.508; h_4 = 0.254; prepreg thickness = 0.1; L_{CPW} = 5.6; L_{Coup} = 1.2; g = 0.4; L_c = 9; W_c = 12.5; D = 1; S = 1.3; L_s = 3.9; W_s = 0.5; Y_s = 0.5)

The center frequency and fractional bandwidth are 10.18 GHz and 2.9%, respectively. The design parameters of the vertical two-pole cavity filter are shown as:

$$k_{12} = 0.021 \tag{4.1}$$

$$Q_{EXT} = 54.4 \tag{4.2}$$

This filter is designed in a multi-layer RO4350B stack as shown in Fig. 4.3(a). The dielectric constant and loss tangent for RO4350B are specified as 3.48 and 0.004, respectively, from Rogers Corp. The prepreg which is used to bond the RO4350B substrates exhibits a dielectric constant of 3.2 and a loss tangent of 0.004. The filter dimensions are shown in Fig. 4.3(b).

4.3 Filter/Antenna Synthesis

The slot antenna is formed by etching the top side of the upper resonator as shown in Fig. 4.4. As a result, this slot antenna does not occupy any additional volume or require any transition structure between the antenna and filter. The slot antenna has a much wider fractional bandwidth than the 2.9% filter bandwidth. Therefore, the slot antenna can act as an equivalent load to the filter within the filter pass band as long as the coupling between the antenna and upper resonator is identical to that between the port and resonator; and the frequency loading from the slot antenna is the same as that from the port. As a result, the filtering function of the filter/antenna system should be identical to that of the same standalone filter. It will be shown in both simulation and measurement results that the slot antenna exhibits the same radiating characteristics in terms of both radiation patterns and gain as a standalone slot antenna. Moreover, the efficiency of this antenna within the integrated structure is much higher than that of the same standalone antenna.

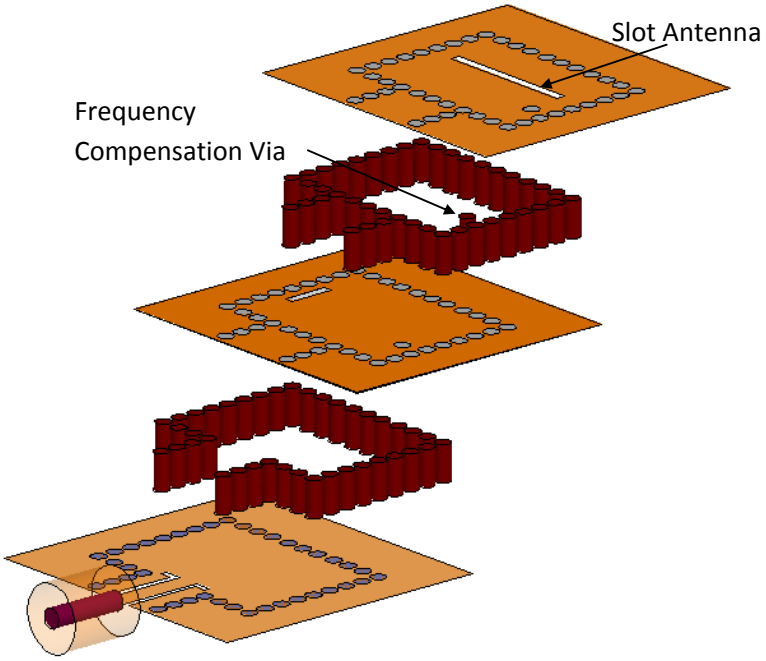

Figure 4.4: Exploded view of a vertical two-pole cavity filter seamlessly integrated with a slot antenna.

This improved efficiency is partly due to the near-zero transition loss between the antenna and filter. Furthermore, since the antenna and filter in the integrated structure share the same substrate, the dielectric and metallic losses are significantly reduced as compared to the discrete case.

4.3.1 Frequency-Domain Slot Antenna Synthesis

The antenna length L_a and width W_a are chosen to be 9.5 and 0.5 mm, respectively. It is noted here that the choice of these two parameters is not unique. Since the slot antenna bandwidth is much wider than the filter bandwidth, slightly different antenna dimensions still cover the filter frequencies.

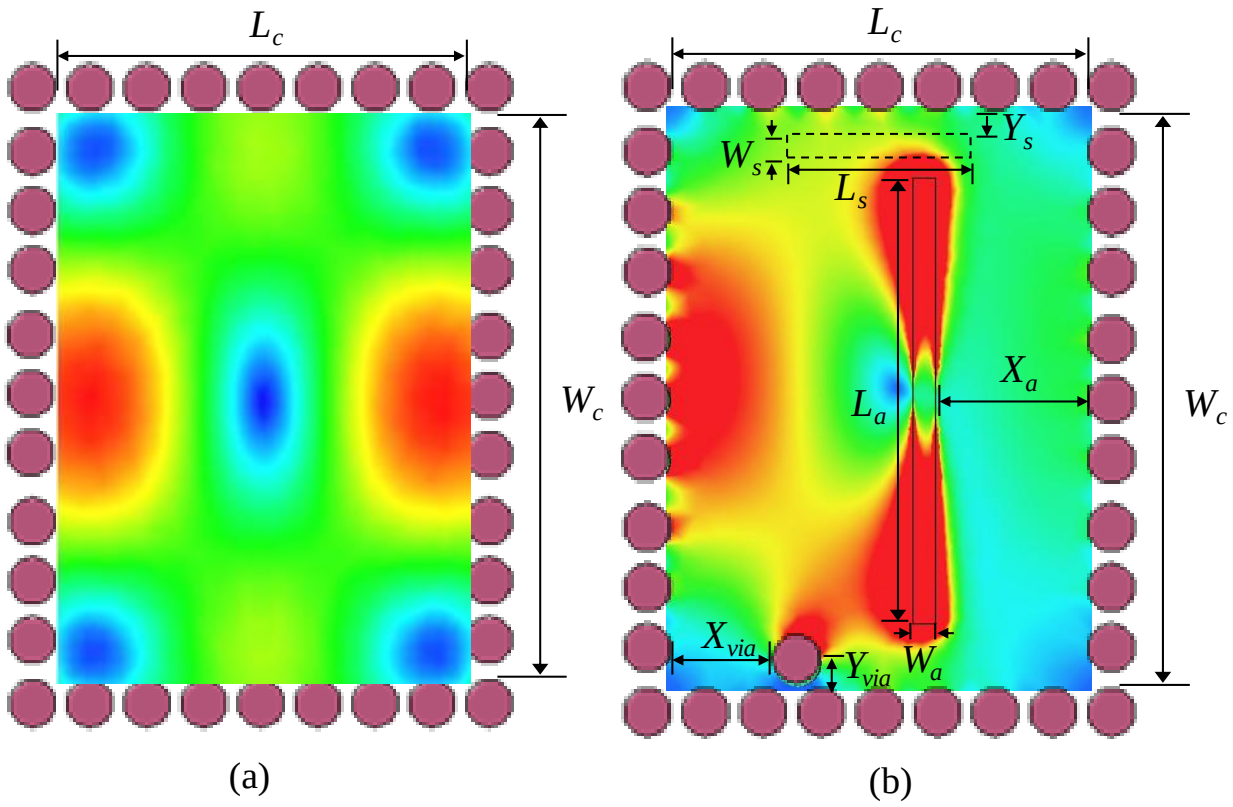

Figure 4.5: Magnetic field distribution at the top of (a) an unperturbed resonator and (b) the upper resonator of the filter antenna. (Dimensions are in millimeters. L_c = 9; W_c = 12.5; L_s = 4; W_s = 0.5; Y_s = 0.5; L_a = 9.5; W_a = 0.5; X_a = 3.3; X_{via} = 2.2; Y_{via} = 0.7)

The slot antenna position X_a controls the coupling between the upper resonator and slot antenna. This coupling is stronger when X_a is smaller, since the magnetic field is stronger at the perimeter of the cavity as shown in Fig. 4.5(a) and the slot antenna predominantly couples to the magnetic field.

Any external coupling detunes the resonant frequency of the upper cavity, so does the slot antenna. It is necessary that this frequency loading effect from the slot antenna be the same as that from the filter port. Therefore, a metallic via inside the upper cavity is used here to adjust the frequency loading caused by the slot antenna as shown in Fig. 4.5(b). The resonant frequency of the upper cavity can be increased with a larger Y_{via} value.

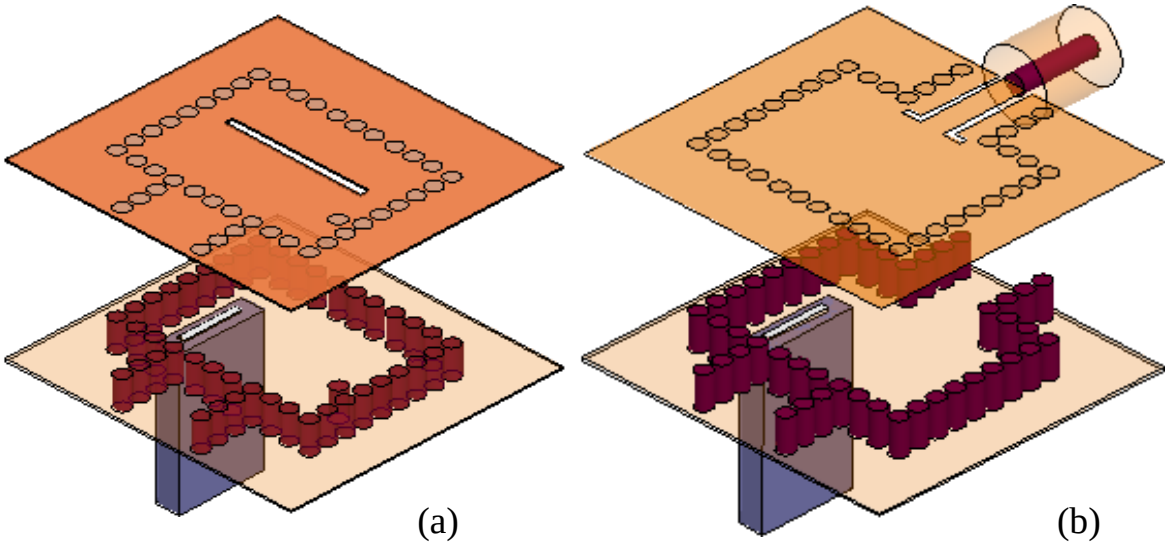

Figure 4.6: Schematics of a cavity resonator terminated with (a) a slot antenna or (b) a 50-ohm port excited by a waveguide port.

Due to the position and orientation of the coupling slot with respect to the slot antenna in Fig. 4.5, the approach used in chapter 3 to design the external coupling to the slot antenna cannot be readily used herein. For this purpose, a more generic method that is amenable to use with other resonator and antenna structures is employed. A waveguide port is used to excite the upper resonator terminated with either a slot antenna as shown in Fig. 4.6(a) or a filter port as shown in Fig. 4.6(b). To achieve reasonably small cross-sectional sizes, i.e. 8 by 1.6 mm herein, the waveguide port is loaded with a dielectric material of ε_r = 10.2. Within 9-11 GHz, this waveguide operates in single-mode condition.

Using the method described in [17], Q_L, which is the parallel combination of Q_U of the upper resonator and Q_{EXT} from the slot antenna or the filter port, can be extracted from the reflection coefficient of the waveguide port.

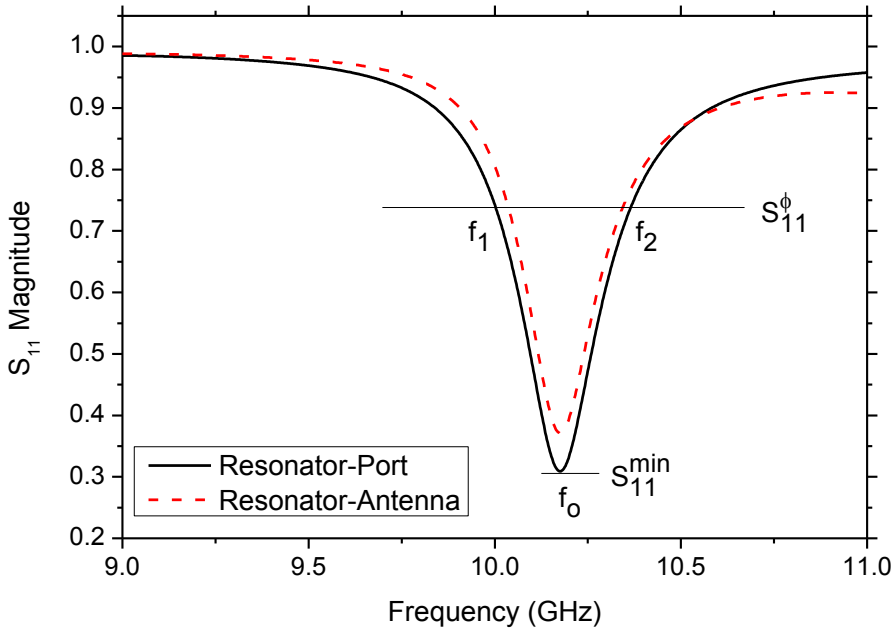

Figure 4.7: Reflection coefficients of the waveguide port for the upper cavity terminated with either a slot antenna (Fig. 4.6(a)) or a filter port (Fig. 4.6(b)).

HFSS full-wave simulations are used to model these structures.S_{11}^{min} is the minimum reflection coefficient occurring at the resonant frequency f_0, as shown in Fig. 4.7. f_1 and f_2 correspond to the frequencies when $S_{11} = S_{11}^{\Phi}$, where S_{11}^{Φ} is defined as:

$$S_{11}^{\phi} = \sqrt{\frac{1+\left|S_{11}^{\min}\right|^2}{2}} \tag{4.3}$$

The coupling coefficient k between the waveguide port and the resonator can be found using:

$$k = \frac{1-S_{11}^{\min}}{1+S_{11}^{\min}} \quad \text{(resonator is under-coupled)} \tag{4.4}$$

$$k = \frac{1+S_{11}^{\min}}{1-S_{11}^{\min}} \quad \text{(resonator is over-coupled)} \tag{4.5}$$

The Q_L can be calculated using:

$$Q_L = (1+k)\frac{f_L}{f_2 - f_1} \tag{4.6}$$

It should be noted that Q_L is independent of S_{11}^{min} since the total loss of the upper cavity due to radiation, metal, and dielectric material is independent of the level of coupling from the waveguide port. This Q_L is found to be 42.6 when the upper cavity is terminated by a filter port. To match this Q_L for the slot antenna case, a parametric sweep of X_a is performed. It should be noted that the frequency loading effect is not constant for different antenna positions. Therefore, a parameter sweep of Y_{via} for each X_a is necessary to achieve the same resonant frequency for every X_a. The reflection coefficient of the waveguide port corresponding to X_a = 3.3 mm and Y_{via} = 0.3 mm is shown in Fig. 4.7. The resonant frequency and Q_L for the slot antenna are 10.18 GHz and 45, respectively, compared with 10.18 GHz and 42.6 for the filter port.

At this juncture, one point of clarification is due. The reader may recall that in Chapter 3 the filter/antenna was designed to have the same response of the reference filter by designing equal Q_{ext} rather than Q_L. Strictly speaking, the responses of the two structures can be made identical only if both Q_{ext} and Q_L are the same in the two cases. This is most easily seen by examining equations (2.20) and (2.21) in Chapter 2 for the expressions of S_{11} and S_{21}. If the unloaded Q-factors of the second resonators in the two structures are different due to increased losses in one case compared to the other, it is possible, by matching Q_L, to design the two structures to have the same S_{11} but not the same S_{21}. This is evident by examining equation (2.20), where Q_L, the parallel combination of Q_{o2} and $Q_{ext,2}$ only explicitly appears. Informally speaking, the input port only feels the effect of the total energy dissipation in the second resonator, and cannot tell where

the energy is being dissipated, whether it is mostly coupled to the output port or lost as heat due to dielectric and metal loss. Under such conditions, the effect of different unloaded Q-factors appears as a change in efficiency as seen by equation (2.21).

In Chapter 3, due to the low loss of the substrate used, the integration of the slot antenna introduced negligible extra losses and the unloaded Q-factor of the last resonator was unchanged. It was therefore sufficient to design for the same Q_{ext}. In this chapter, as we shall see in section 4.4, due to the relatively lossy substrate used, it was necessary to consider the effects of the degradation of the unloaded Q-factor by designing for equal Q_L rather than equal Q_{ext}.

4.3.2 Time-Domain (TD) Filter/Antenna Synthesis

The frequency-domain responses of the reference filter and filter/antenna are shown in Fig. 4.8(a). The gain of the filter/antenna closely follows the S_{21} of the reference filter. The gain of the filter/antenna and the insertion loss of the filter are found to be 4.9 and 2.18 dB, respectively, at the center frequency. However, the S_{11} of the filter/antenna is noticeably different from that of the filter.

Fine tuning the filter/antenna dimensions in frequency domain using full-wave simulation tools such as HFSS can be very time consuming and therefore the time-domain technique [27] is used here to complete the filter/antenna synthesis. The filter S_{11} response is plotted in the time domain as shown in Fig. 4.8(b). The peaks in the time-domain response correspond to the external coupling between Port 1 and the first resonator ($Q_{ext,\,1}$), the internal coupling between resonators 1 and 2 (k_{12}), and the external coupling between the second resonator and Port 2 ($Q_{ext,\,2}$), respectively, from left to right.

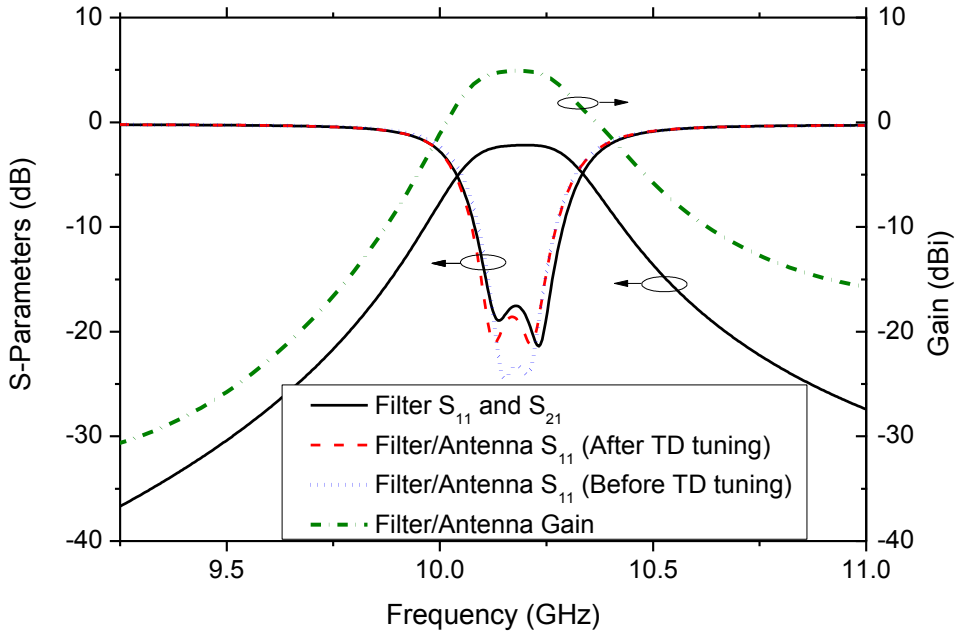

(a)

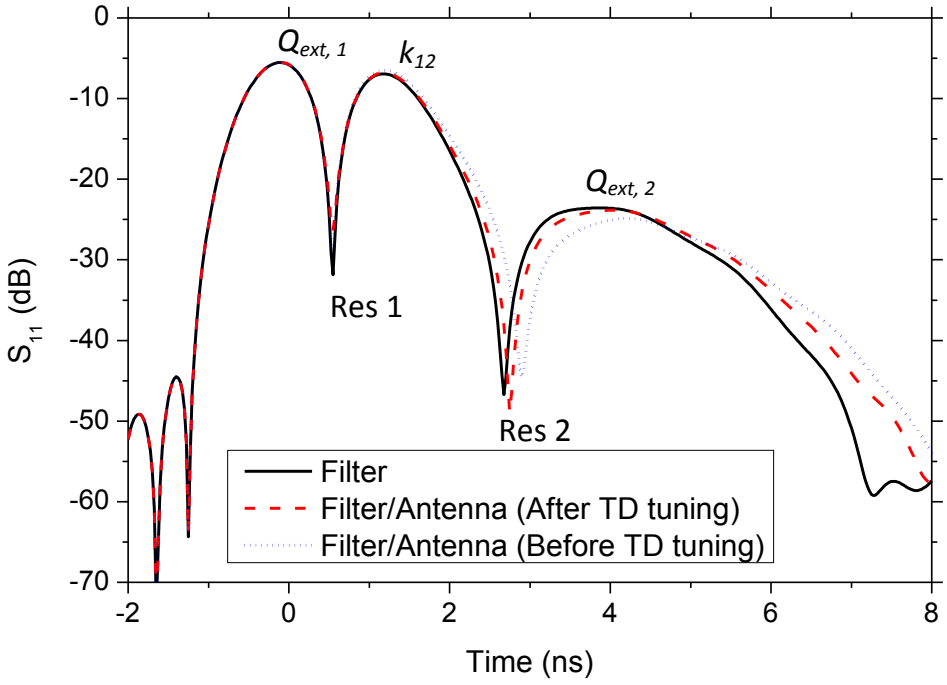

(b)

Figure 4.8: Simulated filter and filter/antenna responses in (a) frequency domain and (b) time domain.

The dips correspond to the resonators 1 and 2, respectively. It is observed in Fig. 4.8(b) that the peak corresponding to k_{12} of the filter/antenna is higher than the filter case, which implies that the reflection from the coupling slot is a little bit too high. Therefore, the coupling slot dimensions need to be increased to allow more coupling between the two resonators. A parametric sweep of L_s is then performed to match the peaks corresponding to k_{12} between the filter and filter/antenna cases. It is found that an L_s value of 4 mm provides the best match in the time-domain S_{11} responses as shown in Fig. 4.8(b). The return losses for both filter and filter/antenna in the frequency domain are shown to be close to each other as illustrated in Fig. 4.8(a). The final dimensions of the filter/antenna are listed in Fig. 4.5(b).

4.4 Q Breakdown and Loss Analysis

Sections 4.3.1 and 4.3.2 presented the synthesis of a filter/antenna system exhibiting the same filtering characteristics as the reference filter. In this section, equivalent circuits are developed to model the loss associated with this filter/antenna integration.

The structures shown in Fig. 4.6 can be modeled by an equivalent circuit illustrated in Fig. 4.9(a). It is noted that the Q_L calculated by (4.6) is expressed by:

$$\frac{1}{Q_L} = \frac{1}{Q_o} + \frac{1}{Q_{EXT}} = \frac{R_2}{\omega_0 L_2} + \frac{K_{23}^2 / Z_0}{\omega_0 L_2} \tag{4.7}$$

Q_{EXT} is equal to Q_L when Q_o is infinity. This can be realized by removing the metal and dielectric losses in HFSS simulations of the structures shown in Fig. 4.6. It is found that for the filter, Q_L, Q_o and Q_{EXT} are 42.6, 196 and 54.4, respectively. For the filter/antenna, the three parameters are 45, 187, and 59.4, respectively.

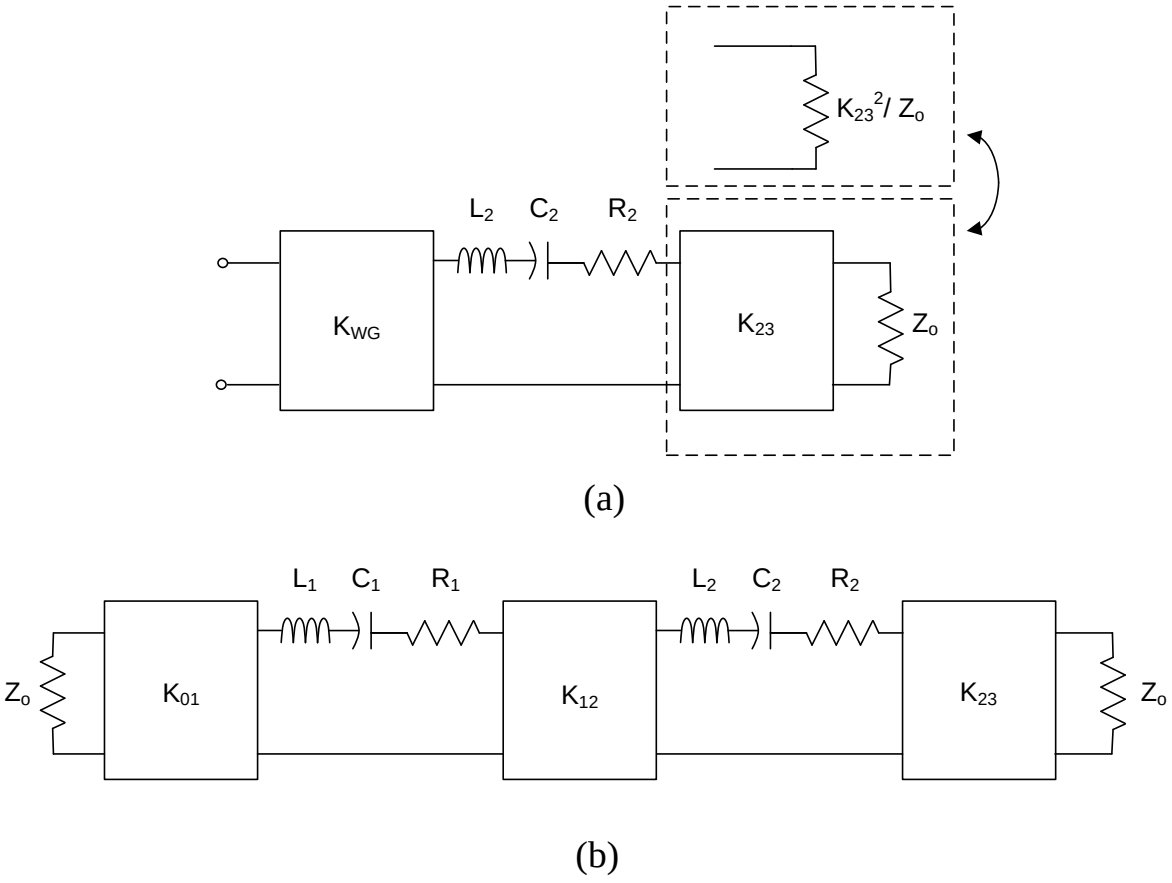

Figure 4.9: Equivalent circuits of the structures (a) in Fig. 4.6 and (b) in Figs. 2&4. (Filter: L_1 = L_2 = 3 nH, C_1 = 0.0815 pF, C_2 = 0.0816 pF, R_1 = R_2 = 0.979 Ω, K_{01} = K_{23} = 13.3 Ω, K_{12} = 4.02 Ω, Z_0 = 50 Ω) (Filter/Antenna: L_1 = L_2 = 3 nH, C_1 = C_2 = 0.0815 pF, R_1 = 0.979 Ω, R_2 = 1.03 Ω, K_{01} = 13.3 Ω, K_{12} = 3.9 Ω, K_{23} = 12.7 Ω, Z_0 = 50 Ω)

It is noted that the Q_{EXT} is very different between the two cases. In addition, the Q_o is degraded from 196 to 187 for the upper resonator loaded with the slot antenna. *However, in order to realize the same reflection coefficient, the same Q_L not Q_{EXT} is necessary*. This has been proven in the synthesis procedure described in Section 4.3.1.

The equivalent circuit model for the entire filter or filter/antenna is illustrated in Fig. 4.9(b). Using the Q_o and Q_{EXT} values found through HFSS simulations, the values of the circuit elements are calculated and presented in Fig. 4.9.

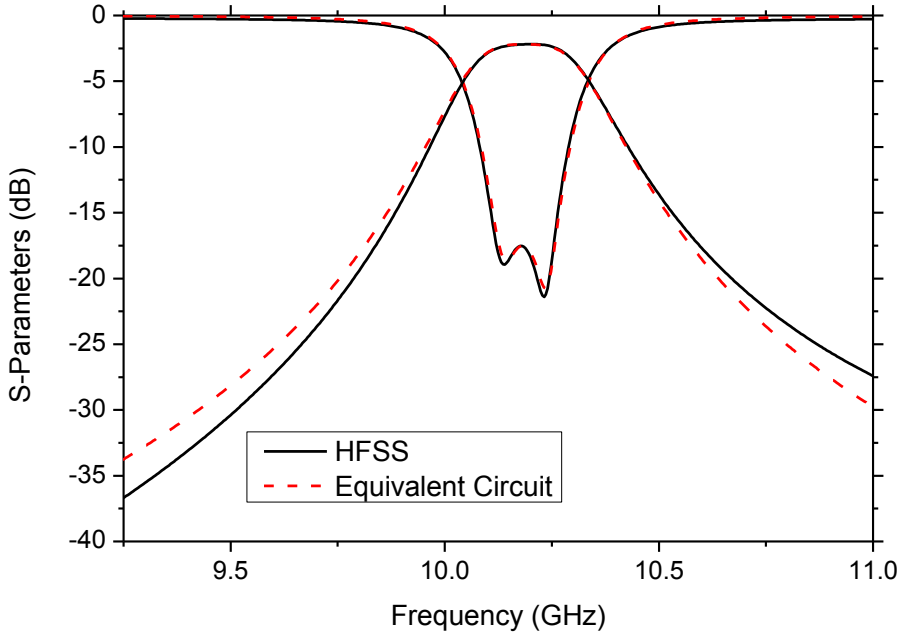

(a)

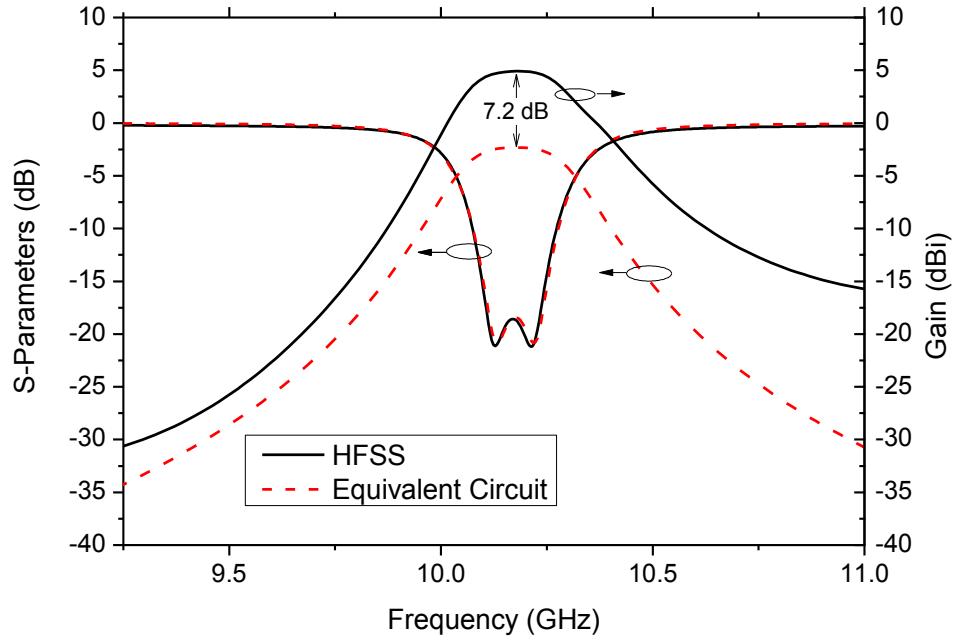

(b)

Figure 4.10: (a) Filter S_{11} and S_{21} using HFSS simulation and equivalent circuit. (b) Filter/antenna S_{11} and gain using HFSS simulation as well as filter/antenna S_{11} and S_{21} using equivalent circuit.

The S_{11} and S_{21} of the filter using both HFSS simulations and equivalent circuit model are compared in Fig. 4.10(a) and closely match each other, particularly within the pass band. Using the equivalent circuit model, it is found that the asymmetric S_{11} response in the passband is due to a 0.05% frequency difference between the two resonators, which is caused by the different number of prepreg layers within the two cavities.

The insertion loss of the filter/antenna system from the equivalent circuit model is found to be 2.3 dB, compared with 2.18 dB for the filter. This 0.12-dB difference is due to the removal of one CPW feeding and addition of one slot antenna. Using HFSS simulations, it is found that the attenuation of one CPW feeding line is 0.035 dB. Therefore the efficiency of the slot antenna is calculated to be 97%, equivalent to a 0.155-dB loss. To verify this loss from the equivalent circuit model, HFSS simulations are performed to find the overall efficiency of the filter/antenna system. This overall efficiency is shown to be 58.9%, which is equivalent to a 2.3-dB loss. From both equivalent circuit model and full-wave simulations, it is observed that (1) the slot antenna has a very high (97%) efficiency, and (2) near zero loss occurs in the transition between the filter and antenna. Very close agreement in S_{11} is observed as shown in Fig. 4.10(b). The S_{21} from the equivalent circuit closely follows the roll off of the gain obtained from HFSS simulations. The 7.2-dB difference between the two curves is due to the fact that the equivalent circuit model does not take the 7.2-dB antenna directivity into consideration.

4.5 Results and Discussion

An integrated filter/antenna system is fabricated and measured. As shown in Fig. 4.11(a), SMA connectors are soldered to the CPW lines for measurement purposes.

The measured filter/antenna center frequency of 10.16 GHz is very close to the simulated 10.18 GHz as shown in Fig. 4.11(b). The measured bandwidth of 3.0% is slightly larger than the simulated 2.7% for the filter/antenna.

The measured impedance matching is better than 28 dB within the passband. The measured filtering shape matches the simulated result very well. The radiation patterns and gain are measured. As shown in Fig. 4.12, the measured radiation patterns agree very well with the simulation results in both H- and E-planes at the center frequency.

The small discrepancy in the backside lobes is caused by the finite ground plane size and scattering effects from the connectors and cables. Although the radiations patterns shown in Fig. 4.12 correspond to the filter/antenna center frequency f_0, similar radiation patterns are observed across the entire passband of the filter/antenna.

The measured maximum gain at the boresight of the radiation pattern is shown to be 4.9 dB, which is identical to the simulated gain. Given the 7.2-dB directivity from HFSS simulations, the overall efficiency of the filter/antenna from the measurement is calculated to be 58.9% as well, which implies that a 97% efficient slot antenna is achieved based on the calculations shown in Section 4.4. 3-D cavity resonators loaded with air dielectric have the potential to achieve unloaded Q factors up to several thousand [3]. Using SIW cavity resonators loaded with RT/Duroid 5880 substrate material, unloaded Q factors as high as 850 were demonstrated in Chapter 3. Using these low-loss cavity resonators, the filter insertion loss can be greatly improved. As a result, the noise figure of the RF front end is significantly reduced. In this Chapter, the choice of the substrate material and stack is not optimum for loss performance.

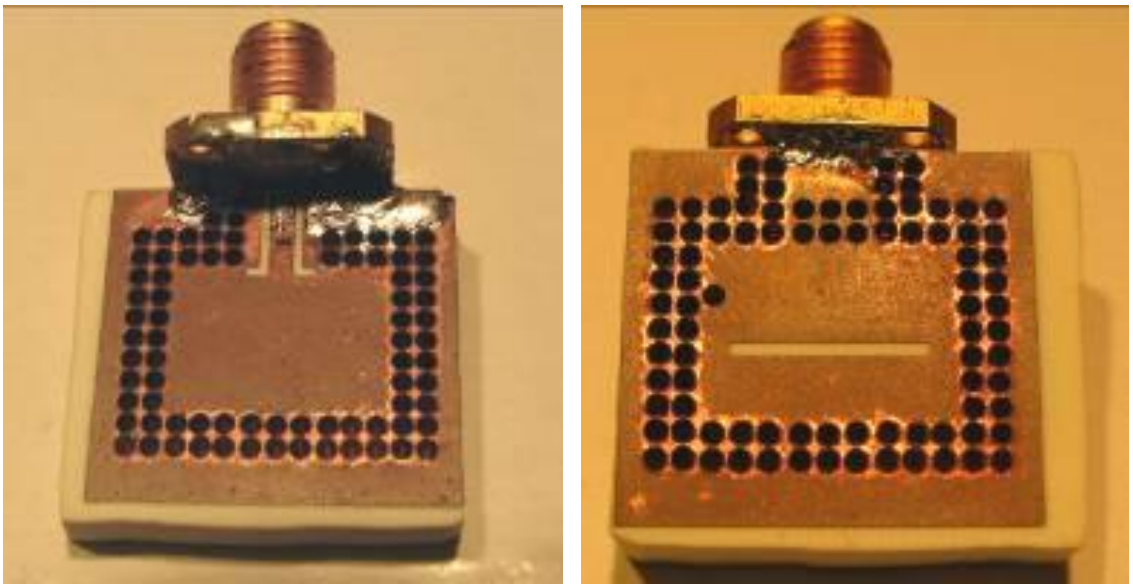

Bottom View (CPW Feed) Top View (Slot Antenna)

(a)

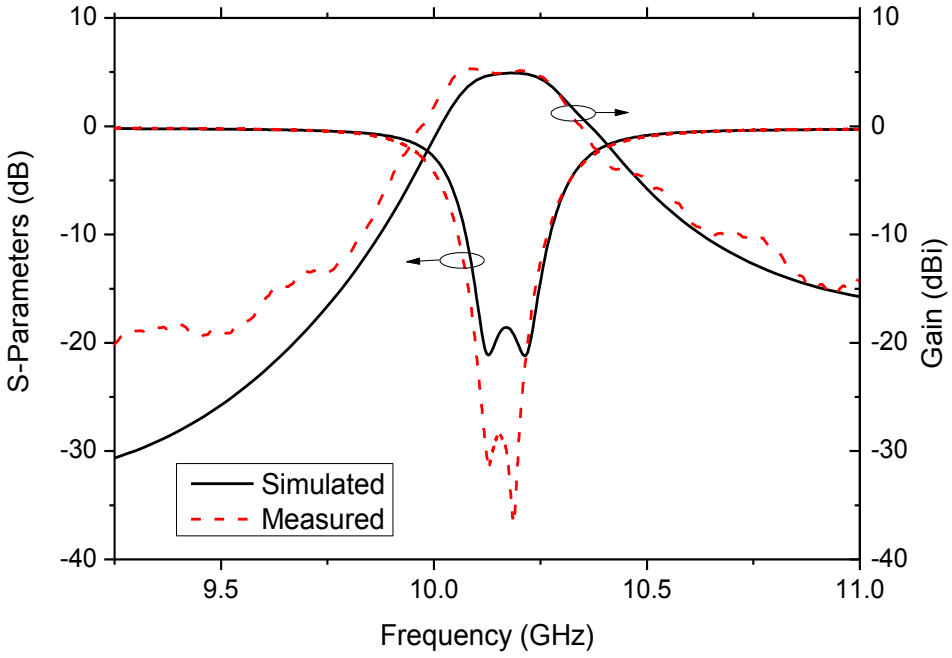

(b)

Figure 4.11: (a) Photo of fabricated filter/antenna, and (b) Simulated and measured S_{11} and gain

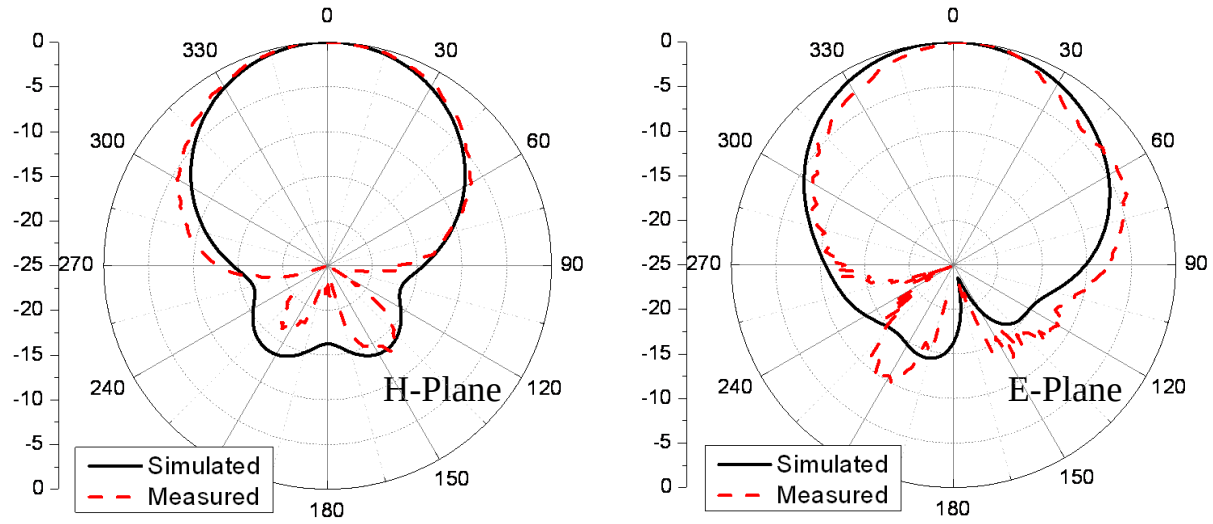

Figure 4.12: Measured and simulated radiation patterns of the filter/antenna at f_0.

However, even with the relatively lossy RO4350B substrates, antenna efficiency as high as 97% is still achieved. To demonstrate the possibility of realizing a highly efficient filter/antenna system, we reduce the loss tangent of RO4350B and prepreg in HFSS to emulate a resonator with an unloaded Q of 1,000. It is found that the filter insertion loss is reduced to 0.5 dB and the antenna efficiency is still as high as 97%, leading to an 86% overall efficiency for the filter/antenna system. Using this low-loss substrate, the simulated gain of the filter/antenna system is as high as 6.58 dB.

4.6 Conclusion

A synthesis approach to seamlessly integrate 3-D vertical filters with highly efficient antennas was presented. The measured results verified the presented synthesis approach. It has been shown that the integrated slot antenna is a 97% efficient radiator with expected radiation patterns and gain. In addition, this slot antenna acts as an equivalent load to the filter, without compromising the filtering characteristics. This compact low-loss integration technique enables low-loss filtering and reduces co-site interference within phased arrays. Following the same

synthesis procedure, higher-order filters can also be seamlessly integrated with highly efficient slot antennas.

5 INTEGRATION OF FILTERS WITH APERTURE ANTENNAS

5.1 Introduction

A synthesis technique to integrate high-Q 3-D filters with highly efficient slot antennas was presented in Chapter 3. Using the new technique, integrated filter/antenna systems with significantly reduced form factors and high system efficiencies were demonstrated. To further reduce the footprint of the integrated systems, slot antennas integrated with vertical cavity filters were demonstrated in Chapter 4.

In this Chapter, we demonstrate the integration of cavity filters with an alternative antenna structure which enables larger bandwidths compared with what can be obtained using the structures in Chapters 3 and 4.

The antenna may be described as an open-ended waveguide aperture mounted on a ground plane as illustrated in Fig. 5.1. In addition to the fields radiated directly at the aperture, a portion of the energy is coupled to the dielectric-air interface as surface waves which travel along the structure and get radiated at its end. By carefully designing this structure, it is shown that the surface wave radiation can augment the direct aperture radiation and result in a broadside radiation pattern similar to a slot antenna. The excitation of surface waves presents an additional loss mechanism from the view point of the last resonator of the filter/antenna structure, and therefore, lower Q_{ext} can be achieved. This, in turn, allows the design of filter/antenna systems with larger bandwidths compared with those presented in Chapters 3 and 4, while preserving the desirable compactness and high efficiency. It is shown that Q_{ext} in the range of 4-43 can be realized within the range of physical parameters used in this study.

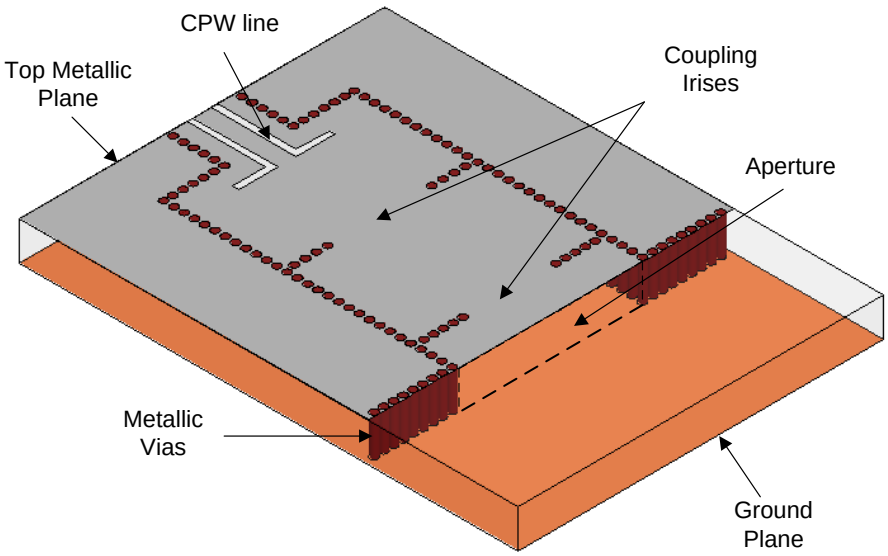

Figure 5.1: Schematic of a three-pole cavity filter integrated with an aperture antenna over a ground plane.

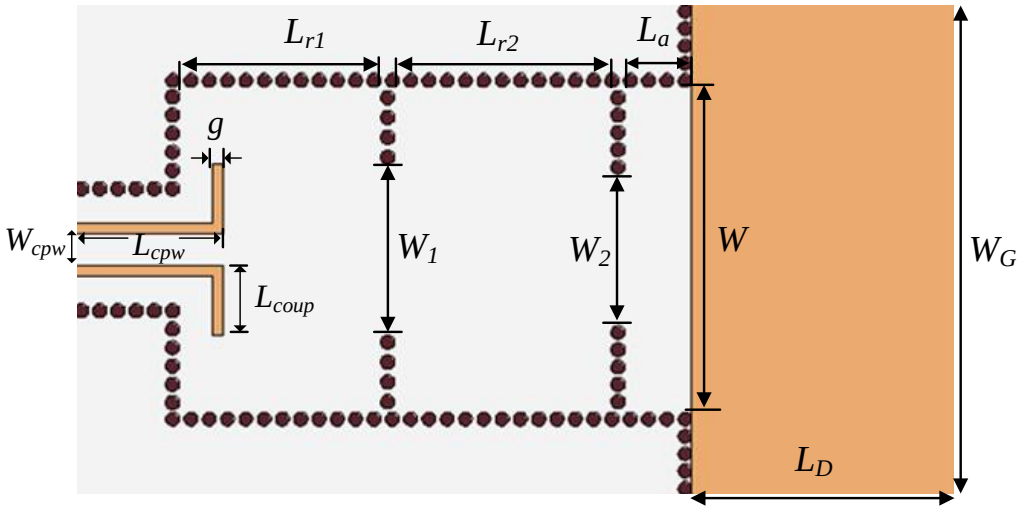

Figure 5.2: Top view of an integrated cavity filter with an aperture antenna. 34% FBW on 3.17-mm thick substrate

(W = 15; W_{cpw} = 1.5; L_{cpw} = 6.5; L_{coup} = 5.4; g = 0.5; W_1 = 8.2; W_2 = 7.5; L_{r1} = 9.7; L_{r2} = 9.7; L_a = 2.9; L_D = 10; W_G = 30). 8% FBW on 1.57-mm thick substrate (W = 13; W_{cpw} = 1.5; L_{cpw} = 7.4; L_{coup} = 2.3; g = 0.5; W_1 = 5.6; W_2 = 5; L_{r1} = 13.2; L_{r2} = 13.7; L_a = 5.9; L_D = 12.3; W_G = 30). Dimensions are in mm.

A 34% FBW three-pole filter/antenna, corresponding to Q_{ext} of 4.4, is designed to demonstrate the widest bandwidth for this integrated filter/antenna structure. The overall efficiency of such system is found to be as high as 96% in full-wave simulations.

5.2 Filter/Antenna Synthesis

The top view of a three-pole Chebyshev bandpass filter integrated with an aperture antenna is shown in Fig. 5.2. The inter-resonator coupling between cavities is achieved through irises in the common sidewalls. External coupling to the first cavity, on the other hand, is realized through the magnetic coupling from the short-ended CPW line. The third cavity is cut open forming an aperture over an extended ground plane. This resonator/antenna contributes to a third pole in the filtering function while simultaneously acting as a radiating element. The extended ground plane directs the radiation upwards causing the structure to act as a broadside radiator.

In order to synthesize a filter/antenna with a prescribed filtering function, it is necessary to be able to design the resonator/antenna's Q_{ext} and its coupling to the preceding resonator as required by the filtering function. The design of Q_{ext} is described in the next section.

5.2.1 Resonator/Antenna Q_{ext}

The resonator/antenna of the filter/antenna system is shown in Fig. 5.3(a). This structure exhibits a resonance behavior analogous to a series *RLC* circuit. The input impedance of the resonator/antenna as seen from the waveguide port depicted in Fig. 5.3(a) is simulated using Ansoft High Frequency Structure Simulator (HFSS) and compared with a series *RLC* resonator in Fig. 5.4. The close agreement between the two cases is apparent around the resonant frequency f_o = 10 GHz, which is chosen to be center frequency of the filter/antenna system.

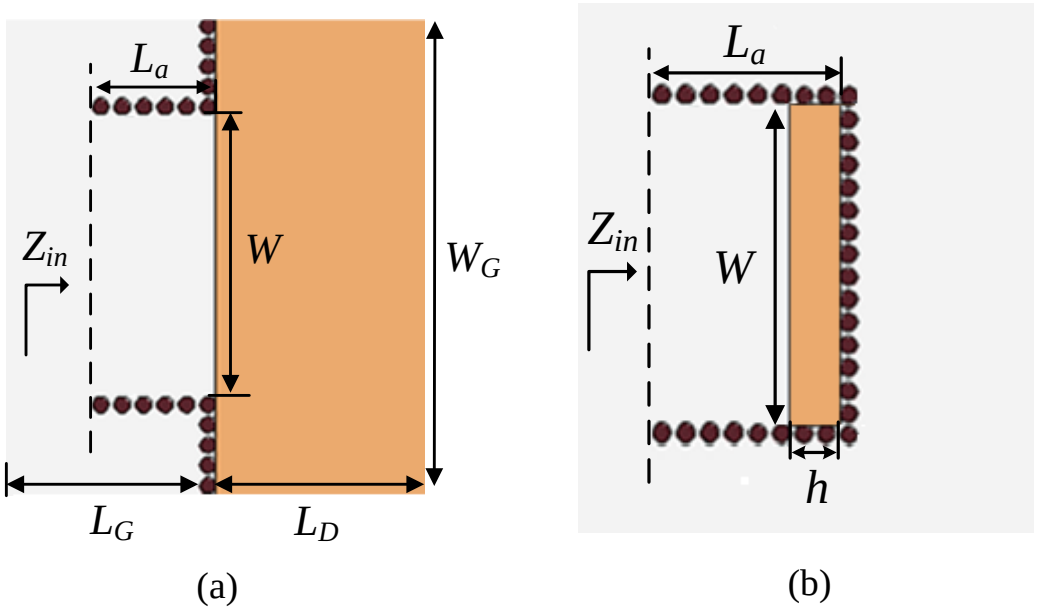

Figure 5.3: Schematic of the resonator/antenna with aperture on (a) side and (b) top.

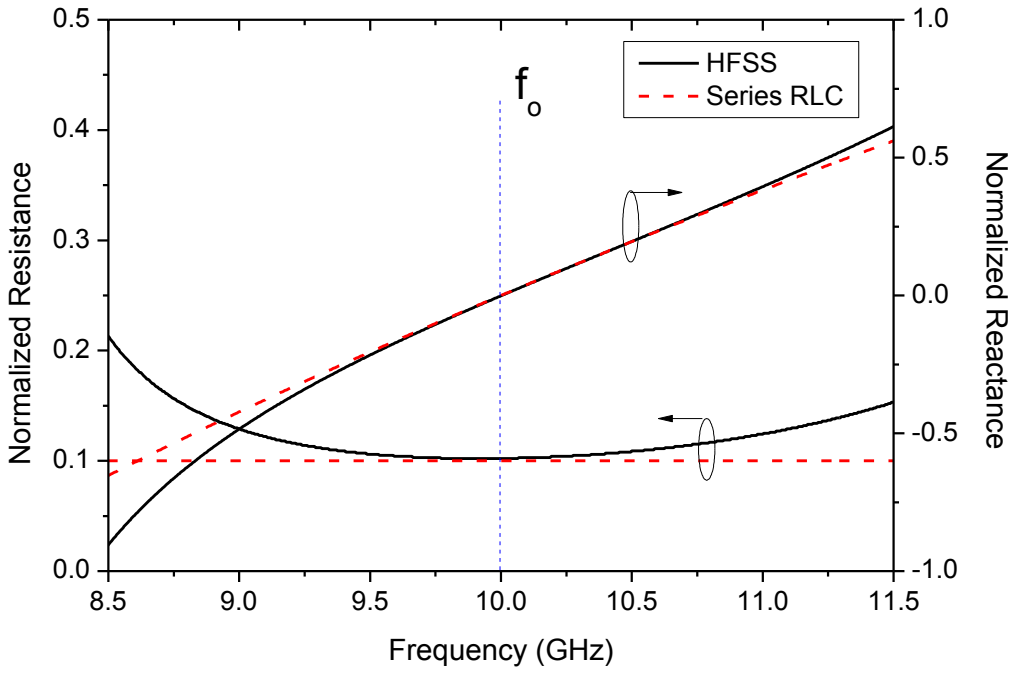

Figure 5.4: Normalized impedance of the resonator/antenna compared with a series *RLC* circuit.

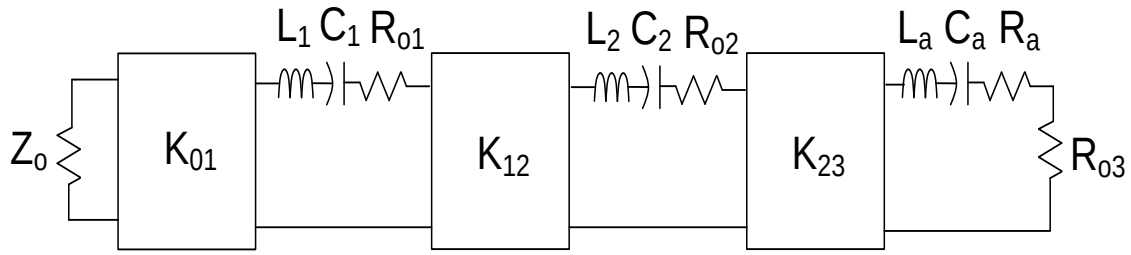

Figure 5.5: Equivalent circuit of the filter/antenna system.

Using the series *RLC* equivalent of the resonator/antenna, the equivalent circuit of the entire filter/antenna system can be constructed as shown in Fig. 5.5. *K* inverters are used to represent the external coupling from the input port to the first resonator and the inter-resonator coupling between the cavity resonators. The resistances R_{o1}, R_{o2}, and R_{o3} account for the unloaded Q factors of the resonators.

We have already seen the resonator/antenna (Fig. 5.3(a)) in Chapter 3 when we considered the effect of physical parameters on the achievable $Q_{ext.}$ The dielectric material was assumed to be truncated beyond the aperture and the structure was analyzed using the cavity model. In this chapter, we consider the presence of a dielectric and hence the possibility of surface wave excitation. In addition to the resonator/antenna of Fig. 5.3(a), the resonator/antenna structure shown in Fig. 5.3(b) in which the aperture is moved to the top metallic plane is also considered. The possibility of surface wave excitation in Fig. 5.3(a) constitutes the main difference between the two alternative structures. In what follows, a comparison of the two structures is found helpful in understanding their respective features.

(a)

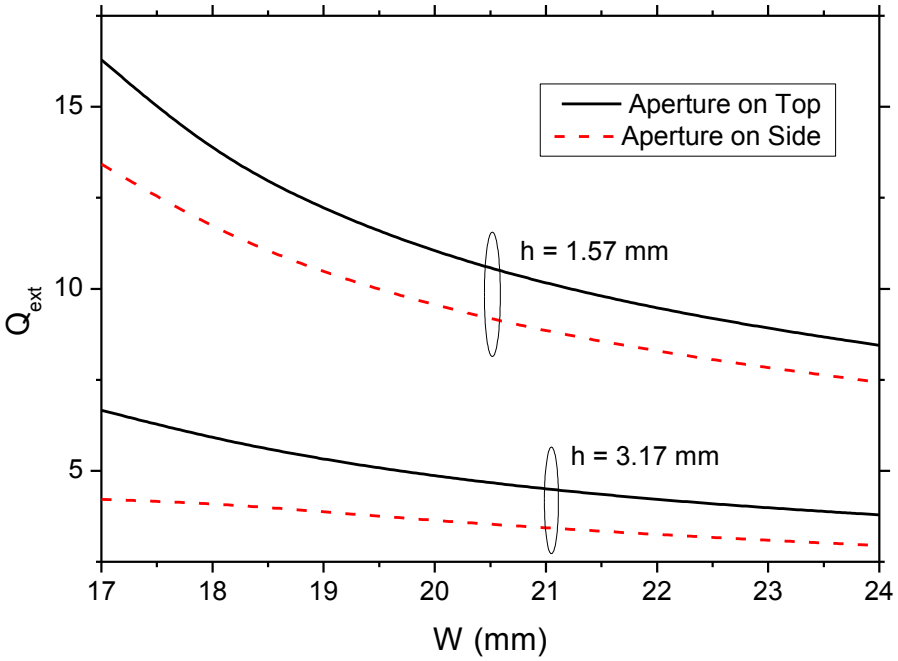
Aperture on Top
Aperture on Side
h = 1.57 mm
h = 3.17 mm
Q_{ext}
W (mm)
15
10
5
17
18
19
20
21
22
23
24

(b)

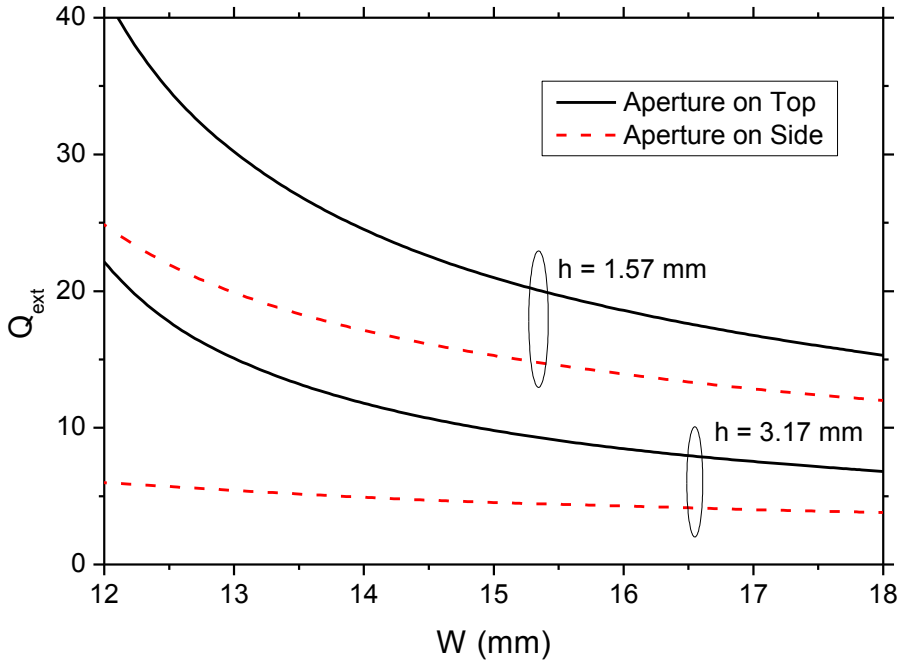
Aperture on Top
Aperture on Side
h = 1.57 mm
h = 3.17 mm
Q_{ext}
W (mm)
40
30
20
10
0
12
13
14
15
16
17
18

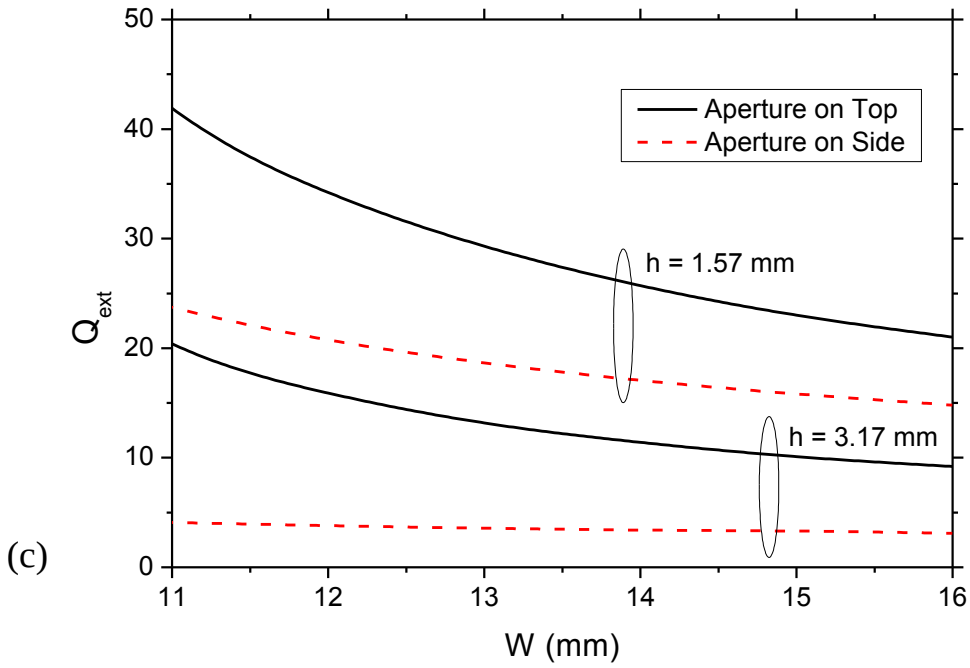

Figure 5.6: Extracted Q_{ext} of the resonator/antennas in Figure 5.3 versus aperture width W for different h with (a) ε_r = 1, (b) ε_r = 2.2, and (c) ε_r = 4.

Fig. 5.6 shows Q_{ext} extracted from HFSS simulations for the two resonator/antenna structures of Fig. 5.3 versus aperture width W for substrate heights h = 1.57 and 3.17 mm and dielectric constants ε_r = 1, 2.2, and 4. The chosen range of W ensures that 10 GHz is above the cutoff frequency of the waveguide. It is noted that for the same dielectric constant, substrate thickness, and aperture width, the resonator/antenna with aperture on the side exhibits smaller Q_{ext} compared with the case with aperture on top. It is interesting to note that this behavior is also observed in the air-filled resonator/antenna where no surface waves can be excited. Furthermore, Q_{ext} of both resonator/antenna structures decreases with increasing substrate thickness and aperture width W.

By carefully examining Fig. 5.6(a)-(c), it is seen that the relative difference of Q_{ext} attained by the two resonator/antenna structures increases with increased substrate thickness and dielectric constant values. This is attributed to the increased excitation of surface waves for the

resonator/antenna in Fig. 5.3(a) under those conditions, a general characteristic exhibited by printed antennas [32].

Fig. 5.7 shows the longitudinal electric field component characteristic of the dominant TM_0 surface wave along the resonator/antenna structure in Fig. 5.3(a) when ε_r = 2.2. The fields of an air-filled resonator/antenna are plotted in the same figure for comparison purposes. In the vicinity of the aperture, the fields are composed of space waves and higher-order waves directly radiated by the aperture in addition to surface waves coupled to the air-dielectric interface. As the space waves decrease away from the aperture, the surface wave separates itself from the aperture near field [33] and is discernible at 10 mm. It is possible to observe a distinct surface wave provided the dimension L_D is made long enough. It is shown in section 5.2.2 that, however, L_D should be kept small if boresight radiation of the resonator/antenna is to be maintained. In these cases, despite being excited, the surface wave is not observed as separate from the aperture near field. The surface wave gets mostly radiated when it reaches the end of the structure albeit being partly reflected. The radiation from the surface wave augments the direct radiation from the aperture and can be utilized to yield a useful broadside radiation pattern. The smaller achievable values of Q_{ext} enabled by the utilization of the surface wave radiation allows the design of filter/antenna systems with larger bandwidths compared with those presented in Chapters 3 and 4.

Due to the partial reflection of the surface and the space waves at the end of the structure, Q_{ext} is seen to have an interesting quasi-periodic dependence on the dimension L_D. Fig. 5.8 shows extracted Q_{ext} for the resonator/antenna for different dielectric constants versus L_D.

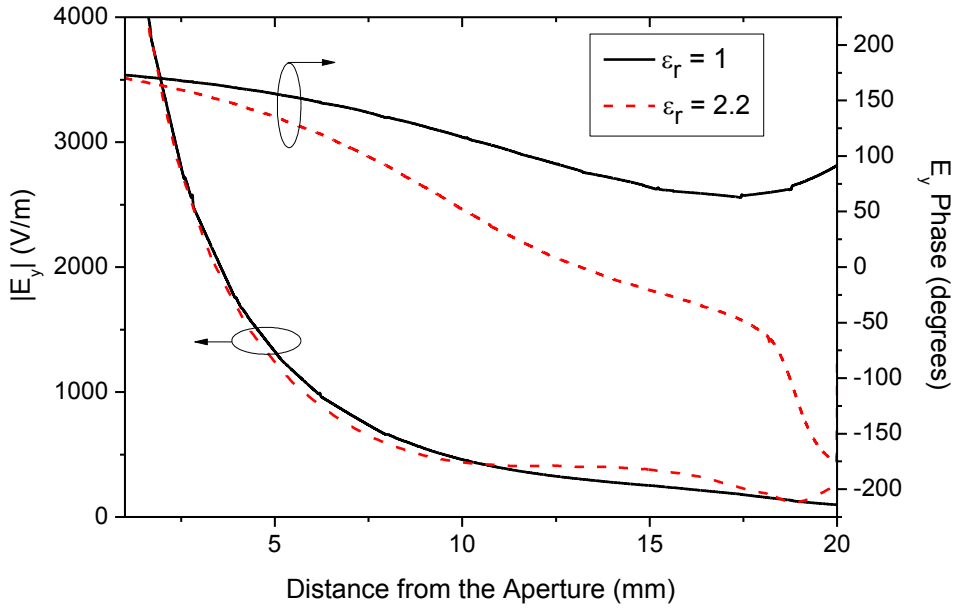

Figure 5.7: Electric field away from the aperture for ε_r = 1 and 2.2.

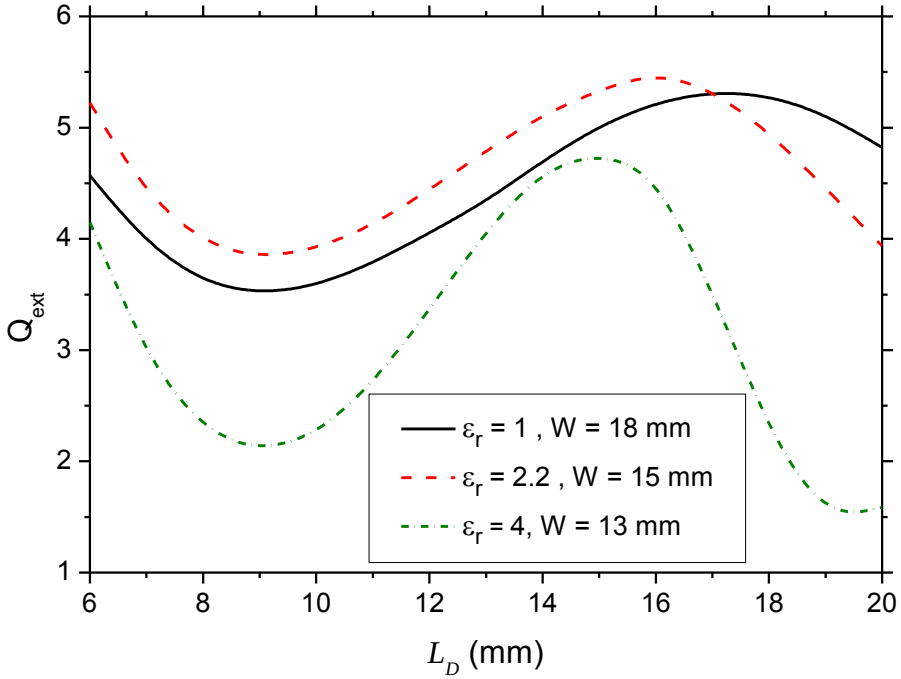

Figure 5.8: Variation of Q_{ext} of the resonator/antenna in Fig. 5.3(a) versus L_D for ε_r = 1, 2.2, and 4. The substrate thickness h = 3.17 mm.

5.2.2 Resonator/Antenna Radiation Characteristics

Using field equivalence principles, and for the purpose of studying radiation patterns, the resonator/antenna in Fig. 5.3(a) can be treated as a lineal magnetic current for a thin substrate. In this case, the radiation resembles that of a horizontal magnetic dipole on top of an infinite ground plane. An air-filled resonator/antenna is considered first to study the resonator/antenna radiation in isolation of surface waves. Fig. 5.9 compares the E-plane radiation patterns of the air-filled resonator/antenna for two different substrate thicknesses over an infinite ground plane. It is seen that although the direction of the maximum radiation is towards end fire, the radiation pattern is broad and significant radiation towards boresight is identified. For thinner substrates, the radiation pattern becomes uniform in the upper half sphere which resembles that of a horizontal magnetic dipole over a ground plane. The resonator/antenna radiation pattern is greatly affected by the finite size of ground plane, which needs to be considered in the design. As pointed out in [34] for cavity backed slot antennas, due to the fact that the radiation along the aperture is small, the diffraction in the H plane is slight and the radiation pattern is very weakly dependent on the dimension W_G of the ground plane. The E-plane pattern, on the other hand, is considerably dependent on the dimensions L_D and L_G as the diffraction effect at the ground plane edges is more pronounced in this plane. The diffracted waves interfere with the direct radiation from the aperture causing a possible distortion of the radiation pattern. Fig. 5.10 shows simulated radiation patterns for different ground plane sizes in which the aperture is symmetrically located on the ground plane ($L_D = L_G$). It is noted that the direction of the maximum radiation is close to boresight for small ground plane sizes, and starts to tilt away from boresight for larger ground planes, before the pattern deteriorates due to destructive interference with diffracted waves.

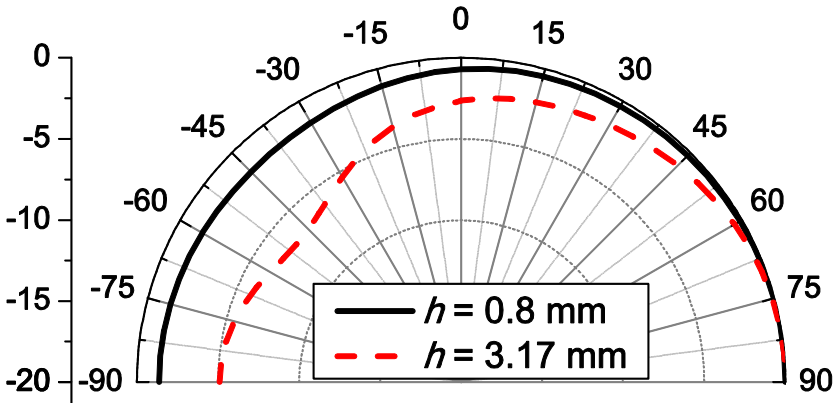

Figure 5.9: Simulated E-plane radiation patterns of an air-filled resonator/antenna over an infinite ground plane for two different substrate thicknesses.

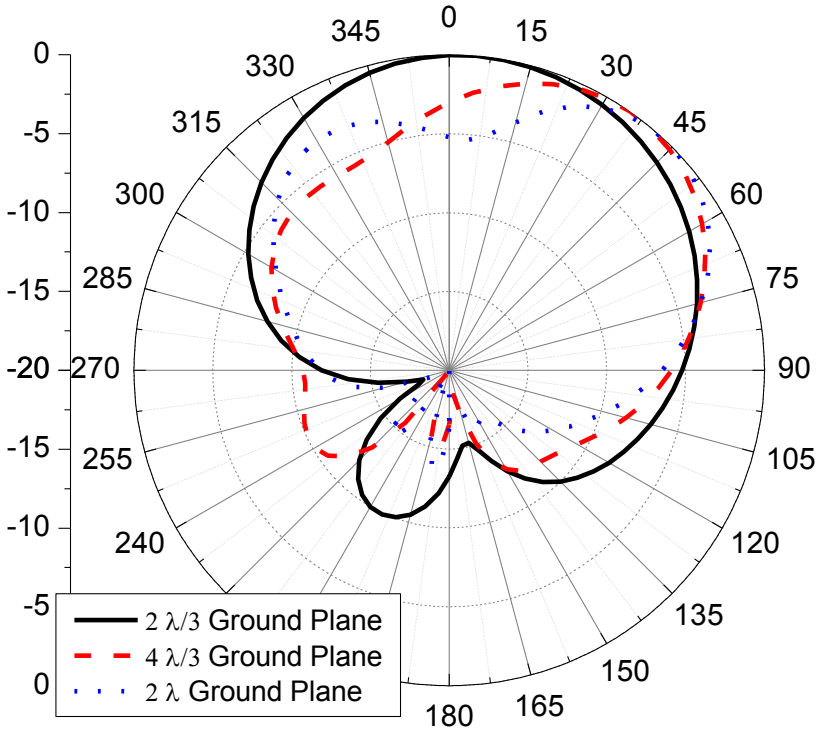

Figure 5.10: Simulated E-plane radiation patterns of an air-filled resonator/antenna over finite ground planes of different lengths L_D. (W = 18 mm, h = 3.17 mm)

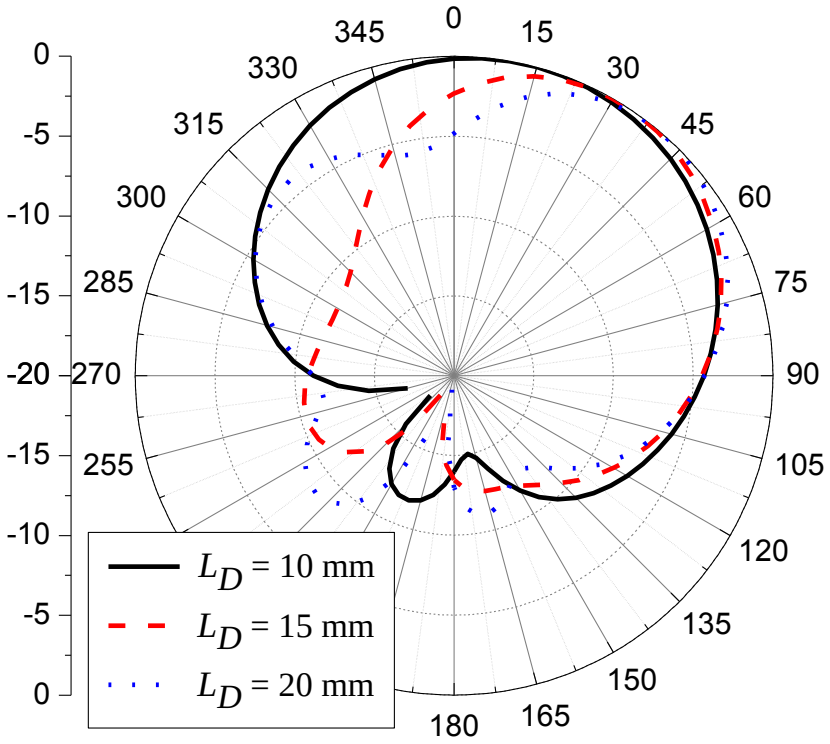

Figure 5.11: Simulated E-plane radiation patterns of a dielectrically-filled resonator/antenna for different L_D. (ε_r = 2.2, W = 15 mm, h = 3.17 mm)

Similar behavior is also found for dielectrically-filled resonator/antennas. The dimension L_D changes the relative phase between the direct aperture radiation, the surface wave radiation, and the diffracted waves. The superposition of those three components determines the total radiation pattern. The E-plane pattern of the resonator antenna with ε_r = 2.2 for different L_D and a fixed L_G = 10 mm is shown in Fig. 5.11. Similar to the air-filled resonator/antenna, the radiation is close to boresight for small L_D, and tilts away for larger L_D, before the pattern is eventually distorted as the surface wave radiation and direct aperture radiation start to interfere destructively at boresight. As might be expected, the value of L_D, at which considerable radiation pattern distortion is observed, decreases with increased dielectric constant. Due to the same reason, for any given design, the radiation pattern tilt away from boresight tends to increase at higher frequencies.

5.2.3 Filter/Antenna Design.

In section 5.2.1, the resonator/antenna is shown to behave as an *RLC* circuit and the equivalent circuit of the entire filter/antenna is presented in Fig. 5.5. With the aid of the equivalent circuit, the filter/antenna system is designed using the same approach described in Chapter 3. In order to demonstrate the possibility of wideband filter/antenna integration, a 34% FBW three-pole Chebyshev filter/antenna is designed at 10.2 GHz on 3.17-mm-thick Rogers RT/Duroid 5880 (ε_r = 2.2 and tanδ = 0.0009). The design parameters are:

$$k_{12} = k_{23} = 0.21 \tag{5.1}$$

$$Q_{ext,1} = Q_{ext,2} = 4.4 \tag{5.2}$$

To obtain a Q_{ext} of 4.4, W is chosen as 15 mm using Fig. 5.6(b). The dimensions of the designed filter/antenna are listed in Fig. 5.2. Shielding metallic caps are used to cover the CPW lines at the input port to eliminate any radiation from the lines. Fig. 5.12 shows the responses of the structure simulated using HFSS. The reflection coefficient is less than -15 dB within the passband. The gain at boresight versus frequency, plotted in the same figure, demonstrates the filtering function of the filter/antenna and is very flat in the pass band. The gain at 9, 10.2, 11 GHz is 5.1, 4.9 and 4.7 dBi, respectively. The radiation patterns of the filter/antenna at the three frequencies are shown to relatively stable over frequency as illustrated in Fig. 5.13. The pattern slightly tilts more towards the endfire direction at higher frequencies for the aforementioned reason. L_D = 10 mm is chosen for this design.

The directivity at boresight is simulated to be 5.1 dBi at 10.2 GHz, which implies an efficiency of 96% by taking the ratio of gain over directivity, for the entire filter/antenna system.

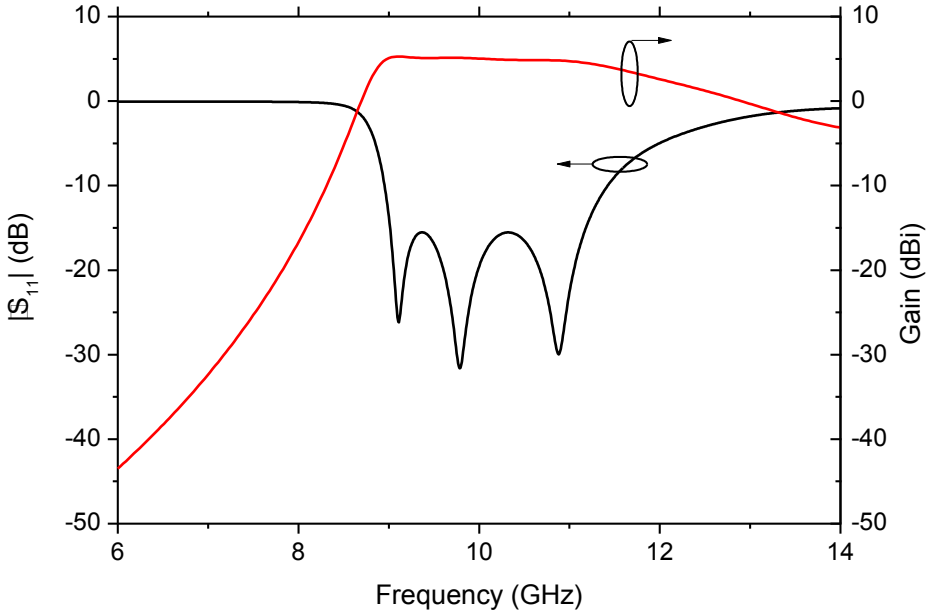

Figure 5.12: Simulated responses of a 34% three-pole integrated filter with an aperture antenna on 3.17-mm-thick Rogers RT/Duroid 5880.

It is noted that the slower out-of-band rejection at the upper band is due to the existence of the TE_{102} mode of the cavity resonators at around 16 GHz. This phenomenon is typical for wide-band cavity filters and can be improved by introducing transmission zeros at the upper band [35] or using evanescent-mode cavities [36].

The presented antenna structure in this Chapter can realize a wide range of Q_{ext}, which leads to great flexibility in designing different FBWs for integrated filter/antenna whereas the filter/antennas using slot antennas in Chapters 3 and 4 are limited to 10% FBW or less. By following the design charts in Fig. 5.6, filter/antennas with FBW of 3-34% can be realized.

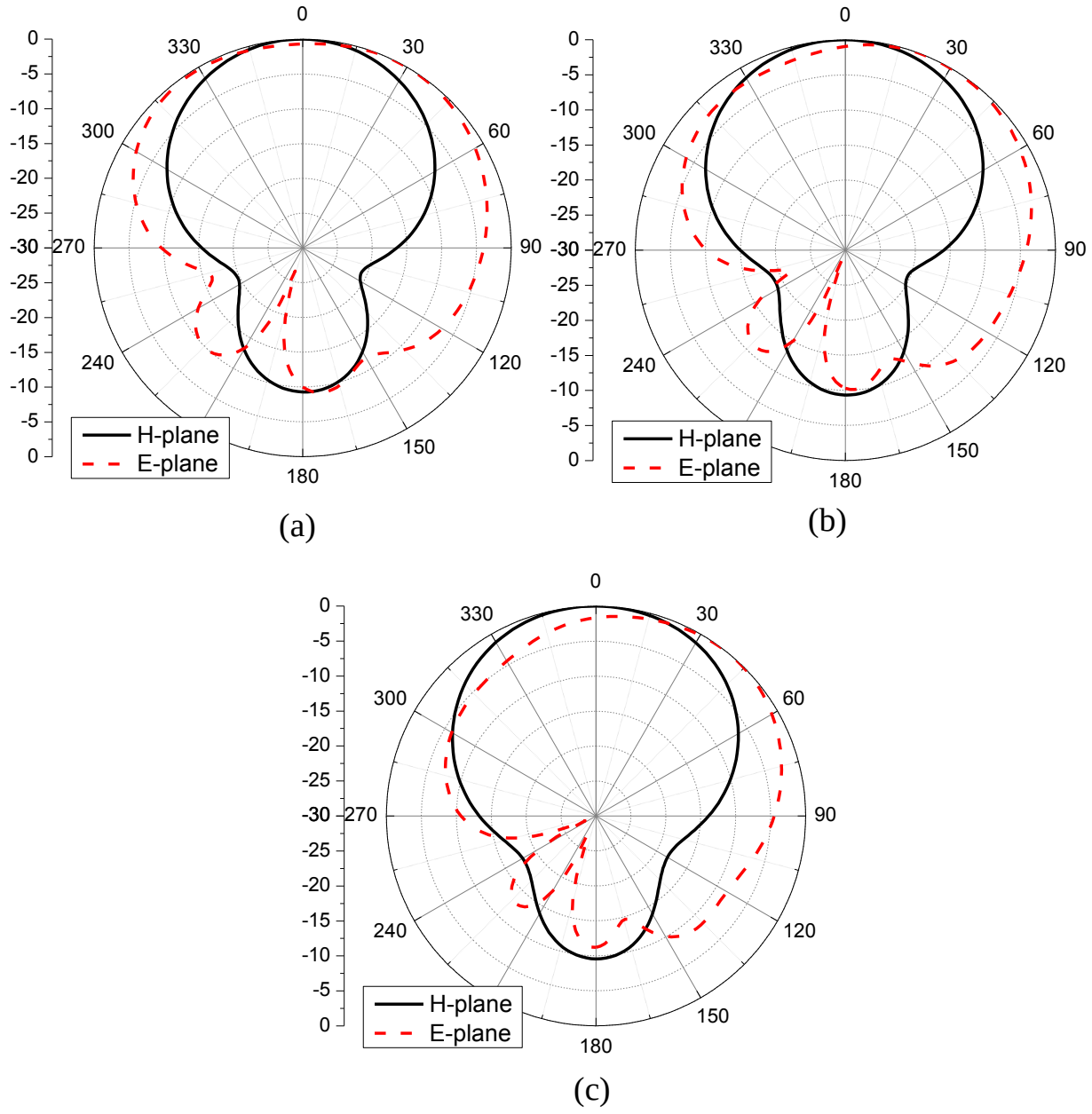

Figure 5.13: Simulated radiation patterns of the 34% integrated filter/antenna at f = (a) 9 GHz, (b) 10 GHz, and (c) 11 GHz.

To prove this new filter/antenna integration, an 8% FBW three-pole filter/antenna is designed at 10 GHz on 1.57-mm-thick Rogers RT/Duroid 5880. We choose this relatively smaller FBW since it is always more difficult to make smaller FBW filters given certain fabrication tolerances. The design parameters are:

$$k_{12} = k_{23} = 0.05 \tag{5.3}$$

$$Q_{ext,1} = Q_{ext,2} = 19.6 \tag{5.4}$$

Using Fig. 5.7(b), W = 13mm is chosen to achieve Q_{ext} of 19.6. The other dimensions of the structure are listed in Fig. 5.2. Simulation and measurement results of a fabricated prototype are compared in section 5.3.

5.3 Results and Discussion

A prototype filter integrated with an aperture antenna is fabricated and measured. Photos of the fabricated device are shown in Fig. 5.14. An SMA connector is soldered to the CPW line for measurement purposes and a shielding cap is used. The measured filter/antenna S_{11} agrees well with simulation results as shown in Fig. 5.15. The measured center frequency is 10.08 GHz, compared with 10 GHz in the simulation. This 0.8% frequency shift is due to the fabrication tolerances. Measured return losses higher than 13 dB are observed within the passband. To verify the filtering function of this integrated system, the gain of the filter/antenna system versus frequency is measured and plotted against the simulation results as shown in Fig. 5.15. The measured filter/antenna bandwidth of 8.3% is slightly larger than the simulated 8.0%. The measured gain at the center frequency is 5.7 dBi which matches the simulated gain.

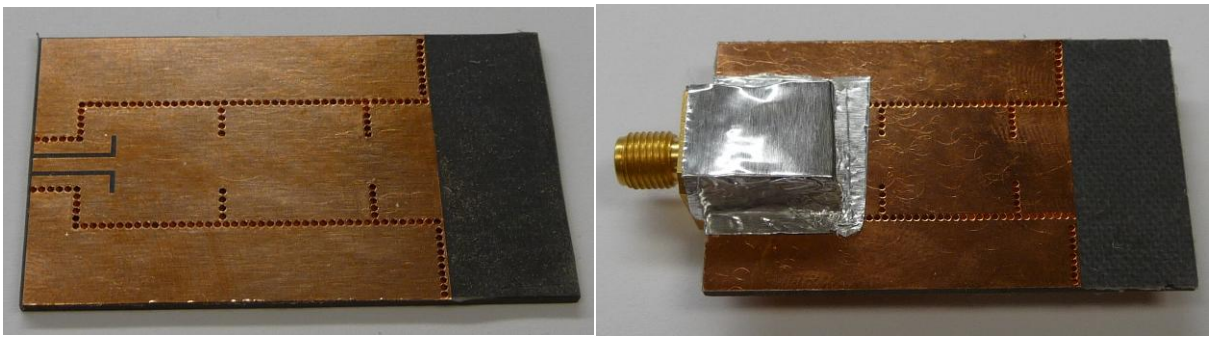

(a) (b)

Figure 5.14: Photos of the fabricated filter/antenna. (a) With and (b) without the shielding cap.

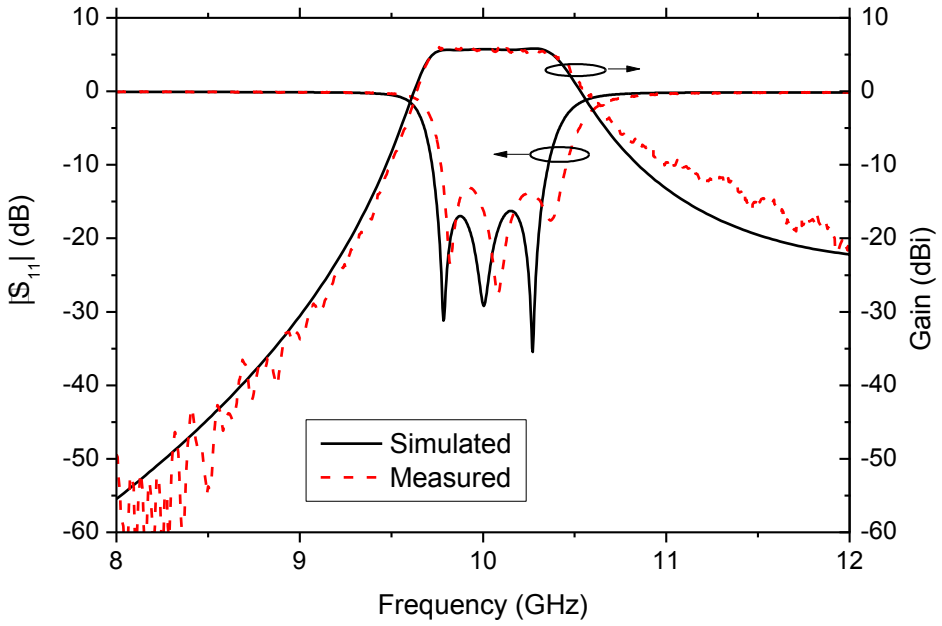

Figure 5.15: Simulated and measured responses of the three-pole integrated filter with an aperture antenna at 8-12 GHz.

Using the simulated directivity of 6.1 dBi, the overall efficiency of the integrated filter/antenna system is found to be 91%, which is lower than that of the 34% FBW filter/antenna due to the reduced FBW. Fig. 5.16 shows the measured wide-band responses of the filter/antenna up to 18 GHz, in which the spurious response due to the TE_{102} mode of the cavity resonators can be seen.

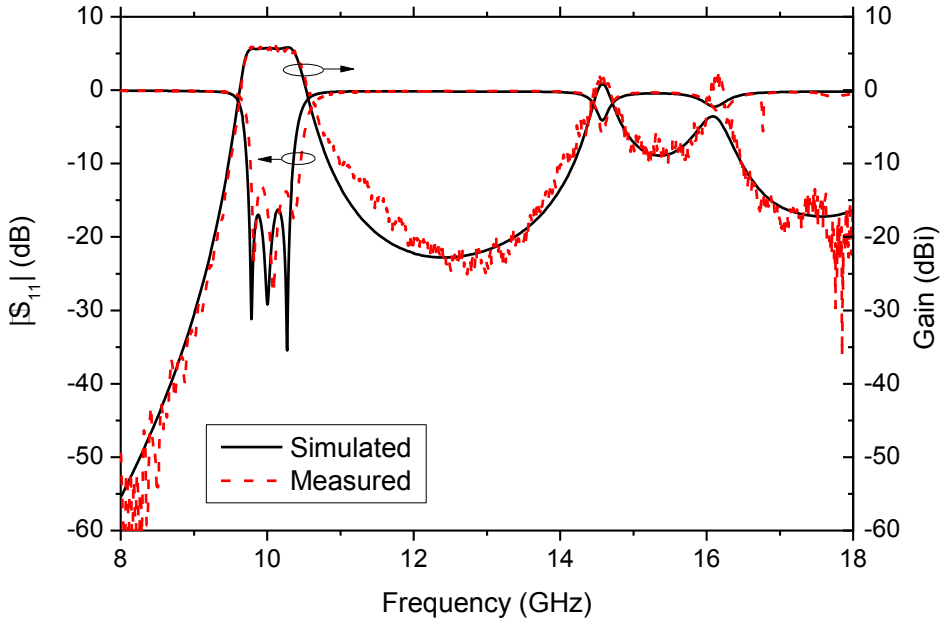

Figure 5.16: Simulated and measured responses of the three-pole integrated filter with an aperture antenna at 8-18 GHz.

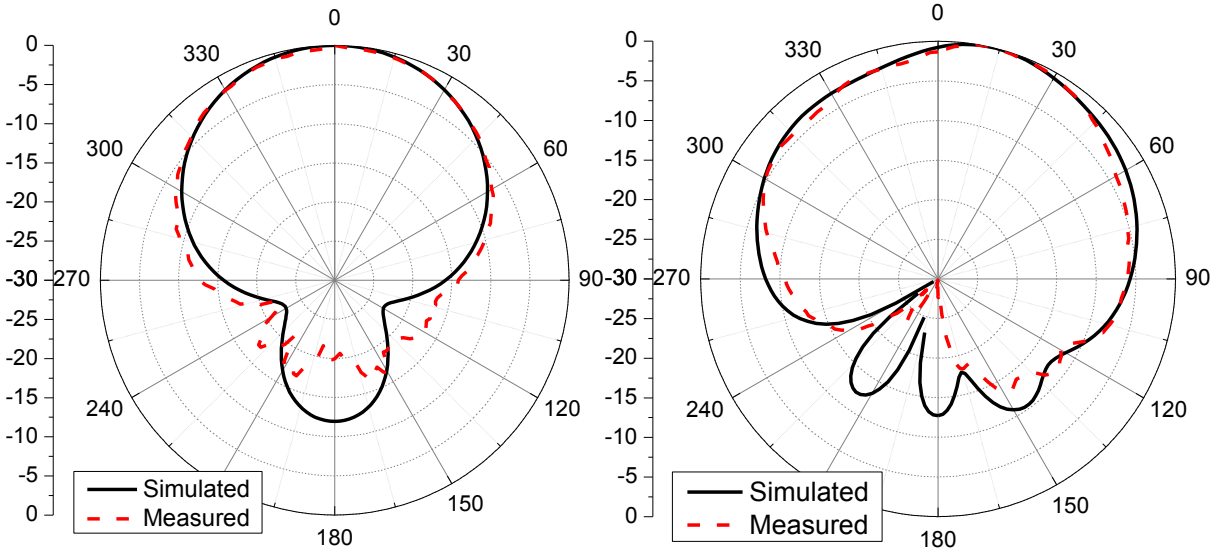

Figure 5.17: Simulated and measured radiation patterns of the 8% integrated filter with an aperture antenna in (a) H-plane and (b) E-plane at the center frequency.

The measured radiation patterns agree very well with the simulation results in both E- and H-planes at the center frequency as shown in Fig. 5.17. The radiation pattern squint with frequency is found very small over the 8% FBW and similar radiation patterns are observed across the frequency passband.

5.4 Conclusion

The integration of high-Q cavity filters with aperture antennas was demonstrated through simulation, fabrication and measurements. Due to the excitation of surface waves, The Q_{ext} of the filter/antenna can be significantly reduced, which allows for the design filter/antenna systems with FBW up to 34%. The radiation characteristics of the antenna and the means to create broadside radiation patterns are discussed. A 34% FBW integrated three-pole filter/antenna system is designed to demonstrate the possibility of wideband filter/antenna integration. A 8% FBW integrated three-pole filter/antenna system has been prototyped and shown to agree very well using the PCB fabrication techniques.

6 INTEGRATION OF FILTERS WITH MONOPOLE ANTENNAS

6.1 Introduction

In chapters 3-5, we presented a synthesis technique to integrate high-Q 3-D filters with slot and aperture antennas. By co-designing the filter and antenna into an inseparable unit, the 50-ohm transition between the otherwise separate structures is eliminated, resulting in more compact and efficient systems. In this chapter, we extend the technique to the integration of 3-D cavity filters with monopole antennas, which provide vertical polarization and omnidirectional radiation patterns. The efficiency of the entire filter/antenna system is shown to be as high as 93% at *X* band. A prototype filter/antenna is designed, fabricated, and measured. Excellent agreement between measured and simulated results is observed. The integration approach presented herein can be used for other types of wire antennas depending on the application.

6.2 Filter/Antenna Synthesis

The schematic of a three-pole Chebyshev bandpass cavity filter integrated with a monopole antenna is shown in Fig. 6.1. The cavities are realized using closely-spaced metallic vias, and the internal coupling between cavities is through irises in the common sidewalls. The external coupling to the first cavity is from a short-ended SMA connector. A monopole antenna is electrically connected to the bottom side of the third cavity through a circular opening on its top side. Due to its relatively wide bandwidth, the monopole antenna can be designed to act as an equivalent load mimicking the effect of a port in a corresponding reference filter.

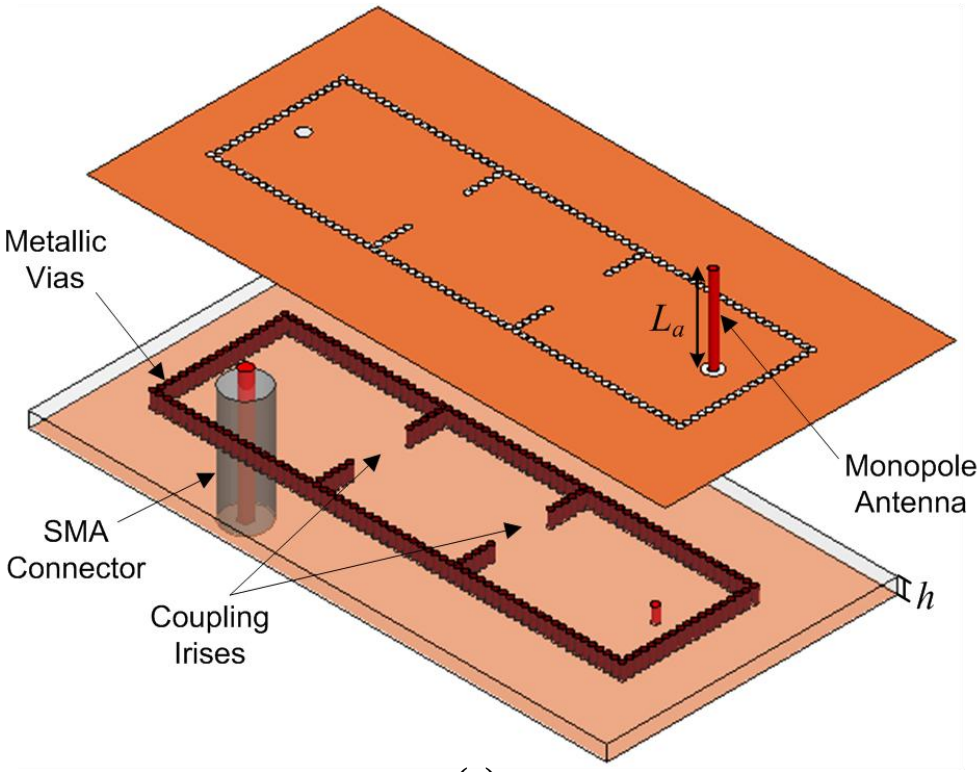

(a)

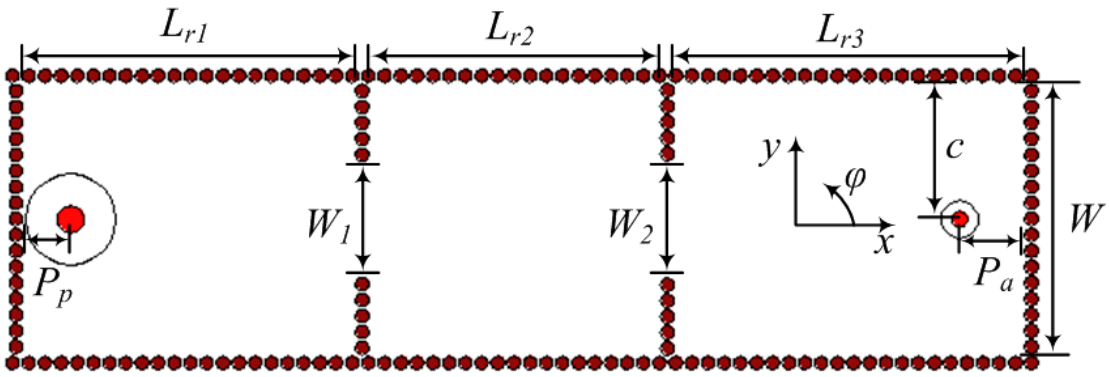

(b)

Figure 6.1: (a) Skew and (b) top view of a three-pole cavity filter integrated with a monopole antenna. (W = 13; P_p = 2.3; W_1 = 5.5; W_2 = 5.6; L_{r1} =15.5; L_{r2} = 13.6; L_{r3} = 16.5; P_a = 3.2, c = 6.5; L_a = 7; h = 1.57) Dimensions are in mm.

The response of the filter/antenna will exhibit the same filtering function if the resonant frequency of each resonator, the internal coupling coefficient k_{ij}, and the external quality factor Q_{ext} are identical to a reference filter. In this regard, the monopole antenna should provide the same external coupling level as the port of the reference filter. In addition, the frequency loading effect of the antenna, which is generally different from that of the port, should be appropriately compensated for. Section 6.2.1 presents the equivalent circuit model for this integrated monopole antenna and the design curves for Q_{ext}. The filter/antenna synthesis procedure is described in Section 6.2.2.

6.2.1 Modeling the Cavity and Monopole Antenna

We first consider a waveguide which is fed by a coaxial probe as shown in Fig. 6.2(a). This structure was studied by Harrington for thin feeding probes [37]. Its equivalent circuit is shown in Fig. 6.2(b). This equivalent circuit uses an ideal transformer with *1:n* turns ratio and a reactance of X_p from the probe. Using a stationary treatment and assuming the characteristic impedance of the waveguide $Z_o = 1\ \Omega$, the turns ratio n is given by [37]:

$$n^2 = Z_w \frac{2h}{W}\left(\frac{\tan(kh)}{kh}\right)^2 \sin^2\left(\frac{\pi c}{W}\right) \tag{6.1}$$

where h and W are the waveguide height and width, respectively; c is the distance between the center of the probe and the sidewall of the waveguide; k is the wave number in the dielectrically-loaded waveguide; and Z_w is the TE_{10} wave impedance.

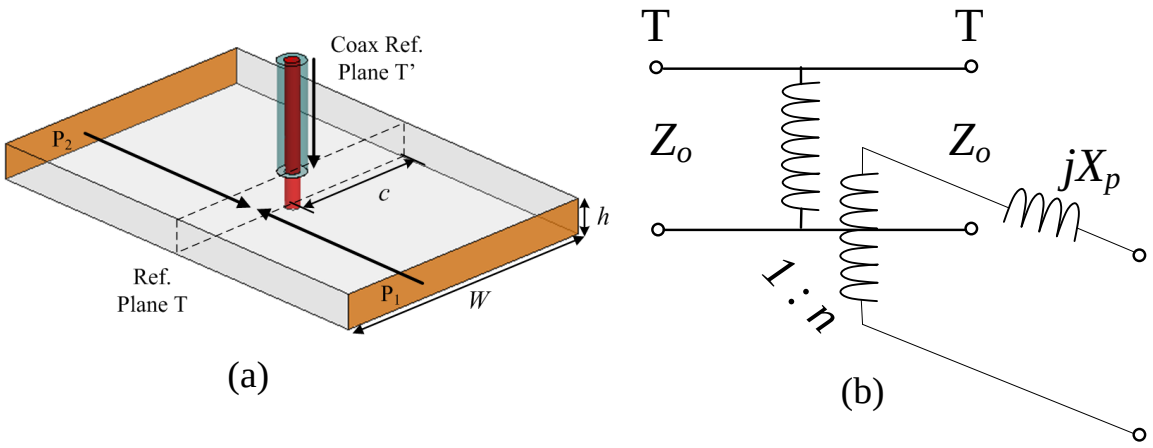

Figure 6.2: (a) Schematic of a waveguide excited by a coaxial probe and (b) its equivalent circuit. (W = 13, c = 6.5, h = 1.57) Dimensions are in mm.

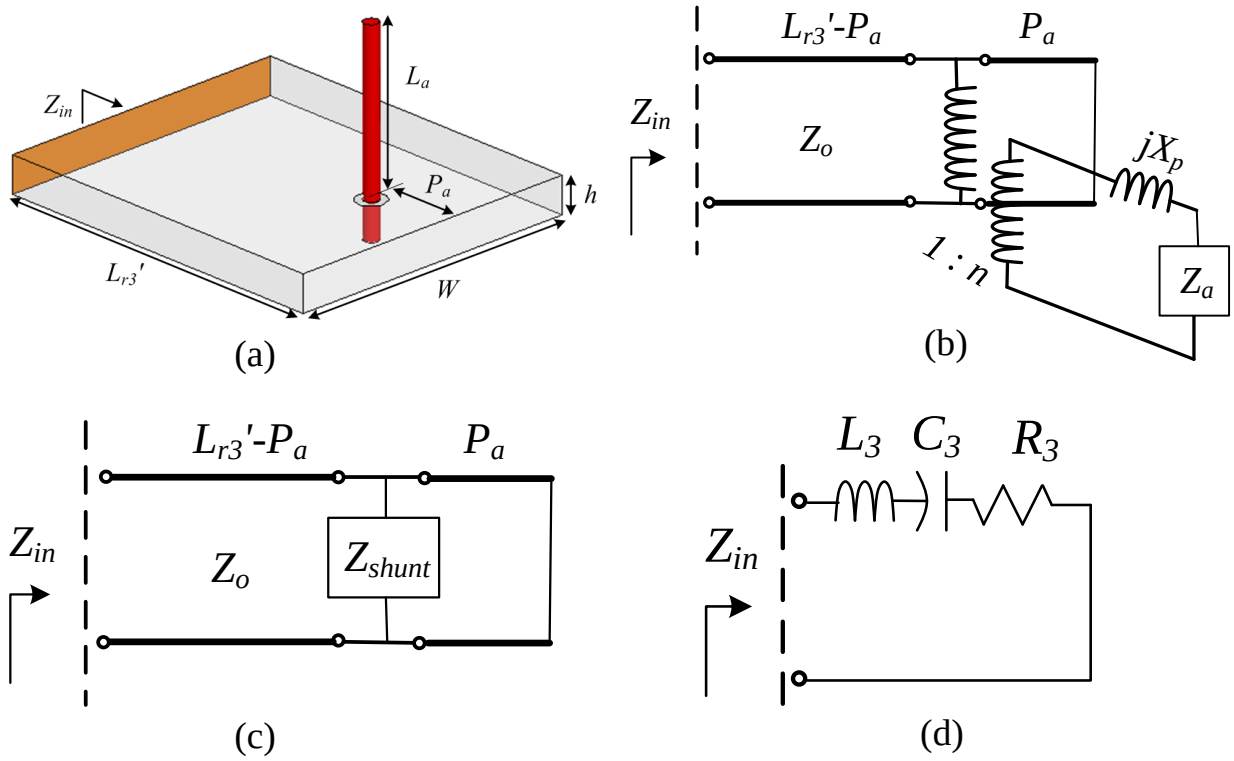

Figure 6.3: (a) Resonator/antenna structure. (b) Equivalent circuit of the resonator/antenna. (c) Simplified equivalent circuit. (c) Equivalent series *RLC* circuit.

The structure consisting of the monopole, the coupling probe, and the third cavity of the filter, referred to as the resonator/antenna is illustrated in Fig. 6.3(a). It can be obtained by connecting a monopole antenna at the reference plane *T'* of the structure in Fig. 6.2(a) and replacing one of the ports with a short-circuiting wall. The equivalent circuit of the resonator/antenna is shown in Fig. 6.3(b), in which Z_a represents the impedance of the monopole antenna. The monopole antenna coupled through the probe can be modeled as a shunt impedance Z_{shunt} as shown in Fig. 6.3(c), which is given by:

$$Z_{shunt} = \frac{1}{n^2}\left(jX_p + Z_a\right) \tag{6.2}$$

in which the turns ratio n modifies Z_{shunt} and can be used to control the coupling between the cavity resonator and monopole antenna. The freedom in choosing n is not exploited herein in order to reduce the number of design parameters.

In order to extract Z_{shunt}, the structure in Fig. 6.4 is first simulated using Ansoft High Frequency Structure Simulator (HFSS). The monopole antenna length L_a is chosen to be 7 mm and the substrate is 1.57-mm-thick Rogers RT/Duroid 5880 (ε_r = 2.2 and tanδ = 0.0009). The diameters of the probe (same as the monopole antenna) and the hole on the top of the cavity are chosen as 0.635 and 1.27 mm, respectively. Z_{shunt} can be extracted as the Z_{12} of two-port network at the reference plane T and plotted in Fig. 6.4, in which Z_o = 1 Ω is used as the characteristic impedance of the waveguide. Using the equivalent circuit in Fig. 6.3(c), the input impedance of the resonator/antenna Z_{in} is calculated and shown in Fig. 6.5. It should be noted that for any P_a value, L_{r3}' is always adjusted to achieve a resonant frequency f_o = 10 GHz.

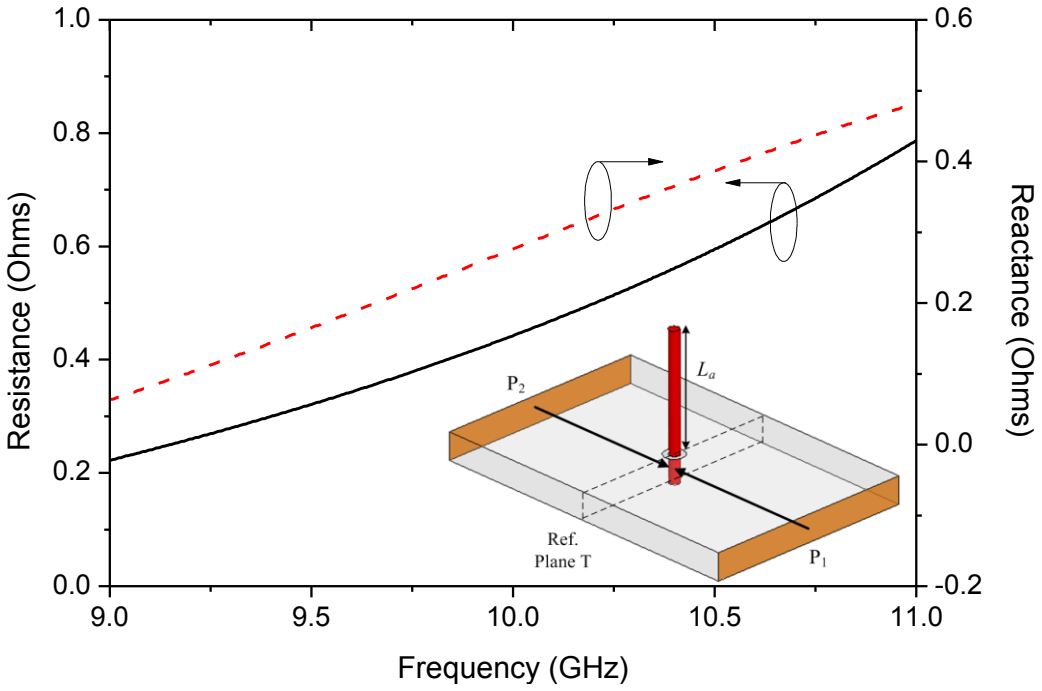

Figure 6.4: Z_{shunt} for a monopole antenna of length L_a = 7 mm.

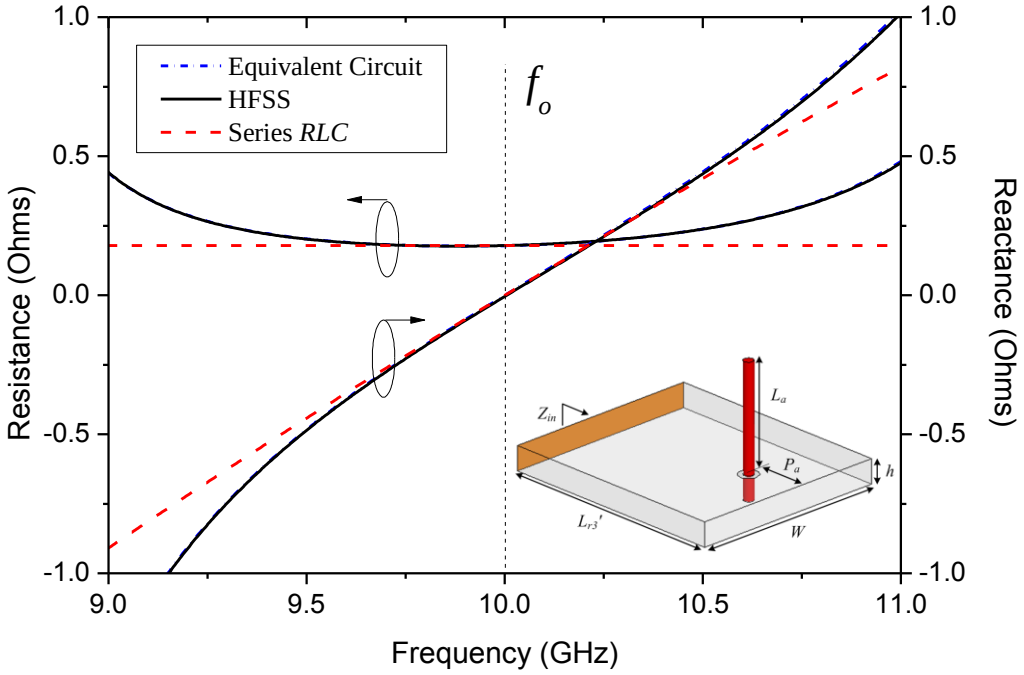

Figure 6.5: Input impedance of the cavity resonator with a monopole antenna.

It is apparent from Fig. 6.5 that the structure behaves like a series *RLC* resonator (Fig. 6.4(d)) around the resonant frequency. Particularly, P_a and L_{r3}' values used to generate Fig. 6.5 are 3.2 and 17.8 mm, respectively.

To verify the accuracy of the equivalent circuit in Fig. 6.3(c), the resonator/antenna structure is also simulated in HFSS, which produces almost identical curves as the equivalent circuit. The element values of the series *RLC* resonator are extracted using:

$$L_3 = \frac{1}{4\pi} \frac{d(\mathrm{Im}(Z_{in}))}{df}\Big|_{f=f_0} \tag{6.3}$$

$$C_3 = \frac{1}{(2\pi f_0)^2 L_a} \tag{6.4}$$

$$R_3 = Z_{in}(f_0) \tag{6.5}$$

R_3 can be divided into two parts, namely R_{ext} and R_{o3}, that represent the radiation loss and the combined dielectric and metallic losses, respectively. By simulating the structure (Fig. 6.3(a)) with/without setting the dielectric and metallic losses to zero, R_{ext} and R_{o3} can be extracted. Q_{ext}, which corresponds to the coupling between the resonator and antenna, can then be calculated using:

$$Q_{ext} = \frac{2\pi f_0 L_3}{R_{ext}} \tag{6.6}$$

The design curves for Q_{ext} corresponding to different combinations of P_a and L_a are presented in Fig. 6.6. The close agreement between HFSS simulations and equivalent circuit model is apparent.

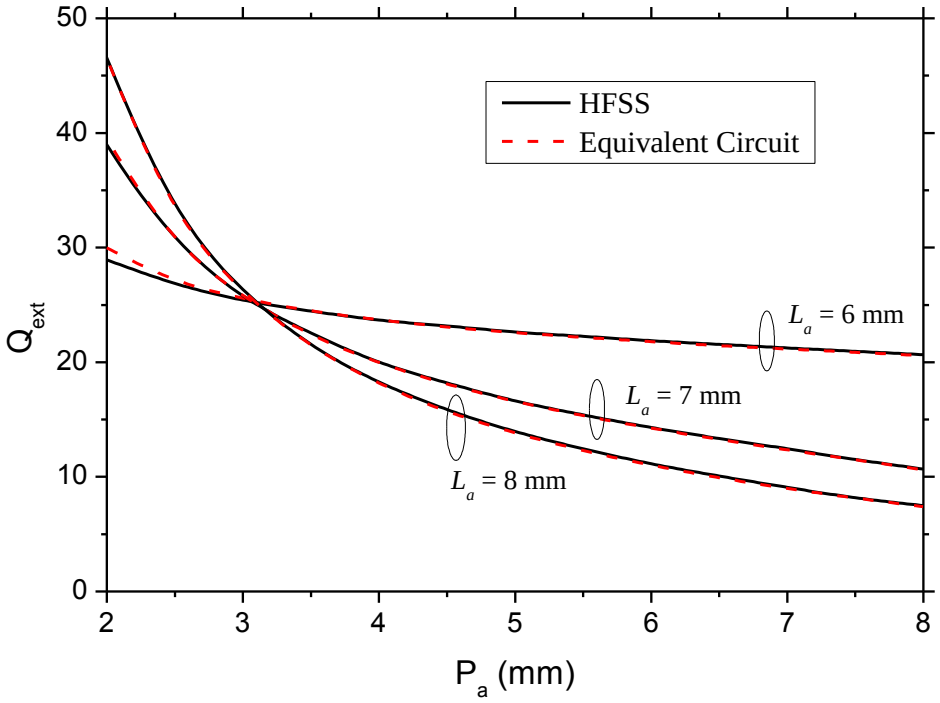

Figure 6.6: Extracted Q_{ext} versus monopole antenna position P_a for antenna lengths L_a = 6, 7, and 8 mm.

To reduce the design time, only several simulations with a parameter sweep on L_a are necessary in HFSS. Then, the extracted Z_{shunt} is employed in the equivalent circuit (Fig. 6.3(c)) to generate these design curves. From Fig. 6.9, it is observed that there are many different L_a/P_a combinations which could be used to achieve a certain Q_{ext}.

6.2.2 Filter/Antenna Design

A 7.2% FBW three-pole Chebyshev filter/antenna is designed at 10 GHz on a 1.57-mm-thick Rogers RT/Duroid 5880 substrate. The design parameters are:

$$k_{12} = k_{23} = 0.046 \tag{6.7}$$

$$Q_{ext,1} = Q_{ext,2} = 24.1 \tag{6.8}$$

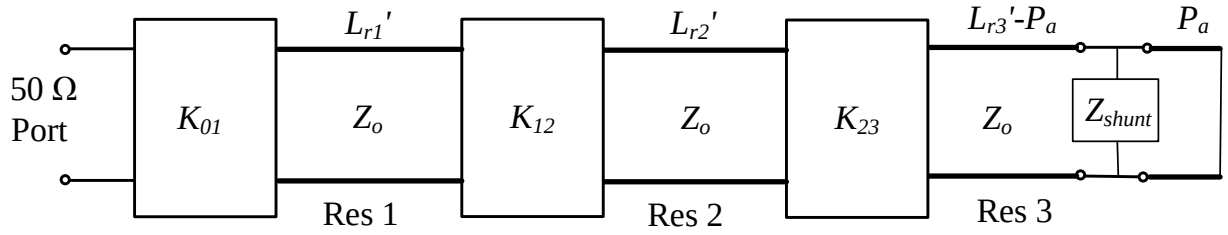

Figure 6.7: Equivalent circuit of the three-pole integrated filter/antenna system (K_{01} = 2.87 Ω, K_{12} = 0.182 Ω, K_{23} = 0.19 Ω, L_{r1}' = L_{r2}' = 16.1, P_a = 3.2, L_{r3}' = 17.8). Dimensions are in mm.

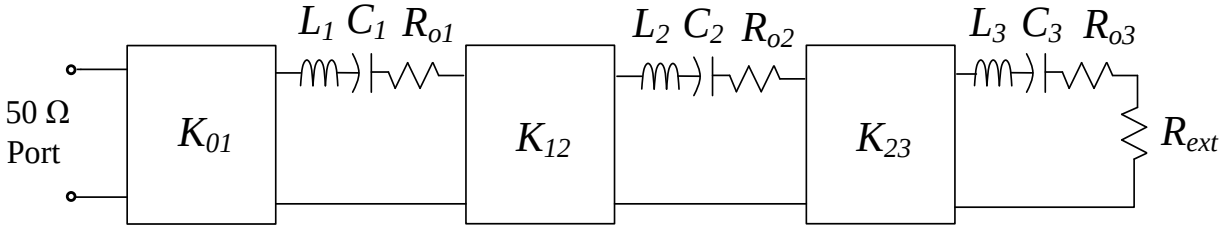

Figure 6.8: Lumped element equivalent circuit of the filter/antenna. (K_{01} = 2.87 Ω; K_{12} = 0.182 Ω; K_{23} = 0.19 Ω; L_1 = L_2 = 63.2 pH; C_1 = C_2 = 4 pF; R_{o1} = R_{o2} = 5.67 mΩ; L_3 = 69 pH; C_3 = 3.67 pF; R_{o3} = 6.2 mΩ; R_{ext} = 0.178 Ω.

Using Fig. 6.6, L_a and P_a are chosen to be 7 and 3.2 mm respectively, in order to obtain Q_{ext} = 24.1. Again, it is noted that this choice of L_a/P_a combination represents only one possible design. L_{r3}' is set to 17.8 mm to make the resonator/antenna resonate at f_o = 10 GHz. At this stage, L_3, C_3, R_{o3}, and R_{ext} can be found using (6.3)-(6.5).

Using the equivalent circuit of the resonator/antenna in Fig. 6.3(c), the equivalent circuit of the entire filter/antenna system can be constructed as shown in Fig. 6.7. *K* inverters are used to represent the external coupling from the input port to the first resonator (K_{01}) and the internal coupling between the cavity resonators (K_{12} and K_{23}). The cavity resonators are modeled by λ_g/2 transmission lines at 10 GHz with length L_{r1}' and L_{r2}'. The equivalent circuit of the filter/antenna can also be represented using lumped elements as shown in Fig. 6.8. The purpose of developing the lumped element equivalent circuit is to derive the *K* inverter values. L_1 and L_2 are obtained by

equating the slope of the reactance a $\lambda_g/2$ transmission line resonator to that of a series *LC* circuit at the resonant frequency f_o = 10 GHz. L_1 and L_2 are given by:

$$L_1 = L_2 = Z_o \frac{\pi^2 \varepsilon_r f_o}{c_0^2 \beta^2} \tag{6.9}$$

where c_0 is the speed of light in free space and β is the propagation constant of the waveguide evaluated at f_o. The coupling coefficient between resonators *i* and *j* is given by [16]:

$$k_{ij} = \frac{K_{ij}}{2\pi f_0 \sqrt{L_i L_j}} \tag{6.10}$$

Since L_3 calculated from (6.3) is generally different from L_1 and L_2, an impedance inverter K_{23} different from K_{12} is needed to obtain $k_{12} = k_{23} = 0.046$. The filter/antenna system with the design parameters shown in (6.7) and (6.8) is synthesized, using the equivalent circuit in Fig. 6.8, in which the obtained circuit parameters are listed. The resistances R_{o1}, R_{o2}, and R_{o3} account for the unloaded Q factor of the cavity resonators which is approximately 700.

Using the approach in [17], P_p, W_1 and W_2 needed to realize the impedance inverters K_{01}, K_{12}, and K_{23} are determined. The physical lengths of the resonators L_{r1} and L_{r2} are obtained by adjusting L_{r1}' and L_{r2}' to account for the negative transmission line lengths of the impedance inverters. The dimensions of the designed filter/antenna are listed in Fig. 6.1(b). The monopole antenna is mounted on a 100 × 100 mm^2 ground plane. The simulated return loss and gain of the filter/antenna using HFSS are presented in Fig. 6.9. S_{11} is less than -12 dB within the passband. It should be noted that this S_{11} level can be further reduced by designing a smaller Q_{ext}. The gain versus frequency in the azimuth plane at $\varphi = 90^o$ clearly demonstrates the filtering function of the filter/antenna. Similar curves are found at all other radiation directions. The simulated maximum

gain and directivity, which occur at 64^o zenith angle, are 4.1 and 4.42 dBi, respectively, implying 93% efficiency by taking the ratio of the two.

6.3 Results and Discussion

A prototype integrated filter/antenna is fabricated and measured. The measured S_{11} agrees well with simulation results as shown in Fig. 6.9. The 0.7% upshift in frequency is due to fabrication tolerances. The measured filter/antenna bandwidth of 6.5% is slightly smaller than the simulated 7.2%. The gain of the filter/antenna system versus frequency is measured in an anechoic chamber and is plotted against the simulation results as shown in Fig. 6.9. It is noted that the gain is measured in the azimuth plane at $\varphi = 90^o$ to directly compare with simulations. At 10 GHz, The measured gain is shown to -0.58 dBi which is close to the simulated gain of -0.35 dBi. The wideband responses are shown in Fig. 6.10.

The measured and simulated radiation patterns in both H plane and E plane ($\varphi = 90^o$) at the center frequency are shown in Fig. 6.11. The small discrepancy between the simulated and measured radiation patterns is due to the scattering from the antenna mounting structure and cables. The small ripples in the H plane radiation pattern is caused by the finite-size ground plane.

6.4 Conclusion

A synthesis approach to integrate high-Q 3-D filters with monopole antennas was presented. The integrated filter/antennas preserve the filtering and radiating characteristics with reduced size and improved efficiency. The measurement results from the prototype verified the synthesis approach.

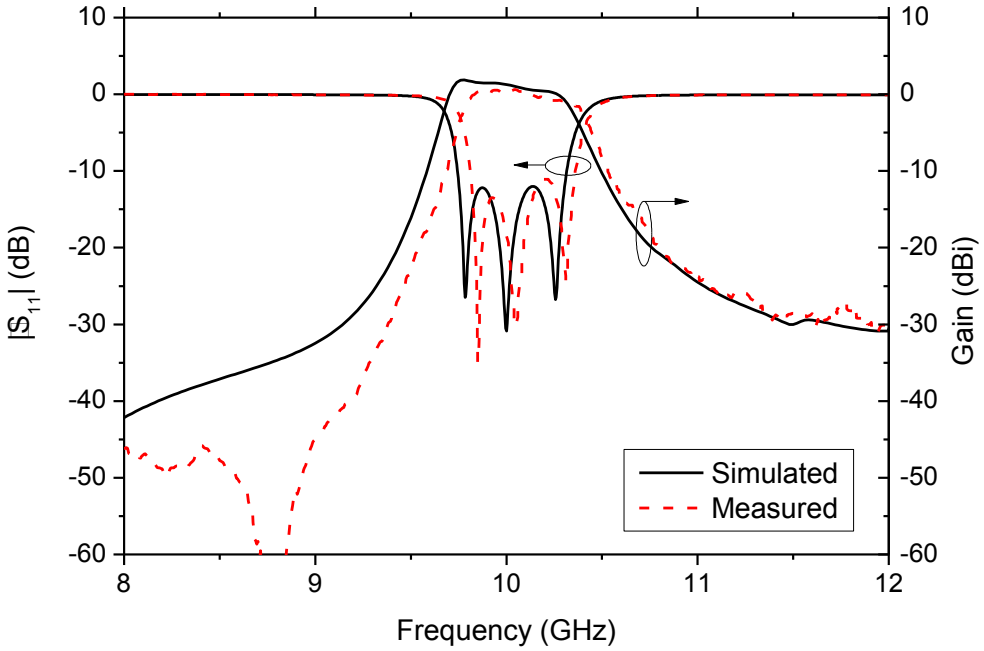

Figure 6.9: Simulated and measured responses of the three-pole integrated filter with a monopole antenna.

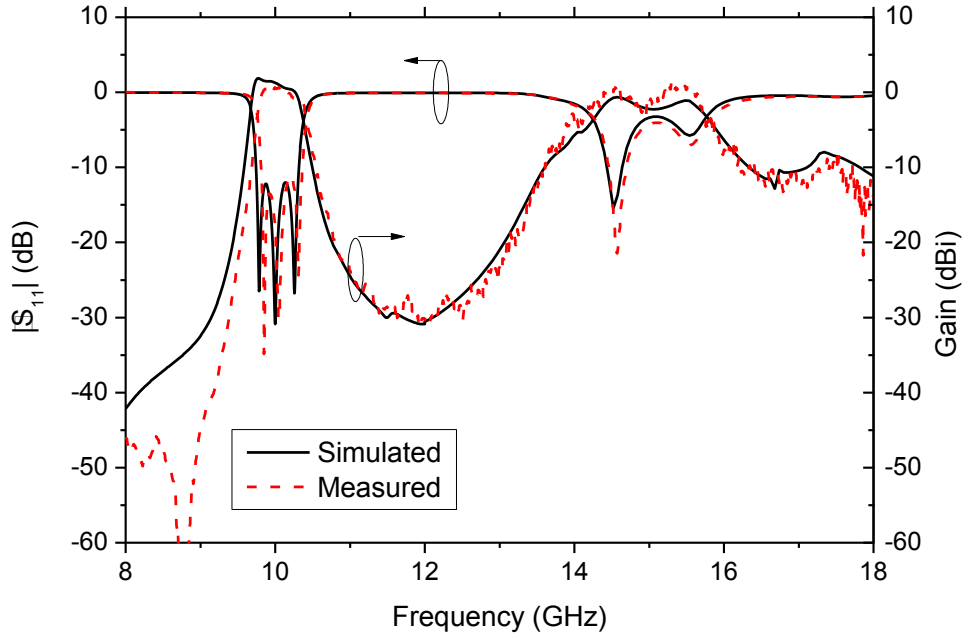

Figure 6.10: Simulated and measured wideband responses of the three-pole integrated filter with a monopole antenna.

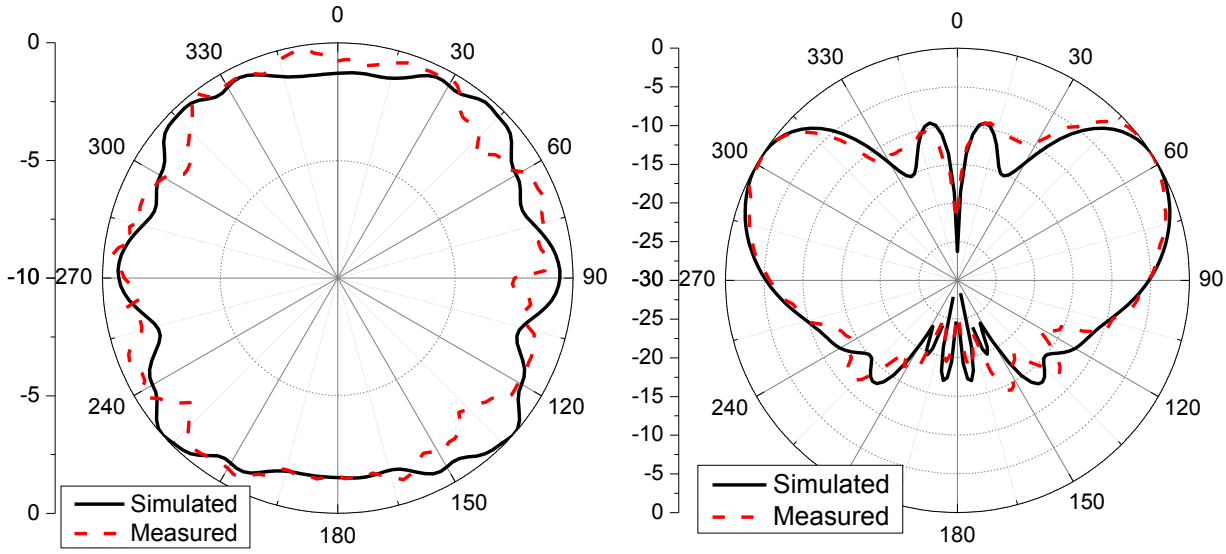

(a) (b)

Figure 6.11: Simulated and measured radiation patterns of the integrated filter with a monopole antenna in (a) H plane and (b) E plane at the center frequency.

7 INTEGRATION OF FILTERS WITH PATCH ANTENNAS

7.1 Introduction

Patch antennas have been widely used in various communications and radar systems due to ease of fabrication, low profile, and flexibility of design in terms of polarization, and radiation pattern etc. Particularly, they are very popular in phased array antenna systems since patch antenna arrays are thin, broad-side radiating, and easy to achieve beam steering capability with the help from phase shifters.

However, patch antennas are usually narrowband due to their high-Q resonant nature. Bandwidth enhancement can be achieved by utilizing thick substrates with low dielectric constants, parasitic resonant patches [38], or resonant slots within the patch antenna [39]. The increased bandwidth using these approaches is usually at the expense of losing efficiency. High-Q filters are necessary to improve the signal-to-noise ratio and consequently reduce the noise figure of the receiver for communications or radar systems. Due to the limitation of size, weight, and power (SWaP) requirements within practical systems, having high-Q filters and highly-efficient wide-band patch antennas becomes very difficult, if not impossible.

The integration of patch antennas with coplanar waveguide (CPW) and microstrip resonator filters was reported in [11-13]. The antennas acted as radiators and additional resonators simultaneously, and therefore, higher-order filtering functions were achieved with reduced number of resonators inside the filter.

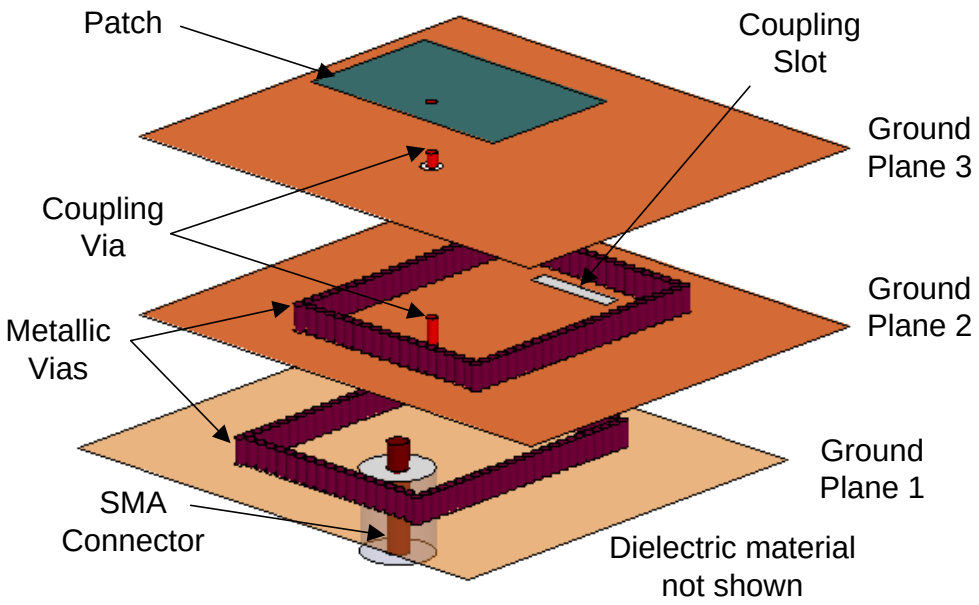

Figure 7.1: Exploded view of a vertically-integrated three-pole filter/antenna with two cavity resonators and one patch antenna.

The main disadvantage of the aforementioned integrated filter/antenna systems is the very limited Q factor performance, generally < 200, associated with the planar resonator structures used. Furthermore, radiation from the transmission line resonators can significantly degrade the out-of-band performance. Because of their better loss performance, filters with high-Q-factor resonators such as waveguide cavities [19], dielectric resonators [20], and substrate integrated waveguides (SIW) [40] are desirable over their planar counterparts.

A new way to realize integrated high-Q filters with highly-efficient patch antenna is presented in this chapter. The entire system consists of two high-Q-factor cavity resonators and one resonant patch antenna which are vertically stacked to greatly reduce the footprint as illustrated in Fig. 7.1. Similar to [11-13], the patch antenna also acts as a resonator contributing to an additional pole in the filtering response. A third-order Chebyshev filtering function is therefore realized using two cavity resonators and one patch antenna. Efficiencies as high as 91.8% have been

achieved in simulations. In addition, the bandwidth of the entire filter/antenna system exceeds that of a standalone patch antenna. A prototype of the designed filter/antenna system is fabricated and very good agreement between measured and simulated results is observed.

7.2 Filter/Antenna Synthesis

As mentioned in Chapter 2, the design of the filter/antenna systems utilizes the same design principles of microwave bandpass filters. As in the filter case, the response of the filter/antenna is determined by the resonant frequencies of the resonators, the internal coupling coefficients k_{ij} between the resonators, and the external quality factors Q_{ext} of the first and last resonators. Depending on the relative antenna bandwidth compared with the filter bandwidth, two schemes of filter/antenna integration are possible. When the antenna bandwidth is sufficiently large compared with the filter bandwidth, the antenna behaves as an equivalent load to the filter and does not contribute an additional pole in the filtering response. The integration of filters with slot, aperture, and monopole antennas presented in Chapters 3-6 fall under this category. In spite of the advantages of high efficiency and reduced size, the filter/antenna bandwidth is limited to be less than the antenna bandwidth. On the other hand, if the antenna bandwidth is comparable to or smaller than the filter bandwidth, the antenna acts as an additional resonator and adds one additional pole in the filtering response. It is found that this integration approach can be used to obtain filter/antennas with bandwidths that exceed those of standalone antennas. In this Chapter, this second category of filter/antenna integration is demonstrated with the use of patch antennas.

As shown in Fig. 7.1, three substrate layers are used to form the integrated filter/antenna structure. The dielectric material used here is Rogers RT/Duroid 5880 (ε_r = 2.2; tanδ = 0.0009; and ½ oz. copper). The cavity resonators are realized using closely-spaced metallic vias and the internal coupling between the two cavity resonators is through a slot in the common ground

plane. The coupling between the resonator and patch antenna is through a coupling via connecting them together. The external coupling to the filter/antenna is achieved by using a short-ended SMA coaxial connector. As mentioned earlier, this integrated filter/antenna exhibits three transmission poles, similar to a three-pole filter. Therefore, a rigorous synthesis procedure must be followed to ensure that the integrated filter/antenna has all the analogues of an equivalent three-pole filter in terms of resonators, internal couplings, and external couplings. The schematics of the integrated filter/antenna from different view angles are shown in Fig. 7.2.

A reference three-pole Chebyshev filter with 8% FBW at 10.16 GHz was synthesized. The design parameters of this filter are:

$$k_{12} = k_{23} = 0.054 \tag{7.1}$$

$$Q_{ext,1} = Q_{ext,2} = 17.2 \tag{7.2}$$

If this three-pole filter were realized using the vertical stacking as shown in Fig. 7.1, it would be symmetric with respect to a horizontal plane in the middle of ground planes 2 and 3. In this integrated filter/antenna design, the patch antenna replaces the top cavity resonator. k_{23} now becomes the coupling between the middle cavity and patch antenna which is achieved through a coupling via. The radiation Q factor (Q_{rad}) of the patch antenna is equivalent to $Q_{ext,2}$ of the reference filter. The rest of this section will describe the details on how to synthesize these design parameters for the integrated filter/antenna in order to realize the same filtering functions of the reference filter.

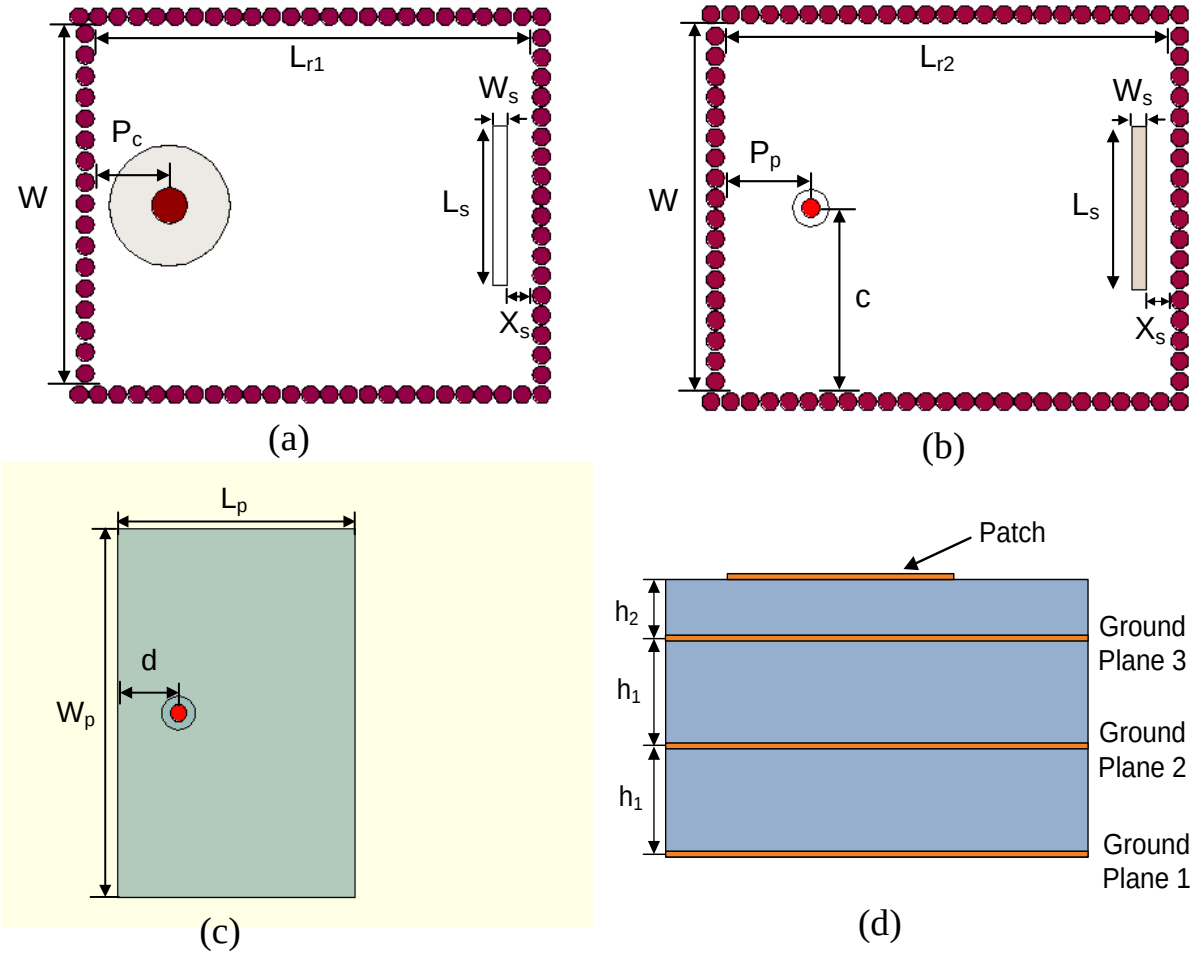

Figure 7.2: Schematics of (a) SMA coaxial feeding and coupling slot; (b) coupling slot and via; (c) coupling via and patch antenna; and (d) vertical stack. (W = 12.9; P_c = 2.7; L_s = 5.7; W_s = 0.5; X_s = 0.9; L_{r1} = 15.7; L_{r2} =16; P_p = 3.1; c = 6.5; d = 2.3; L_p = 9.1; W_p = 14; h_1 = 1.6; h_2 = 0.8) Dimensions are in mm.

It will also be shown in Section 7.3 that the integrated patch antenna exhibits the same radiating characteristics as a standalone patch antenna but with a wider frequency range of operation. This bandwidth enhancement can be explained by viewing the two cavity resonators preceding the patch antenna as a multisection impedance transformer that matches the antenna to the input port over a larger frequency range.

The most challenging part in the design is to synthesize k_{23} and the related frequency detuning effect on the middle cavity and patch antenna. There are many physical parameters which could

lead to a change in k_{23}. Therefore, it is imperative to understand the role of these parameters and provide design guidelines. In Sections 7.2.1-7.2.4, the equivalent circuit models for different sections of the filter/antenna are developed and the analytical formula of k_{23} is derived. The filter/antenna synthesis procedure is described in Section 7.2.5.

7.2.1 Modeling the Coupling Via Inside a Waveguide

In order to build the equivalent circuit for the coupling via inside the middle cavity, we first studied a waveguide which is fed by a coaxial probe as shown in Fig. 7.3(a). This coaxial probe has the same cross-sectional dimensions as the coupling via. The inner and outer diameters of the coaxial probe are 0.635 and 1.27 mm, respectively. This structure was investigated by Harrington for thin feeding vias [37]. Its equivalent circuit is shown in Fig. 7.3(b). This equivalent circuit uses an ideal transformer with $1{:}n_1$ turn ratio and a reactance of X_1 from the probe inside the waveguide. Using a stationary treatment and selecting the wave impedance Z_w as the characteristic impedance of the waveguide, the turn ratio n_1 is given by [37]:

$$n_1^2 = \frac{2h}{W}\left(\frac{\tan(kh)}{kh}\right)^2 \sin^2\left(\frac{\pi c}{W}\right) \tag{7.3}$$

where h and W are the waveguide height and width, respectively; c is the distance between the center of the probe and the sidewall of the waveguide; k is the wave number in the dielectrically-loaded waveguide. If unity characteristic impedance (Z_o =1 Ω) is preferred, n_1 is:

$$n_1^2 = Z_w \frac{2h}{W}\left(\frac{\tan(kh)}{kh}\right)^2 \sin^2\left(\frac{\pi c}{W}\right) \tag{7.4}$$

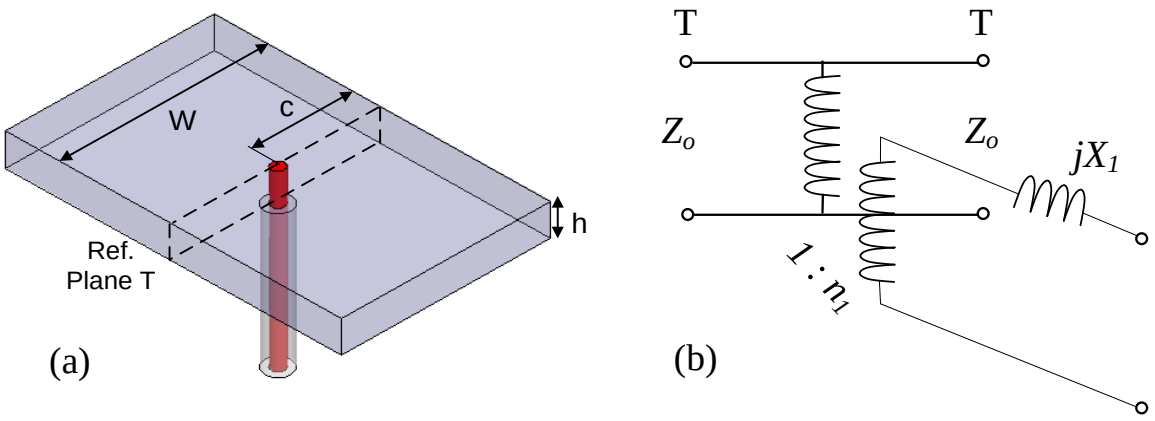

Figure 7.3: (a) Schematic of a waveguide excited by a coaxial probe and (b) its equivalent circuit.

7.2.2 Modeling the Coupling Via and the Patch Antenna

The modeling of the coupling via with the patch antenna is shown in Fig. 7.4. The reactance X_2 is from the probe (coupling via) inside the patch. The position of the probe *d* from the edge of the patch determines the turn ratio n_2 which can be calculated using [28]:

$$n_2 = \cos\left(\frac{\pi d}{L_p}\right) \tag{7.5}$$

Q_{rad} is primarily controlled by the dielectric constant and thickness of the antenna substrate [28]. Lower Q_{rad} can be obtained using thicker substrates and lower dielectric constants. In terms of the equivalent circuit parameters, Q_{rad} is given by:

$$Q_{rad} = 2\pi f_o R_r C_p \tag{7.6}$$

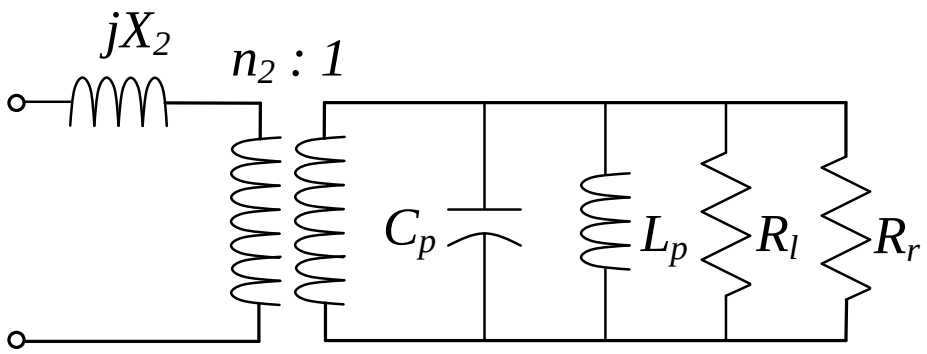

Figure 7.4: The equivalent circuit of a probe-fed patch antenna.

The parallel resistors R_r and R_l represent the radiation loss and combined dielectric and conductor losses, respectively. The quality factors due to the dielectric and metallic losses are given by [28]:

$$Q_d = 1/\tan\delta \tag{7.7}$$

$$Q_c = h\sqrt{\pi f_o \mu_o \sigma} \tag{7.8}$$

Where σ is the metal conductivity and tanδ is the loss tangent of the dielectric material. The combined quality factor Q_l due to both dielectric and conductor losses is:

$$Q_l = \frac{Q_c Q_d}{Q_c + Q_d} = 2\pi f_o R_l C_p \tag{7.9}$$

While Q_{rad} of the patch antenna is equivalent to $Q_{ext,2}$, Q_l plays the role of the unloaded quality factor of the third cavity resonator of the reference filter.

7.2.3 Filter/Antenna Modeling

With the equivalent circuits presented in the previous two subsections, the equivalent circuit of the entire filter/antenna system can be constructed as shown in Fig. 7.5. *K* inverters are used to

represent the external coupling from the SMA connector to the bottom resonator and the inter-resonator coupling between the two cavity resonators. The turn ratio n_1 and n_2 can be controlled by the probe position *c* and *d*, respectively, as illustrated in Fig. 7.2. The combined effects from the two parameters affect the coupling between the middle cavity and patch antenna k_{23}.

The impedance resulting from the short-circuited waveguide with the length P_p is equal to jX_p which is given by:

$$jX_p = jZ_o \tan(\beta P_p) \tag{7.10}$$

where β is the propagation constant of the waveguide. By reflecting the patch *RLC* circuit through the two transformers, the simplified equivalent circuit is shown in Fig. 7.6(a). The equivalent circuit element values are given by:

$$R_p' = \left(\frac{n_2}{n_1}\right)^2 R_p \,,\; L_p' = \left(\frac{n_2}{n_1}\right)^2 L_p \tag{7.11}$$

$$C_p' = \left(\frac{n_1}{n_2}\right)^2 C_p \,,\; jX_s = \frac{j(X_1 + X_2)}{n_1^2} \tag{7.12}$$

For the convenience of further analysis, the two cavity resonators are modeled by series *LC* circuits in Fig. 7.6(b). Their equivalent inductances are obtained by equating the slope of the reactance of a $\lambda/2$ short-circuited resonator to that of a series *LC* circuit at their respective resonant frequencies and found as:

$$L_1 = Z_o \frac{\sqrt{\varepsilon_r}(L_{r1}')^2}{2\pi c} \sqrt{\left(\frac{\pi}{L_{r1}'}\right)^2 + \left(\frac{\pi}{W}\right)^2} \tag{7.13}$$

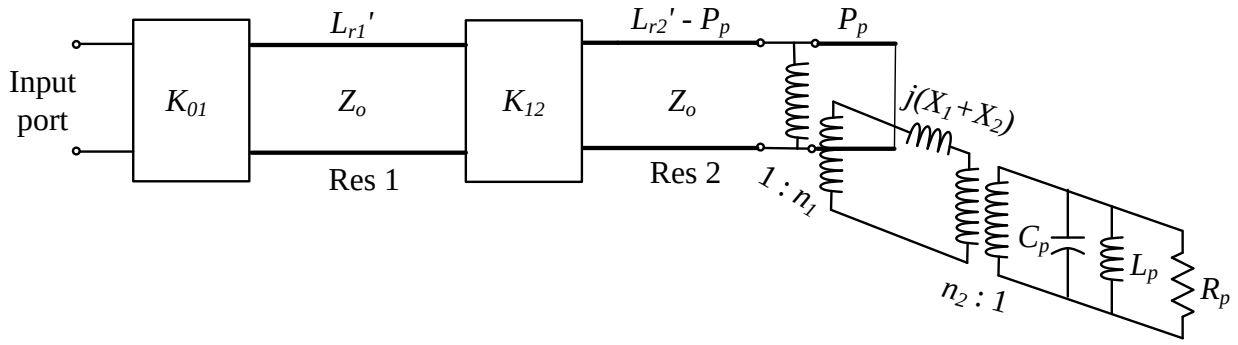

Figure 7.5: Equivalent circuit of the filter/antenna system.

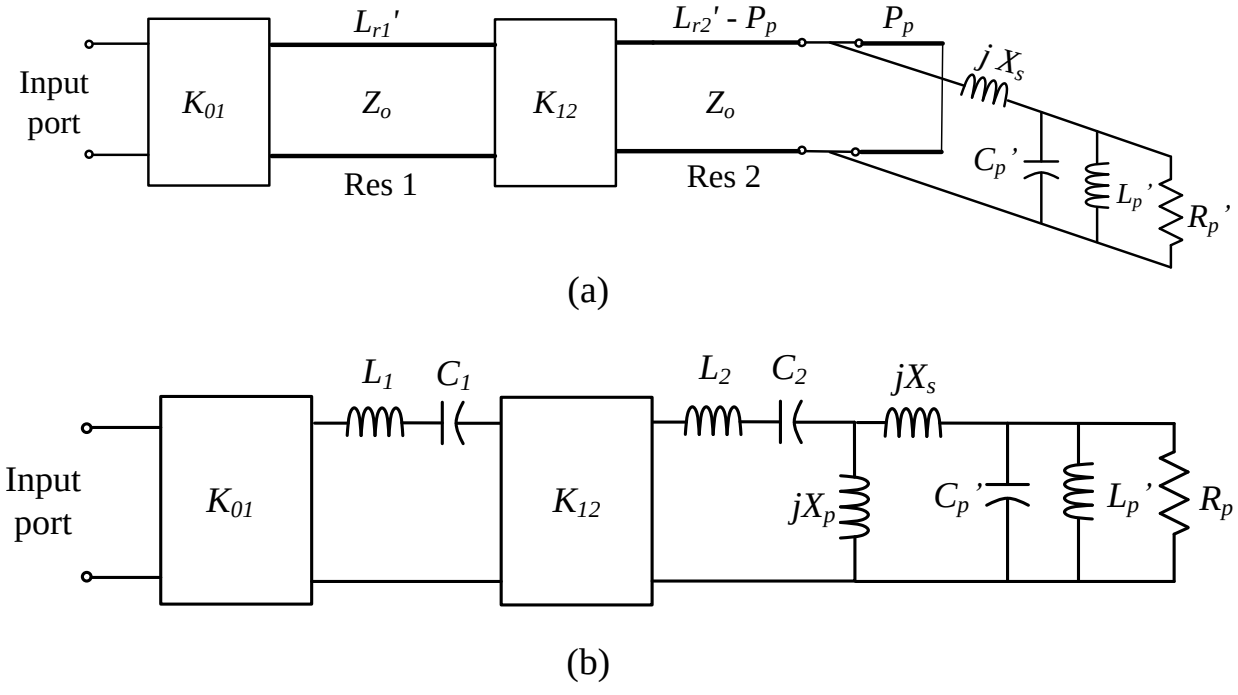

Figure 7.6: Simplified equivalent circuits of the filter/antenna system (K_{01} = 0.469 Ω, K_{12} =0.208 Ω, L_{r1}' = 15.4 mm, L_{r2}' = 16.8 mm, P_p = 2.9 mm).

$$L_2 = Z_o \frac{\sqrt{\varepsilon_r}\left(L_{r2}'-P_p\right)^2}{2\pi c}\sqrt{\left(\frac{\pi}{L_{r2}'-P_p}\right)^2+\left(\frac{\pi}{W}\right)^2} \tag{7.14}$$

7.2.4 Coupling between Patch and Middle Cavity (k_{23})

In order to see the effect of the equivalent circuit parameters and their role in determining the coupling between the middle cavity resonator and patch antenna, the circuit in Fig. 7.7 is studied where the resistance R_p' is removed. The circuit is now transformed to a more conventional form consisting of two series resonators coupled using an impedance inverter. The transformations make use of the lumped element impedance inverter models [26] shown in Fig. 7.8. The transformation steps are outlined in Fig. 7.9, and the final form is shown in Fig. 7.9(c). The patch is transformed into a series resonator circuit, the reactance of which is given by:

$$X_3(\omega) = X_s^2\left(C_p'\omega - 1/\omega L_p' - \frac{1}{X_s + X_p}\right) \tag{7.15}$$

Similarly, the reactance of the second resonator is modified by the additional term ($X_s//X_p$) and given by:

$$X_2(\omega) = \omega L_2 - 1/\omega C_2 + \frac{X_s X_p}{X_s + X_p} \tag{7.16}$$

It should be noted that L_{r2}'- P_p is slightly less than half guided wavelength at the filter/antenna center frequency. Therefore, equation (7.16) deviates from the actual value at the center frequency of the filter/antenna since the lumped circuit model in Fig. 7.6(b) closely matches a transmission line resonator of length L_{r2}'- P_p only around its resonant frequency.

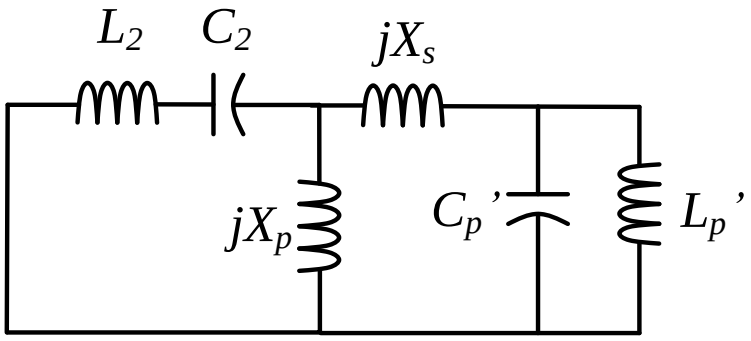

Figure 7.7: Equivalent circuit of the patch antenna coupled to the middle cavity resonator.

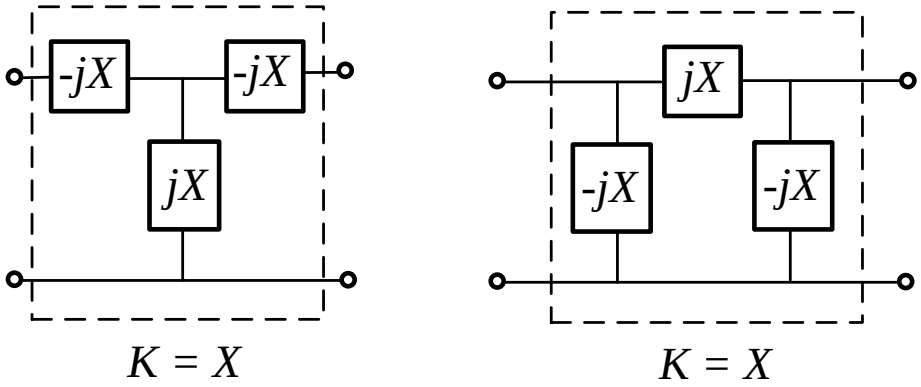

Figure 7.8: Lumped element impedance inverters.

A more accurate representation of $X_2(\omega)$ in a wider frequency range is given by:

$$X_2(\omega) = Z_o \tan(\beta(L_{r2}'-P_p)) + \frac{X_s X_p}{X_s + X_p} \tag{7.17}$$

The reactance slope parameter of series resonators is defined as [16]:

$$\alpha_i = \frac{\omega_o}{2}\frac{dX_i}{d\omega}\bigg|_{\omega_o} \tag{7.18}$$

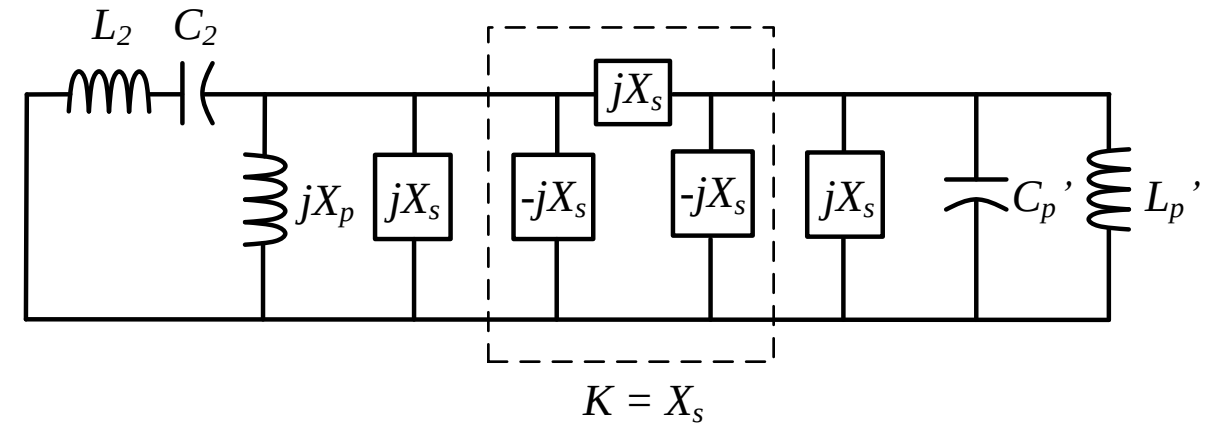

(a)

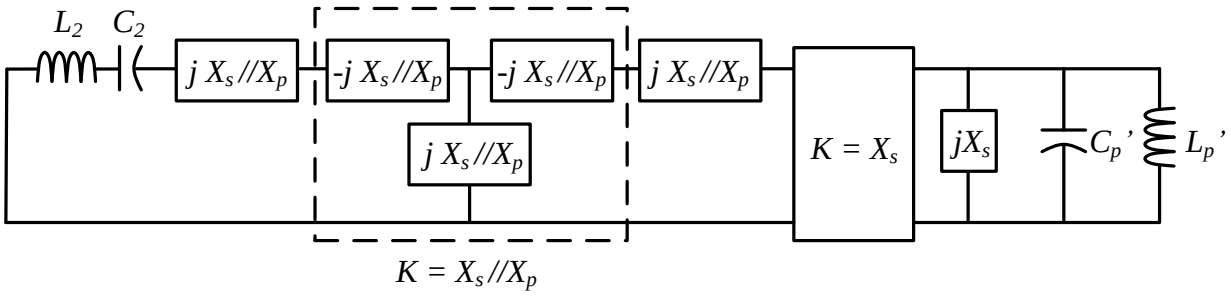

(b)

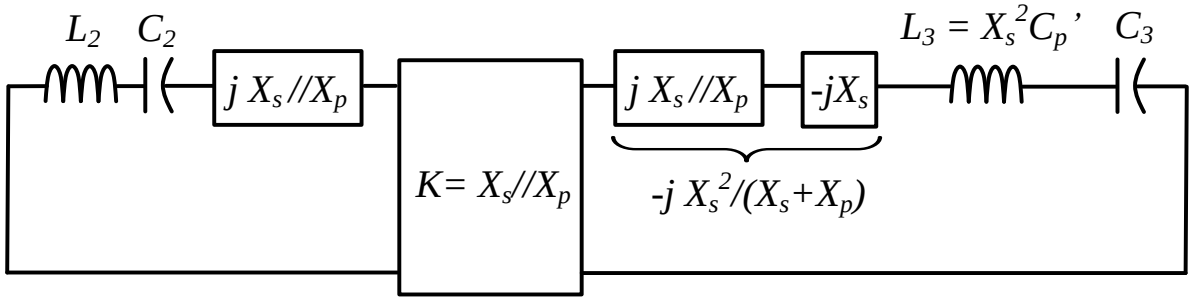

(c)

Figure 7.9: Transformation of the equivalent circuit in Fig. 7.7 to the conventional form of two series resonators coupled by an impedance inverter.

The coupling coefficient between the resonators k_{23} is:

$$k_{23} = \frac{K_{23}}{\sqrt{\alpha_2 \alpha_3}} \tag{7.19}$$

It is noted that (7.15), (7.17) (7.18), and (7.19), which are able to provide accurate calculations of k_{23}, are used in the synthesis described in Section 7.2.5.

The reactances X_s and X_p appearing in (7.15), (7.16), and (7.17) have a twofold effect. First, they detune the resonant frequencies of the resonators in Fig. 7.9(c). Because of their frequency dependence, they also modify the slope parameters of the resonators given by (7.18) and consequently the coupling coefficient k_{23}.

In order to understand which physical parameters control k_{23} and minimize of the number of parameters to be optimized, a closed-form formula for k_{23} is derived here by using (7.16) and assuming X_s and X_p to be frequency independent. Under those assumptions, the inductance and capacitance of the second resonator in Fig. 7.9(c) are:

$$L_3 = X_s^2 C_p' \ , \ C_3 = L_p' \big/ X_s^2 \tag{7.20}$$

The coupling coefficient k_{23} is derived as:

$$k_{23} = \frac{1}{2\pi f_o} \frac{X_p}{X_p + X_s} \frac{1}{\sqrt{L_2 C_p'}} \tag{7.21}$$

The reflected patch capacitance C_p' is a function of the turn ratio (n_1, n_2). X_s is the reflected probe reactance. Although these parameters can be used in changing k_{23}, to minimize the number of parameters in the optimization, we fix the value of the physical dimensions associated with

these parameters in the synthesis procedure. The primary control of k_{23} is from X_p, which corresponds to the physical dimension P_p.

The actual resonant frequency of resonator on the right hand side of the impedance inverter in Fig. 7.9(c) can be obtained by solving $X_3(\omega) = 0$. Within a small frequency detuning range, the frequency shift can be approximated by:

$$\Delta f_3 = \frac{1}{4\pi C_p'} \frac{1}{X_s + X_p} \tag{7.22}$$

As a result, the patch antenna size needs to be increased to compensate for the frequency upshift caused from the coupling between the middle cavity and patch antenna. The frequency detuning of the middle cavity resonator can be conveniently accounted for with the aid of the equivalent circuit in Fig. 7.6(a).

7.2.5 Filter/Antenna Design

Using the developed equivalent circuits and the guidelines described in the previous sections, a filter/antenna system that exhibits the same filtering functions of the reference filter is now designed.

As the first step, we design the patch antenna with Q_{rad} that matches $Q_{ext,2}$ of the reference filter. Because Q_{rad} varies relatively slowly with frequency, at this stage, the resonant frequency of the patch does not need to be exactly fixed and it suffices to use a frequency close to the desired center frequency of the filter/antenna system. The resonant frequency of the patch can always be adjusted during the design and little change in Q_{rad} is observed. Using Rogers RT/Duroid 5880, Q_{rad} = 17.2 is obtained with substrate thickness h_2 = 0.8 mm. The patch antenna is simulated using Ansoft High Frequency Structure Simulator (HFSS). Using the dimensions listed in Fig.

7.2, the patch is resonant at 9.97 GHz. Q_{rad} and Q_l are separately determined by simulating the patch with/without setting the dielectric and metallic losses to zero. The simulated patch antenna impedance is plotted and compared with the *RLC* model (Fig. 7.4) as shown in Fig. 7.10. Using the extracted *RLC* values, Q_{rad} and Q_l are calculated using equations (7.6) and (7.9) and are found as 17.3 and 585, respectively. The result of Q_l = 585 agrees well with calculations using (7.7)-(7.9).

In order to obtain the patch equivalent circuit element values reflected into the waveguide, the patch coupled to a waveguide using a coupling via is simulated as shown in Fig. 7.11(a). The patch appears as a shunt element in the waveguide, and its impedance is extracted as the impedance parameter Z_{12} after the waveguide ports are de-embedded to the reference plane *T*. The patch impedance as seen from the waveguide is plotted and compared with its equivalent *RLC* circuit. The waveguide characteristic impedance is chosen as Z_o = 1 Ω. Constant probe reactances X_2 and X_s evaluated at the patch resonant frequency are used in the *RLC* equivalents in Fig. 7.10 and Fig. 7.12, respectively. A frequency-dependent reactance X_s can be used that accounts for the difference between the reactances obtained using HFSS and the *RLC* model. The reactance X_s is extracted and plotted in Fig. 7.13. Plotted on the same figure, are the reactances X_p and $\omega L_2 - 1/\omega C_2$ for a middle cavity resonator having dimensions of L_{r2}' = 16.8 mm and P_p = 2.9 mm. Although X_s and X_p vary relatively slowly with frequency compared with $\omega L_2 - 1/\omega C_2$, their frequency dependence needs to be considered for more accurate k_{23} calculation by using (7.19). Using the equivalent circuit model in Fig. 7.6(a) and the aid of equation (7.19), the filter/antenna is designed to match the reference filter response. The impedance of the patch antenna obtained using HFSS (Fig. 7.12) is used in the circuit simulations as shown in Fig. 7.6(a). Only P_p was used to control k_{23}.

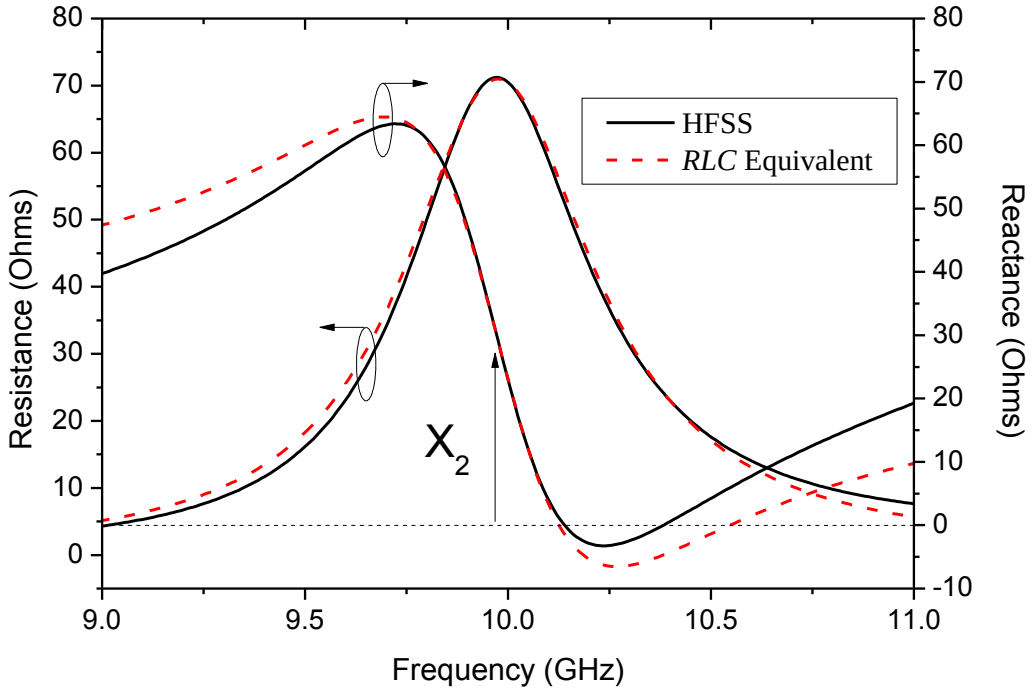

Figure 7.10: Simulated impedance of a probe-fed patch antenna and its equivalent *RLC* model (C_p = 1.882 pF, L_p = 0.135 nH, R_r = 147.1 Ω, R_l = 4961.7 Ω, n_2 = 0.695, X_2 = 29 Ω)

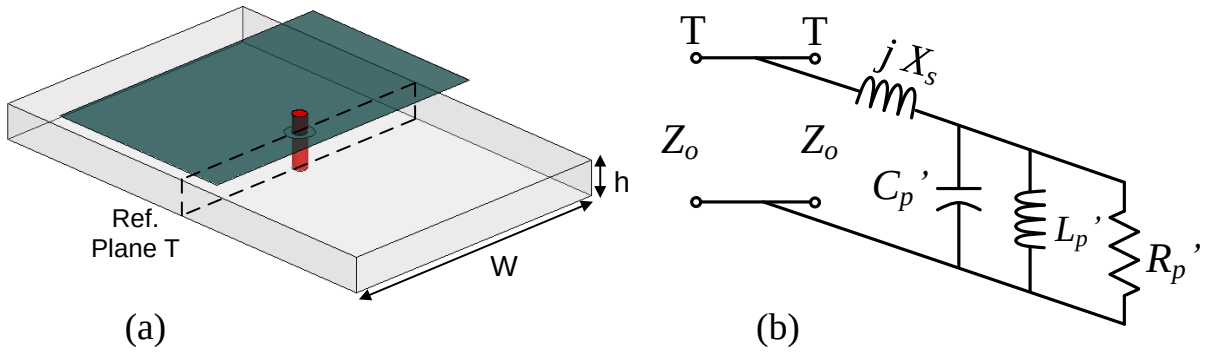

Figure 7.11: (a) Schematic of a patch antenna coupled to a waveguide through a coupling via and (b) its equivalent circuit.

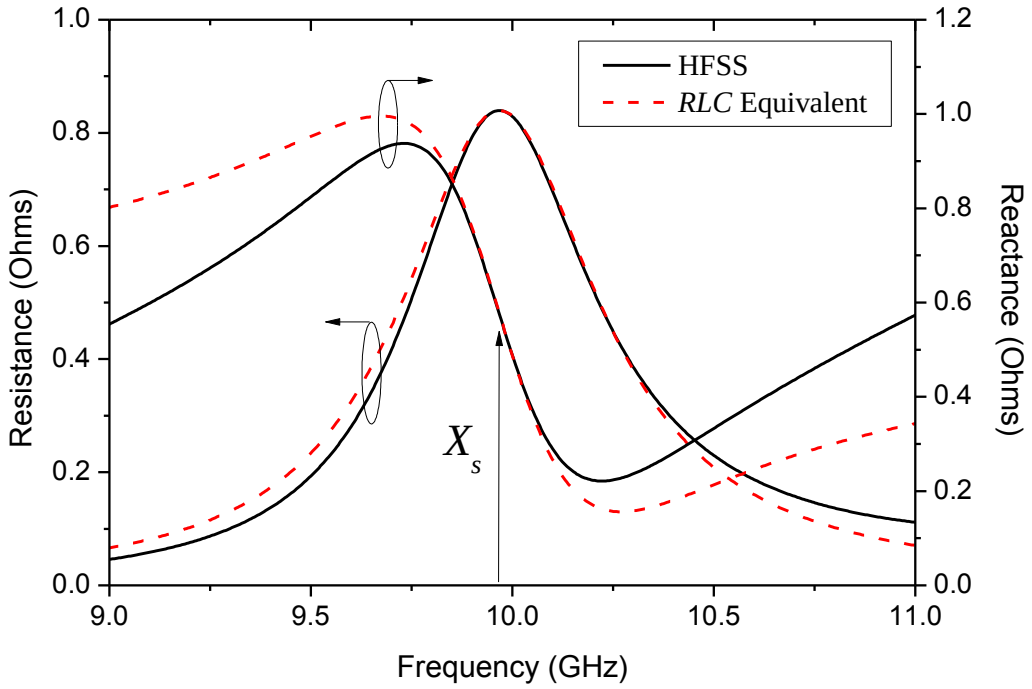

Figure 7.12: Simulated impedance of the patch antenna in Fig. 7.11(a) as seen from the waveguide and its equivalent *RLC* model (C_p' = 0.318 nF, L_p' = 0.802 pH, R_p' = 0.840 Ω, X_s = 0.576 Ω)

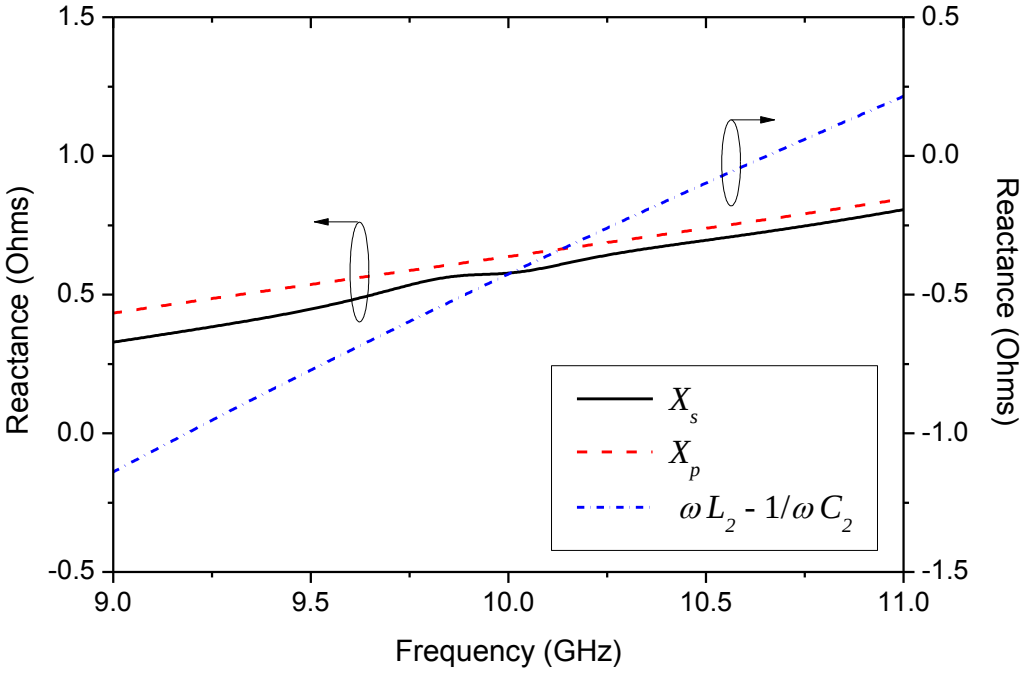

Figure 7.13: The reactances X_s and X_p compared with ($\omega L_2 - 1/\omega C_2$) showing a slower variation with frequency.

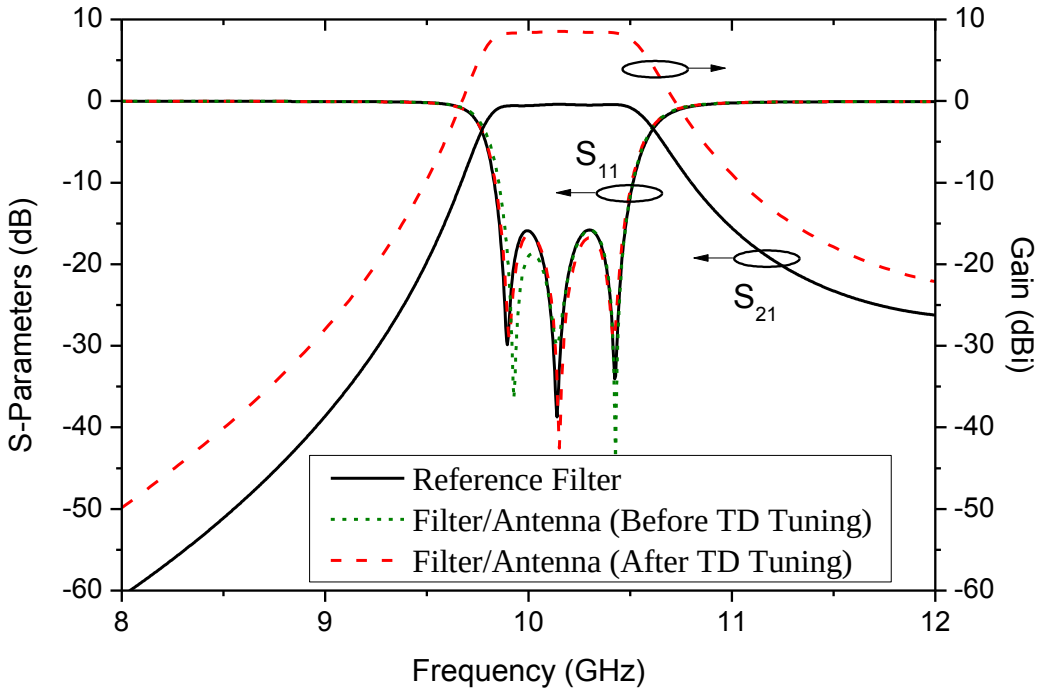

Figure 7.14: Simulated S_{11} and S_{21} of the reference filter compared to simulated S_{11} and gain of the filter/antenna shown in Fig. 7.1.

The dimensions and circuit parameters in the equivalent model are listed in Fig. 7.6. Based on the dimensions obtained using the circuit model, the filter/antenna is simulated using HFSS. In the simulations, the physical lengths of the resonators L_{r1} and L_{r2} are obtained from L_{r1}' and L_{r2}' by accounting for the negative transmission line lengths of the impedance inverters. The dimensions of the filter/antenna system obtained are the same as those listed in Fig. 7.2 except for P_p = 2.9 mm, and L_{r2} = 15.8 mm.

The reflection coefficient S_{11} of the filter/antenna is compared with the response of the reference filter in Fig. 7.14. Although the results are in close agreement, fine tuning is still necessary to complete the design. The discrepancy between the circuit model results and HFSS simulations is due to full-wave effects not captured by the circuit model. The model, however, provides an excellent starting point for further optimization.

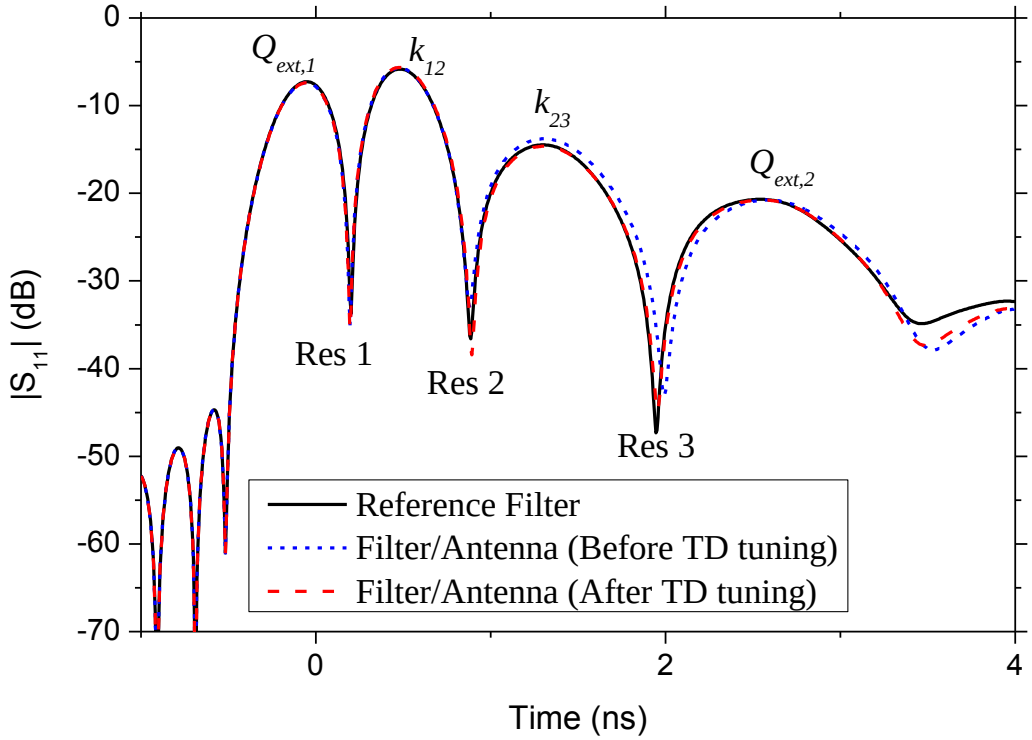

Figure 7.15: Time domain S_{11} responses of the reference filter and the filter/antenna shown in Fig. 7.1.

Since optimization using full-wave simulations is time consuming, time-domain filter tuning [27] is employed here. Using this time-domain technique, one is able to fine-tune the filter response with a few steps. Using a inverse Chirp-Z transform, the filter/antenna S_{11} response is plotted in time domain as shown in Fig. 7.15. It is observed that the responses from different sections of the filter/antenna are isolated in time. The peaks in the time-domain response correspond to the external coupling at the input port, the internal coupling between the two cavity resonators (k_{12}), the coupling between the middle cavity and the patch (k_{23}), and the external coupling of the patch to free space ($Q_{ext,2} = Q_{rad}$), respectively, from left to right. The dips correspond sequentially to the two cavity resonators and the patch antenna. The filter/antenna S_{11} time-domain response can be tuned to match that of the reference filter, the response of which is also plotted in Fig. 7.15. The comparatively higher level of the third peak indicates that the coupling coefficient k_{23} of the

filter/antenna is smaller than the desired coupling in the reference filter. P_p is increased from 2.9 mm to 3.1 mm, in order to correct the coupling level (L_{r2} is now 16 mm). The tuned S_{11} response of the filter/antenna system in time domain is illustrated in Fig. 7.15. After time-domain fine tuning, excellent agreement between the two cases is apparent. As a result, the frequency-domain responses of the two cases match closely as shown in Fig. 7.14.

The gain of the filter/antenna system at boresight shown in Fig. 7.14 follows the same roll-off of S_{21} of the reference filter. The filter/antenna system and the reference filter clearly exhibit the same filtering function.

7.2.6 Filter/Antenna Efficiency

In section 7.2.5, we have demonstrated that the patch antenna can be utilized as a resonator contributing to an additional pole in the filtering response while simultaneously acting as a radiating element. The combined dielectric and metal loss Q factor Q_l, and Q_{rad} of patch in the filter/antenna play the analogous roles of the unloaded Q factor Q_u and $Q_{ext,2}$, respectively in a conventional filter. Since the antenna in a filter/antenna system can generally have a Q_l that is very different from the unloaded Q factors Q_u of the other resonators in the structure, it is important to understand how the efficiency of the overall system is affected.

We now consider the scenario by which the last resonator of a filter structure with Q factors Q_u and $Q_{ext,2}$ is replaced by a resonator with Q factors Q_u' and $Q_{ext,2}$'.We require that the input reflection coefficient at the input port remain unchanged. This can be ensured if the same total energy dissipation conditions are maintained in both cases. More specifically, this happens when the *loaded* Q factors of the last resonators in the two cases are equal:

$$\frac{1}{Q_u}+\frac{1}{Q_{ext,2}}=\frac{1}{Q_u'}+\frac{1}{Q_{ext,2}'} \tag{7.23}$$

Under this condition the same average total energy is stored in the last resonator in the two cases. Since the power collected by the second port is inversely proportional to $Q_{ext,2}$ and S_{11} is identical in both cases, the efficiencies are related as:

$$\frac{\eta'}{\eta}=\frac{Q_{ext,2}}{Q_{ext,2}'}=1+\frac{Q_u'-Q_u}{Q_u'Q_u}Q_{ext,2} \tag{7.24}$$

where (7.23) has been used. For high unloaded Q factors, the difference of the efficiencies in dB is:

$$\Delta\eta=\eta'(dB)-\eta(dB)=4.343\frac{Q_u'-Q_u}{Q_u'Q_u}Q_{ext,2} \tag{7.25}$$

Since $Q_{ext,2} \sim$ 1/FBW, equation (7.25) shows that the effect of the change of Q_u on the system efficiency is smaller for larger fractional bandwidths.

For the integrated filter/antenna system designed, Q_u of the cavity resonators is found to be approximately 650. Q_l of the patch antenna was found as 585. Due to the proximity of two values, it was sufficient to match $Q_{ext,2}$ and Q_{rad}, although this is generally not the case. Using (7.23), $Q_{ext,2}$ or equivalently Q_{rad} is calculated as 17.3. Using (7.25), $\Delta\eta$ = -0.013 dB (0.997), which represents the decrease in efficiency caused by replacing a cavity resonator with a patch antenna, is negligibly small.

The overall efficiency of the integrated filter/antenna system is calculated using Gain/Directivity and found to be 91.8 %. The simulated directivity and gain using HFSS are found to be 8.91 and 8.54 dBi, respectively.

It is expedient to compare the performance of the integrated filter/antenna system with the more traditional way in which filters and antennas are cascaded in the system front end. If a high-Q filter that utilizes the same available materials used for the filter/antenna system is to be used, an antenna of 99.7% efficiency ($\Delta\eta$) which is impedance matched over a 8% fractional bandwidth will be needed to maintain the same overall efficiency (91.8%). The efficiency improvement earned by integrating the filter and antenna is evident. The efficiency of the standalone patch antenna can be calculated using:

$$\eta_A = \frac{1}{1 + Q_{rad} / Q_l} \tag{7.26}$$

which is 97%. Through filter/antenna integration, a 97% efficient antenna having a FBW~4% acts as a 99.7% efficient antenna with FBW~8%. In addition to the improved efficiency, and bandwidth, the integrated structure is very compact.

7.3 Fabrication and Measurement Results

A prototype filter/antenna is fabricated and measured to verify the synthesis procedure described in Section 7.2. Each layer of the entire system is individually fabricated using standard PCB fabrication processes. Then the coupling via is soldered into the patch antenna and middle cavity resonator. An SMA connector is soldered to the bottom resonator to form the feeding port. Finally, all three layers are bonded together using a solder paste inside a reflow oven. Photos of the fabricated filter/antenna are shown in Fig. 7.16.

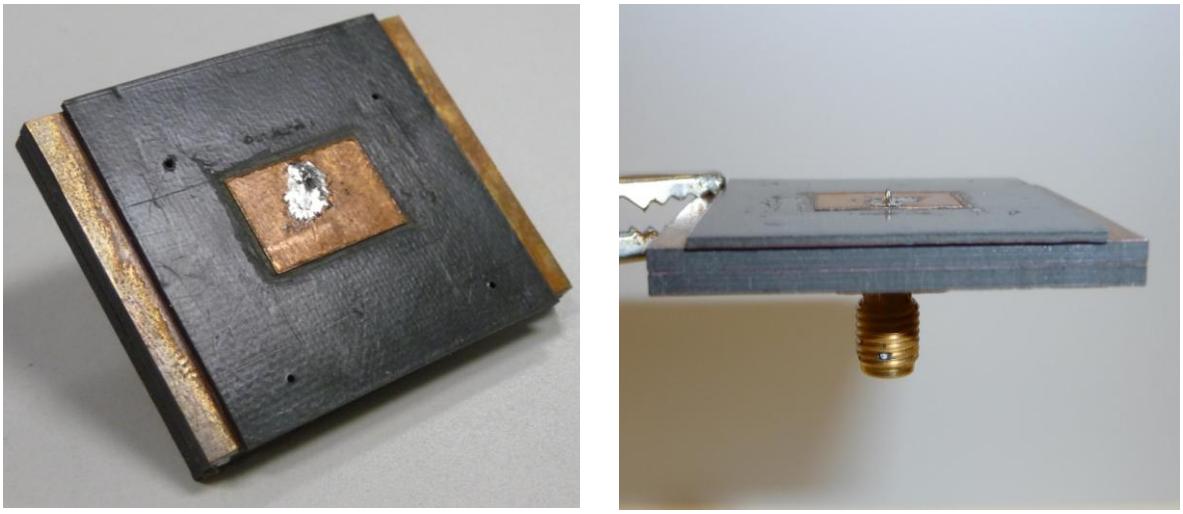

Figure 7.16: Photos of the fabricated filter/antenna system.

The measured filter/antenna S_{11} agrees very well with simulation results as shown in Fig. 7.17. The measured center frequency is 10.27 GHz, compared with 10.16 GHz in the simulation. This 1.1% frequency shift is due to the fabrication tolerances. Return losses higher than 12 dB are measured across the filter/antenna passband. It is clearly seen in Fig. 7.17 that three transmission poles have been achieved with two resonators and one patch antenna. To verify the filtering function of this integrated system, the gain of the filter/antenna system is measured in an anechoic chamber. The measured gain versus frequency is plotted against the simulation results as shown in Fig. 7.9. Both simulation and measurement results demonstrate the third-order filtering function across a wide frequency range. The measured filter/antenna bandwidth of 8.7% is slightly larger than the simulated 8.0%.

The radiation patterns of the filter/antenna are measured in both E- and H-planes. As shown in Fig. 7.18, the measured patterns match the simulation results at the center frequency. As expected, these radiation patterns are typical for patch antennas.

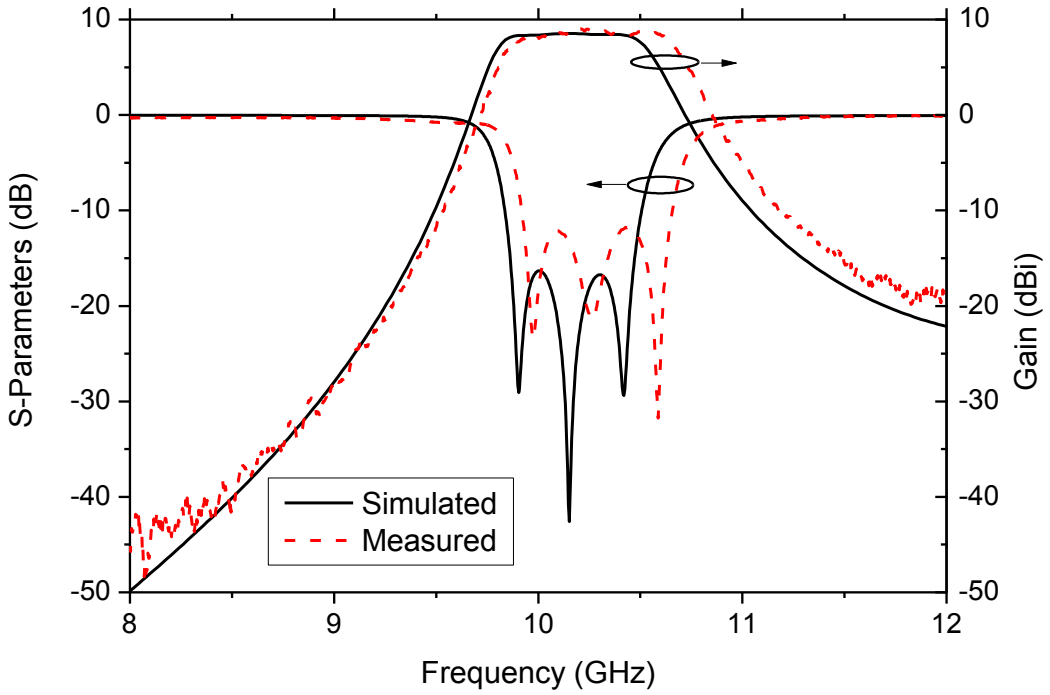

Figure 7.17: Simulated and measured responses of the three-pole vertically integrated filter with a patch antenna.

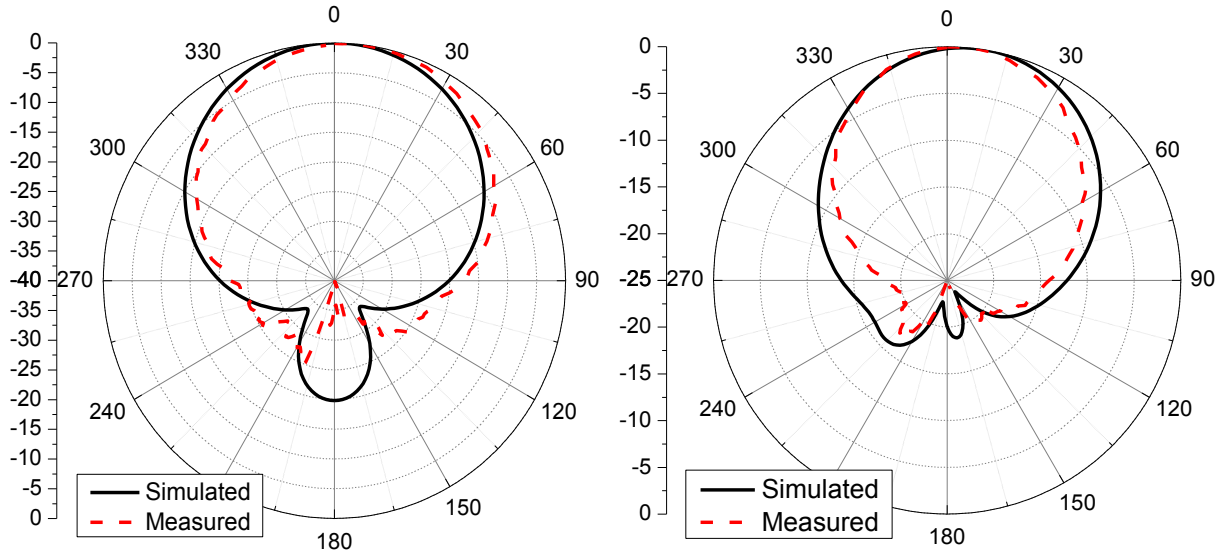

Figure 7.18: Simulated and measured radiation patterns in (a) H-plane and (b) E-plane at the center frequency.

It should be noted that the measured radiation patterns are slightly narrower than in simulation particularly in the E-plane, which corresponds to a higher directivity. Similar radiation patterns are observed across the entire passband. Therefore, the integrated patch antenna is able to function within an 8.7% fraction bandwidth, which is larger than the bandwidth (approximately 4%) of a probe-fed standalone patch antenna with the same dimensions.

The gain at the center frequency is measured to be 8.8 dBi, which is slightly higher than the simulated gain. This is attributed to the slightly larger directivity observed in measurements.

7.4 Filter/Antenna Array

The integrated filter/antenna systems exhibit small footprints that make them very suitable for array applications in which the separation between antenna elements is limited. It is desirable to study the mutual coupling effect on the impedance matching of the filter/antennas within an array. For this purpose, a 1 × 4 array arranged along the E-plane is simulated using HFSS. The spacing between the filter/antenna elements is 17.7 mm which corresponds to 0.6λ at the center frequency. The reflection coefficients of the filter/antenna elements in the array are compared with S_{11} of a standalone filter/antenna in Fig. 7.19. It is noticed that reflection coefficients are slightly raised from -16 to -14.5 dB primarily due to the mutual coupling effect on the resonant frequency of the patch.

The simulated radiation patterns in both E- and H-planes are plotted in Fig. 7.20. The simulated gain of the array at the center frequency is 13.9 dBi compared with the directivity of 14.36 dBi, implying an efficiency of 90% for the array.

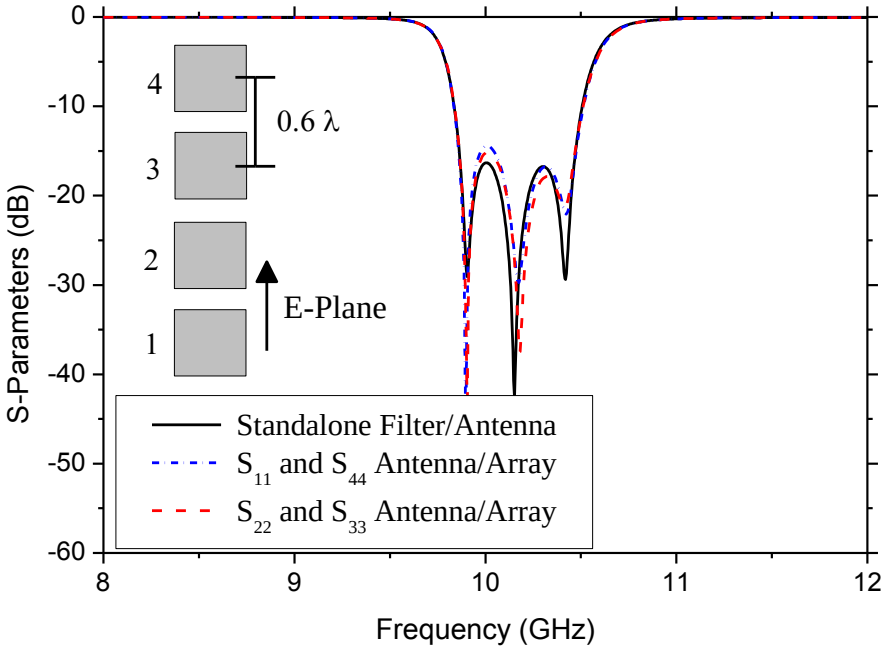

Figure 7.19: Simulated input reflection coefficients of individual filter/antenna elements in a 1 × 4 array.

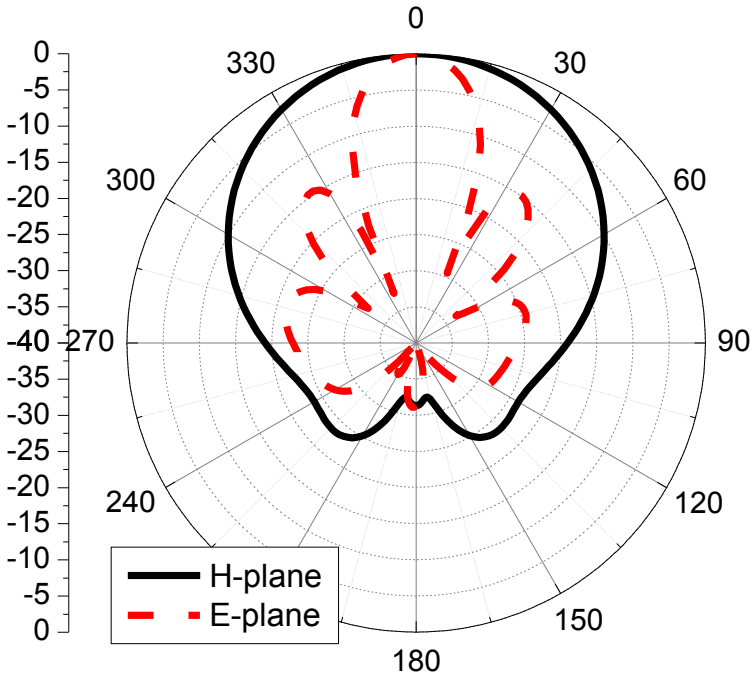

Figure 7.20: Simulated radiation patterns of the 1 × 4 filter/antenna array in both H- and E-planes at the center frequency.

7.5 Conclusion

A systematic synthesis approach to seamlessly integrate N high-Q resonators with a resonant patch antenna to realize $(N+1)^{th}$-order filtering was presented and verified through simulation, fabrication, and measurement. The integrated filter/antenna has small footprints, is highly efficient, and achieves enhanced bandwidth without compromising the high efficiency. This new filter/antenna architecture can enable compact and low-loss RF front ends and phased array systems.

8 CONCLUSION AND FUTURE WORK

8.1 Contributions

This dissertation focused on the seamless integration of high-Q filters with highly efficient antennas. The integrated filter/antenna systems are shown to exhibit small footprints and extremely high efficiencies. A number of contributions have been made in this work, which are summarized as follow:

- The analysis and synthesis of coupled-resonator microwave filters was formulated with the use of coupled-mode theory. This unconventional treatment stresses the underlying physical principles and provides a deeper understanding of phenomena involved in coupled resonator structures. Based on this approach, the insertion loss of filters was studied and accurate expression for filters up to fifth order were obtained.
- A systematic approach to integrate high-Q cavity filters with slot antennas was demonstrated. Within the integrated systems, the slot antenna was shown to effectively act as a 100% efficient radiator. In addition, the integrated filter/antenna systems exhibit small form factors. Further reduced form factors were achieved through vertically integrated structures.
- Wideband integrated filter/antenna systems were enabled by the use of a unique radiating structure, which consists of an open-ended aperture mounted on a ground plane. The enhanced bandwidth was made possible through the excitation and radiation of surface waves.
- Monopole antennas were systematically integrated with high-Q cavity filters to obtain integrated filter/antenna systems with omnidirectional radiation patterns.

- Integrated cavity filters with patch antennas were demonstrated, in which the patch antenna acted as an additional resonator in the filtering function, contributing to an additional pole.

8.2 Future Work

8.2.1 Integration of Antennas with other High-Q Filters.

In order to demonstrate integration of high-Q filters with antennas, cavity filters realized using SIW technology have been used in this dissertation. Integration of antennas with other high-Q filters such as dielectric resonator and evanescent-mode resonator filters has distinct advantages. Dielectric resonators are generally smaller in size compared with cavity filters and therefore present a means of further size reduction. In addition to being significantly smaller in size, the use of evanescent-mode resonators can help improve the out-of-band performance of the integrated systems by increasing the separation between the desired passband and the spurious response.

8.2.2 Implementation of Vertically Integrated Filter/antennas in Antenna Arrays

Due to their extremely small footprints, vertically integrated filter/antennas form a very suitable choice for the implementation of antenna arrays, in which the separation between the antenna elements is limited. The use of vertically integrated cavity filters with slot antennas in antenna arrays was recently demonstrated [31]. Arrays of vertical filters integrated with patch antennas are currently being fabricated.

8.2.3 Integrated Filter/antenna Systems with General Filtering Functions

The integrated filter/antennas presented were implemented by coupling the constituent resonators in a cascade configuration, from which all-pole filtering characteristics were obtained. More

general filtering functions, exhibiting transmission zeros near passband edges, can be realized provided couplings between non-adjacent resonators are used.

8.2.4 Tunable Integrated Filter/Antenna Systems

There has been an increased interest in frequency-tunable systems over the last ten years. By using suitable tuning elements such as a semiconductor or Barium Strontium Titanate (BST) varactors, the response of a filter/antenna system can be frequency-tuned. The equivalent circuit models of the different filter/antennas developed in this dissertation can be used to model the tunable structures facilitating their design.

9 REFERENCES

[1] Jong-Hoon Lee, S. Pinel, J. Laskar and M. M. Tentzeris, "Design and Development of Advanced Cavity-Based Dual-Mode Filters Using Low-Temperature Co-Fired Ceramic Technology for V-Band Gigabit Wireless Systems," *IEEE Trans. Microw. Theory Tech.,* vol. 55, pp. 1869-1879, 2007.

[2] Kiburm Ahn and Inbok Yom, "A ka-band multilayer LTCC 4-pole bandpass filter using dual-mode cavity resonators," in *IEEE MTT-S Int. Microw. Symp. Dig.* 2008, pp. 1235-1238.

[3] Bosui Liu, Xun Gong and W. J. Chappell, "Applications of layer-by-layer polymer stereolithography for three-dimensional high-frequency components," *IEEE Trans. Microw. Theory Tech.,* vol. 52, pp. 2567-2575, 2004.

[4] Xun Gong, Bosui Liu, L. P. B. Katehi and W. J. Chappell, "Laser-based polymer stereolithography of vertically integrated narrow bandpass filters operating in K band," in *IEEE MTT-S Int. Microw. Symp. Dig.* 2004, pp. 425-428 vol.2.

[5] L. Harle and L. P. B. Katehi, "A vertically integrated micromachined filter," *IEEE Trans. Microw. Theory Tech.,* vol. 50, pp. 2063-2068, 2002.

[6] D. Deslandes and Ke Wu, "Single-substrate integration technique of planar circuits and waveguide filters," *IEEE Trans. Microw. Theory Tech.,* vol. 51, pp. 593-596, 2003.

[7] Xiao-Ping Chen and Ke Wu, "Substrate Integrated Waveguide Cross-Coupled Filter With Negative Coupling Structure," *IEEE Trans. Microw. Theory Tech.,* vol. 56, pp. 142-149, 2008.

[8] Jong-Hoon Lee, N. Kidera, G. DeJean, S. Pinel, J. Laskar and M. M. Tentzeris, "A V-band front-end with 3-D integrated cavity filters/duplexers and antenna in LTCC technologies," *IEEE Trans. Microw. Theory Tech.,* vol. 54, pp. 2925-2936, 2006.

[9] G. Q. Luo, W. Hong, H. J. Tang, J. X. Chen, X. X. Yin, Z. Q. Kuai and K. Wu, "Filtenna Consisting of Horn Antenna and Substrate Integrated Waveguide Cavity FSS," *Antennas and Propagation, IEEE Transactions on,* vol. 55, pp. 92-98, 2007.

[10] B. Froppier, Y. Mahe, E. M. Cruz and S. Toutain, "Integration of a filtering function in an electromagnetic horn," in *Microwave Conference, 2003. 33rd European,* 2003, pp. 939-942.

[11] T. Le Nadan, J. P. Coupez and C. Person, "Optimization and miniaturization of a filter/antenna multi-function module using a composite ceramic-foam substrate," in *Microwave Symposium Digest, 1999 IEEE MTT-S International,* 1999, pp. 219-222 vol.1.

[12] A. Abbaspour-Tamijani, J. Rizk and G. Rebeiz, "Integration of filters and microstrip antennas," in *Antennas and Propagation Society International Symposium, 2002. IEEE,* 2002, pp. 874-877 vol.2.

[13] Chin-Kai Lin and Shyh-Jong Chung, "A compact edge-fed filtering microstrip antenna with 0.2 dB equal-ripple response," in *Microwave Conference, 2009. EuMC 2009. European,* 2009, pp. 378-380.

[14] Chao-Tang Chuang and Shyh-Jong Chung, "Synthesis and Design of a New Printed Filtering Antenna," *Antennas and Propagation, IEEE Transactions on,* vol. 59, pp. 1036-1042, 2011.

[15] Xun Gong, W. J. Chappell and L. P. B. Katehi, "Embedded radiating filters in metamaterial substrates," in *IEEE Int. Antennas Propag. Symp. Digest,* 2003, pp. 351-354 vol.3.

[16] G. L. Matthaei, L. Young and E. M. T. Jones, *Microwave Filters, Impedance-Matching Networks, and Coupling Structures.* Dedham, MA: Artech House Books, 1980.

[17] R. J. Cameron, C. M. Kudsia and R. R. Mansour, *Microwave Filters for Communication Systems: Fundamentals, Design, and Applications.* Wiley, 2007.

[18] J. -. Hong and M. J. Lancaster, *Microstrip Filters for RF/Microwave Applications.* Wiley, 2001.

[19] A. E. Atia and A. E. Williams, "Narrow-Bandpass Waveguide Filters," *IEEE Trans. Microw. Theory Tech.,* vol. 20, pp. 258-265, 1972.

[20] Chi Wang and K. A. Zaki, "Dielectric resonators and filters," *IEEE Microw. Mag.,* vol. 8, pp. 115-127, 2007.

[21] A. Atia, A. Williams and R. Newcomb, "Narrow-band multiple-coupled cavity synthesis," *Circuits and Systems, IEEE Transactions on,* vol. 21, pp. 649-655, 1974.

[22] R. J. Cameron, "General coupling matrix synthesis methods for Chebyshev filtering functions," *Microwave Theory and Techniques, IEEE Transactions on,* vol. 47, pp. 433-442, 1999.

[23] H. A. Haus, *Waves and Fields in Optoelectronics.* Englewood Cliffs, NJ: Prentice-Hall, 1984.

[24] A. F. Stevenson, "Theory of Slots in Rectangular Wave-Guides," *Journal of Applied Physics,* vol. 19, pp. 24-38, 1948.

[25] L. Josefsson, "A waveguide transverse slot for array applications," *IEEE Trans. Antennas Propag.,* vol. 41, pp. 845-850, 1993.

[26] R. E. Collin, *Foundations for Microwave Engineering.* New York: McGraw-Hill, 1992.

[27] "Application note 1287-8: Simplified filter tuning using time domain," Agilent Technologies Corp., Palo Alto, CA., 2001.

[28] C. A. Balanis, *Antenna Theory: Analysis and Design.* Hoboken, N.J.: Wiley-Interscience, 2005.

[29] Tze-Min Shen, Chi-Feng Chen, Ting-Yi Huang and Ruey-Beei Wu, "Design of Vertically Stacked Waveguide Filters in LTCC," *IEEE Trans. Microw. Theory Tech.,* vol. 55, pp. 1771-1779, 2007.

[30] Jong-Hoon Lee, S. Pinel, J. Papapolymerou, J. Laskar and M. M. Tentzeris, "Low-loss LTCC cavity filters using system-on-package technology at 60 GHz," *IEEE Trans. Microw. Theory Tech.,* vol. 53, pp. 3817-3824, 2005.

[31] Haitao Cheng, Y. Yusuf and Xun Gong, "Vertically Integrated Three-Pole Filter/Antennas for Array Applications," *IEEE Antennas Wireless Propag. Letters,* vol. 10, pp. 278-281, 2011.

[32] D. M. Pozar, "Rigorous closed-form expressions for the surface wave loss of printed antennas," *Electronics Letters,* vol. 26, pp. 954-956, 1990.

[33] F. J. Zucker, "Surface-wave antennas," in *Antenna Engineering Handbook*, R. C. Johnson, Ed. McGraw-Hill, 1992, .

[34] G. Markov, "Antennas," 1965.

[35] F. Mira, J. Mateu, S. Cogollos and V. E. Boria, "Design of Ultra-Wideband Substrate Integrated Waveguide (SIW) Filters in Zigzag Topology," *Microwave and Wireless Components Letters, IEEE,* vol. 19, pp. 281-283, 2009.

[36] Xun Gong, A. Margomenos, Bosui Liu, S. Hajela, L. P. B. Katehi and W. J. Chappell, "Precision fabrication techniques and analysis on high-Q evanescent-mode resonators and filters of different geometries," *IEEE Trans. Microw. Theory Tech.,* vol. 52, pp. 2557-2566, 2004.

[37] R. F. Harrington, *Time-Harmonic Electromagnetic Fields.* New York: McGraw-Hill, 1961.

[38] S. Egashira and E. Nishiyama, "Stacked microstrip antenna with wide bandwidth and high gain," *Antennas and Propagation, IEEE Transactions on,* vol. 44, pp. 1533-1534, 1996.

[39] Kin-Fai Tong, Kwai-Man Luk, Kai-Fong Lee and R. Q. Lee, "A broad-band U-slot rectangular patch antenna on a microwave substrate," *Antennas and Propagation, IEEE Transactions on,* vol. 48, pp. 954-960, 2000.

[40] Yu Lin Zhang, Wei Hong, Ke Wu, Ji Xin Chen and Hong Jun Tang, "Novel substrate integrated waveguide cavity filter with defected ground structure," *IEEE Trans. Microw. Theory Tech.,* vol. 53, pp. 1280-1287, 2005.